Studies on Structures and Electronic Properties of Organic Thin Film Transistors(Dissertation_全文)

AUTHOR(S):

Natsume, Yutaka

Studies on Structures and Electronic Properties of Organic Thin Film Transistors

Yutaka Natsume

2009

Preface

Since the first report on organic semiconductors in the late 1940s, a large number of experimental and theoretical investigations have been made. In contrast to the fruitful prosperity of inorganic semiconductors in electronic devices, initial application of organic semiconductors to transistors was only reported in the 1980s. Over the past decade, however, organic thin film transistors (OTFTs) have been expected to be applied to large-area flexible devices such as active matrix of liquid crystal displays, electronic papers, light-emitting diodes, photovoltaic cells, low-end smart cards, radio-frequency ID tags, and so on. The principal advantages of using organic semiconductors are low cost and high processibility.

One of the most promising candidates for organic semiconductors, pentacene, has been widely used as an active layer of OTFTs. Although the OTFTs using pentacene exhibit relatively high carrier mobility of 0.1 to 1 cm^2/Vs, which is comparable to amorphous silicon, the pentacene thin films and single crystals have been prepared hitherto mostly by vacuum evaporation process because of its low solubility. Printing technologies will be feasible for the cost-effective fabrication of the large-area electronic devices, thereby establishing the position of OTFTs in the market near future. Solution-processed OTFTs ever reported have been prepared mainly from polymer organic semiconductors, which exhibit lower carrier mobilities than pentacene in general.

This thesis proposes a novel solution process, making use of pentacene, that provides the large-area OTFT arrays with high carrier mobility. The studies also clarify the electronic structures of several conjugated molecules based on the density functional calculations, the crystalline structures and crystal growth mechanism of the solution-processed thin films, and the characteristics of the solution-processed OTFTs in comparison with the vacuum-deposited ones. The author hopes that this study would be helpful to the future development in the plastic electronics.

Contents

Chapter 1

General introduction

1.1 Organic semiconductors

Organic semiconductors have been studied since the late 1940s [1]. However, until recently they had not been applied to electronic devices successfully, in spite of a large number of experimental and theoretical efforts. Organic semiconductors can be classified into two groups, polymers and small molecules. In the late 1970s, Shirakawa, MacDiarmid, and Heeger found that doped polyacetylene (cf. Figure 1.1(a)) has a high conductivity comparable to copper [2], and this discovery had opened the way to practical applications in the organic electronics. The applications of these conjugated polymers to the electronic devices as semiconductive materials have been reported since the 1980s [3]. These polymers generally show semiconductive characteristics without chemical doping. On the other hand, the conductivity of the small molecular semiconductors, e.g. anthracene and perylene, has been already studied since the 1950s [4], followed by the discovery of the metallic conductivity and superconductivity of TTF–TCNQ (see Figures 1.1(b) and (c)) charge-transfer salt in the 1970s and 1980s [5,6]. In the 1980s, the small molecular semiconductors have also been applied to electroluminescent diodes [7] and field-effect transistors (FETs) [8]; however, the electronic performances for the organic devices, such as luminescence efficiency and carrier mobility, were too low to be utilized for practical applications.

The charge carrier mobility of organic semiconductors has been mainly measured by time-of-flight (TOF) method, which was first applied to organic single crystals in 1960 [9,10], and other methodologies have also been carried out, for example, space-charge-limited current [11], Hall effect [12,13], and so on. The upper limit of carrier mobility in the organic molecular crystals may be placed between 1 to 10 cm^2/Vs at room temperature on the basis of TOF measurement. Organic FETs have attracted

much attention since the 1990s, because the both thin-film and single-crystal FETs have been reported to show high carrier mobility more than 1–10 cm^2/Vs [14–16]. On the whole, the small molecular semiconductors tend to exhibit higher carrier mobility than the polymers, as is attributed to highly ordered solid-state structure of the small molecules. One of the polycyclic aromatic hydrocarbons (PAHs), pentacene (Figure 1.1(d)), has been most widely used in organic thin-film transistors (OTFTs) among a variety of organic semiconductors so far. In this thesis, the author focuses mainly on pentacene, including other PAHs, and the crystalline structures and electronic properties of thin films are studied.

1.2 Single-crystal and thin-film structures of organic semiconductors

Depending on a given process condition and environment, molecules show various modes of packing that result in an ordered structure over the substrate. Since the intermolecular interactions are crucial for the exhibited semiconductor properties, such crystalline form of the structures should be well characterized. Gavezzotti and Desiraju have classified the crystal structures of PAHs into four basic structural types. Their study was based on surveying molecular systems in the crystal structure database and inducing principles of energetic and geometrical criteria [17,18]. The four different crystal structures of PAHs are shown in Figure 1.2, which shows anthracene, pyrene, coronene, and violanthrene as examples of the herringbone, sandwich, γ and β structures, respectively [19–22]. The basis of this structural diversity is that all polymorphs are layered structures, and differences arise from intra-layer interactions. The latter consists of intermolecular interactions of the type C–H, between a carbon of the aromatic ring of one molecule and a hydrogen at a ring edge of adjacent molecules, and type C–C, between the aromatic rings of neighboring molecules. The β- and γ-type structures have a tendency to form one-dimensional stacking of molecules, whereas the herringbone and sandwich-type structures form two-dimensional networks

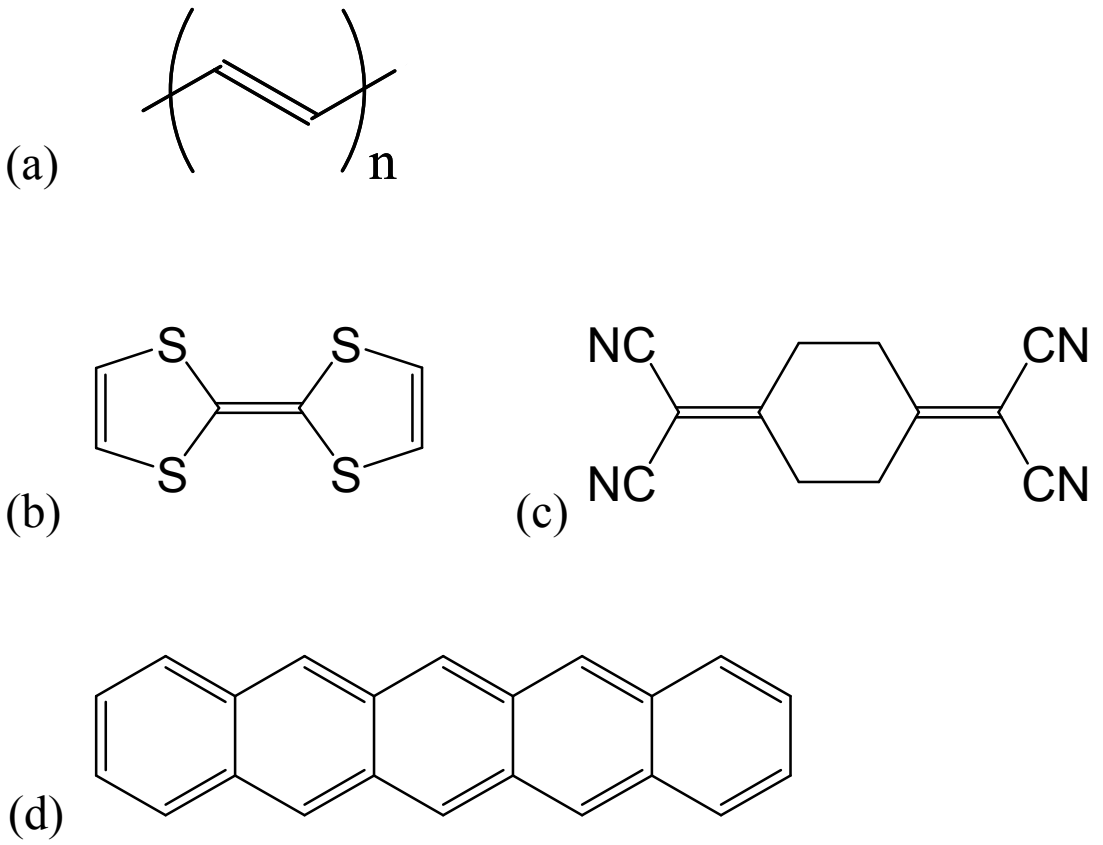

Figure 1.1: Chemical structures of organic semiconductors (a) polyacetylene, (b) TTF, (c) TCNQ, and (d) pentacene.

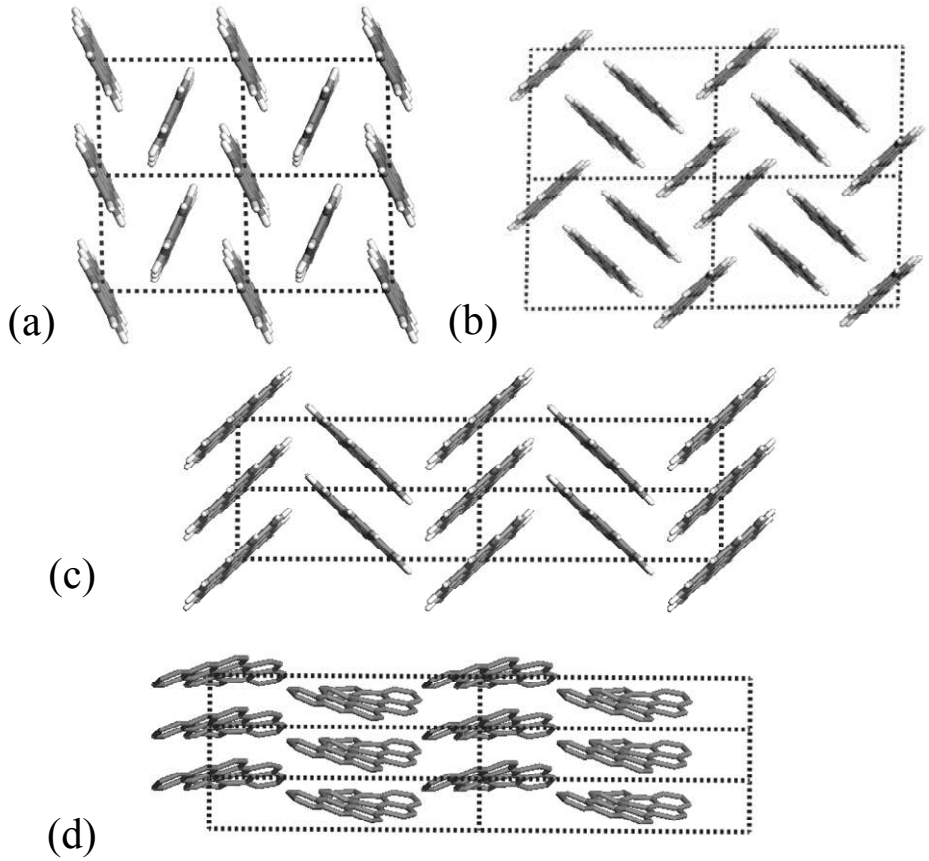

Figure 1.2: Four basic crystal packings of PAHs (a) anthracene (herringbone), (b) pyrene (sandwich), (c) coronene (gamma), and (d) violanthrene (betha).

in the *a*-*b* plane. The tendency to result in the respective crystal structures depends on the relative abundance of the C–H and C–C interactions in the layer, that is, the C–C interactions promote one-dimensional stacking such as the β and γ-type, while the C–H interactions promote two-dimensional stacking such as the herringbone stacking.

Crystal structure of pentacene, which can be classified into herringbone-type structure within the criteria mentioned above, was first reported by Campbell *et al*. in the early 1960s [23,24]. Campbell's single crystal was grown from solution, and yielded an interlayer spacing of $d(0\ 0\ 1)$ = 14.5 Å. Since the 1990s, pentacene has been frequently used as a source of vacuum-evaporation process for organic thin film transistors (OTFTs), and its vacuum-deposited thin films have been reported to show two interlayer values of $d(0\ 0\ 1)$ = 14.4 and 15.4 Å, which were termed *bulk phase* and *thin-film phase*, respectively [25]. Holmes and Mattheus independently reported another crystal structure with $d(0\ 0\ 1)$ = 14.1 Å [26,27], and moreover several polymorphs of pentacene crystalline structures for single crystal and thin film were presented by Mattheus [28]. In this thesis, the author fabricates solution-processed pentacene thin films and determines the crystal structure of the film.

1.3 Organic thin-film transistors

Since the invention of transistor by Bardeen, Shockley, and Brattain in 1947 [29,30], the FETs based on single-crystal inorganic semiconductors such as Si, Ge, and GaAs are omnipresent in our life today. Kahng and Atalla first reported the fabrication of silicon-based metal-oxide-semiconductor FETs (MOSFETs) in 1960 [31]. Nowadays, the Si-based MOSFETs have made the most prolific advances in microelectronics, such as discrete devices and integrated circuits. In contrast, the first demonstration of field effect in the organic semiconductors was reported in the 1960s [32]. Since the first application of the organic semiconductors to FETs in the 1980s [3,8], the impressive improvements in the performance have been attained especially during the last decade. However, OTFTs cannot rival the performance of FETs based

on the inorganic semiconductors, because of several orders of magnitudes lower carrier mobility. In order to put OTFTs to practical use, it will be necessary to find another unique applications that take advantage of the organic semiconductors, such as large-area coverage, flexibility, and low-temperature processing at low cost. Such preferable applications are thought to be switching devices for active matrix of liquid crystal, electronic paper, and organic electroluminescence displays. The printing technologies will be desirable for the purpose of making the large-area plastic electronics marketable. To this end, novel soluble materials have been studied vigorously by several groups [33–37]. Nevertheless the most promising candidate is still pentacene, since it shows high carrier mobility comparable to amorphous silicon. The hydrogenated amorphous silicon (a-Si:H) is widely used in liquid crystal display at present; however it is impossible to fabricate the active layer of a-Si:H on the plastic substrate, because of high temperature in the deposition process (ca. 360 °C). In this thesis, the author proposes a novel solution process using pentacene, and evaluates the electronic properties of the solution-processed pentacene TFTs in comparison with the conventional vacuum-deposited ones.

1.4 Outline of this thesis

In this chapter, the history of developments in organic electronics has been introduced, and focus was made on the application of electronic properties and the crystal structures. In this thesis, the author focuses on pentacene including other PAHs as organic semiconductors, and a novel solution processing of organic thin films is presented. The purpose of this thesis is to provide the large-area electronic devices based on OTFTs using a simple solution processing, and to reveal the crystalline structures and the electronic properties of the solution-processed thin films. The outline of this thesis is described as follows.

In Chapter 2, the fabrication and characterization of OTFTs using several PAHs, pentacene, ovalene, dibenzocoronene and hexabenzocoronene, are reported. These

organic semiconductors are deposited on silicon wafers in a vacuum. The pentacene TFT shows the highest field-effect mobility among these PAHs. The film structures are analyzed by using atomic force microscopy and X-ray diffraction. First-principles calculations of a molecular layer extracted from the bulk structures are performed to investigate the electronic interactions between the neighboring molecules. The results reveal that the high field-effect mobility of the pentacene thin film is due to large grain size and intrinsic electronic properties.

In Chapter 3, pentacene-based direct solution processing of organic thin films is presented. Two types of surface structure are observed: flat and rough domains. The TFT characteristics of both domains are evaluated. In-plane structures of solution-processed thin films are analyzed by using grazing-incidence X-ray diffraction (GIXD). The crystal structure is proposed on the basis of two dimensional mapping of the GIXD patterns.

In Chapter 4, the electrical and chemical stabilities of solution-processed pentacene TFTs are investigated. Using an analytical model for transfer characteristics, the trap state of the solution-processed pentacene TFT are estimated in comparison with vacuum-deposited one. The shifts in the electrical properties of OTFTs are pursued during long-term storage in air and under dark conditions. Surface mass spectroscopy is used to investigate the origin of the shift in the TFT performances.

In Chapter 5, large-area TFT arrays are fabricated by means of the solution processing. The directionality in the crystal growth of pentacene is investigated, and GIXD and electron diffraction analyses reveal the crystal-growth azimuth of the solution-processed pentacene films. The high performances in TFT arrays are achieved by controlling the growth direction of the pentacene films from solution, and by optimizing conditions for drop casting.

In Chapter 6, single and multi-domain thin films of pentacene are fabricated by coating flake crystals dispersed in a liquid media. The films are structured with oriented crystals and have a well-defined grain structure obtained from the source crystals. Single and multi-domain films assembled with large or sub-micron crystals

show carrier mobility of 1 cm^2/Vs and above 0.01 cm^2/Vs, respectively. Small electrode contact resistance of the films and transport barrier heights below 56 meV for multi-domain films were confirmed from the transmission line model patterns and the temperature dependence of the mobility.

References

1) D. D. Eley, *Nature* **162**, 819 (1948).

2) H. Shirakawa, E. J. Louis, A. G. MacDiarmid, C. K. Chiang, A. J. Heeger, *J. Chem. Soc. Chem. Commun.* 578, (1977).

3) F. Ebisawa, T. Kurokawa, S. Nara, *J. Appl. Phys.* **54**, 3255 (1983).

4) H. Akamatsu, H. Inokuchi, Y. Matsunaga, *Nature* **173**, 168 (1954).

5) J. P. Ferraris, D. O. Cowan, V. Walatka, Jr. and J. H. Perlstein, *J. Am. Chem. Soc.* **95**, 948 (1973).

6) D. Jerome, A. Mazaud, M. Ribault, K. Bechgaard, *J. Phys. Lett.* **41**, L95 (1980).

7) C. W. Tang, S. A. Van Slyke, *Appl. Phys. Lett.* **51**, 913 (1987).

8) K. Kudo, M. Yamashita, T. Moriizumu, *Jpn. J. Appl. Phys.* **23**, 130 (1984).

9) O. H. LeBlanc Jr., *J. Chem. Phys.* **33**, 636 (1960).

10) R. G. Kepler, *Phys. Rev.* **119**, 1226 (1960).

11) Y. Shen, A. R. Hosseini, M. H. Wong, G. G. Malliaras, *Chem. Phys. Chem.* **5**, 16 (2004).

12) V. Podzorov, E. Menard, J. A. Rogers, M. E. Gershenson, *Phys. Rev. Lett.* **95**, 226601 (2005).

13) J. Takeya, K. Tsukagoshi, Y. Aoyagi, T. Takenobu, Y. Iwasa, *Jpn. J. Appl. Phys. Part 2* **44**, L1393 (2005).

14) S. F. Nelson, Y.-Y. Lin, D. J. Gundlach, T. N. Jackson, *Appl. Phys. Lett.* **72**, 1854 (1998).

15) R. W. I. de Boer, M. E. Gershenson, A. F. Morpurgo, V. Podzorov, *Phys. Stat. Sol.* **201**, 1302 (2004).

16) J. Y. Lee, S. Roth, Y. W. Park, *Appl. Phys. Lett.* **88**, 252106 (2006).

17) G. R. Desiraju, A. Gavezzotti, *Acta Cryst. B* **45**, 473 (1989).

18) C. C. Mattheus, G. A. de Wijs, R. A. de Groot, T. T. M. Palstra, *J. Am. Chem. Soc.*

125, 6323 (2003).

19) R. Mason, *Acta Crystallogr.* **17**, 547 (1964).

20) A. Camerman, J. Trotter, *Acta Crystallogr.* **18**, 636 (1965).

21) J. K. Fawcett, J. Trotter, *Proc. R. Soc. London, Ser. A* **289**, 366 (1965).

22) I. Oonishi, S. Fujisawa, J. Aoki, Y. Sasada, *Bull. Chem. Soc. Jpn.* **59**, 2233 (1986).

23) R. B. Campbell, J. M. Robertson, J. Trotter, *Acta Crystallogr.* **14**, 705 (1961).

24) R. B. Campbell, J. M. Robertson, J. Torotter, *Acta Crystallogr.* **15**, 289 (1962).

25) C. D. Dimitrakopoulos, A. R. Brown, A. Pomp, *J. Apll. Phys.* **80**, 2501 (1996).

26) D. Holmes, S. Kumaraswamy, A. J. Matzger, K. P. C. Vollhardt, *Chem.-Eur. J.* **5**, 3399 (1999).

27) C. C. Mattheus, A. B. Dros, J. Baas, A. Meetsma, J. L. de Boer, T. T. M. Palstra, *Acta Crystallogr. C* **57**, 939 (2001).

28) C. C. Mattheus, A. B. Dros, J. Baas, G. T. Oostergentel, A. Meetsma, J. L. de Boer, T. T. M. Palstra, *Synth. Met.* **138**, 475 (2003).

29) J. Bardeen, W. K. Brattain, *Phys. Rev.* **71**, 717 (1947).

30) W. Shockley, *Bell Syst. Tech. J.* **28**, 435 (1949).

31) D. Kahng, M. M. Atalla, *IRE Solid-State Devices Reserch Conference, Carnegie Institute of Technology*, Pittsburgh, PA (1960).

32) G. H. Heilmeier, L. A. Zanoni, *J. Phys. Chem. Solids* **25**, 603 (1964).

33) M. M. Payne, S. A. Odom, S. R. Parkin, J. E. Anthony, *Org. Lett.* **6**, 3325 (2004).

34) H. Meng, J. Zheng, A. J. Lovinger, B.-C. Wang, P. Gregory, V. Patten, Z. Bao, *Chem. Mater.* **5**, 1778 (2003).

35) M. Mas-Torrent, P. Hadley, S. Bromley, X. Ribas, J. Tarres, M. Mas, E. Molins, J. Veciana, C. Rovira, *J. Am. Chem. Soc.* **126**, 8546 (2004).

36) K. Takimiya, H. Ebata, K. Sakamoto, T. Izawa, T. Otsubo, Y. Kunugi, *J. Am. Chem. Soc.* **128**, 12604 (2006).

37) F. Valiyev, W.-S. Hu, H.-Y. Chen, M.-Y. Kuo, I. Chao, Y.-T. Tao, *Chem. Mater.* **19**, 3018 (2007).

Chapter 2

Structures and electronic properties of thin films of polycyclic aromatic hydrocarbons

2.1 Introduction

Organic thin film transistors (OTFTs) have the potential for and are expected to be used in various applications in the near future, such as flexible displays, smart cards, radio frequency tags, and sensor arrays [1–4]. For such applications, pentacene is one of the most promising candidates as an active *p*-type semiconductive material in terms of the high field-effect mobility and on-to-off current ratio. Although various attempts have been made at using different organic semiconductors, such as thiophene oligomers, rubrene, phthalocyanine, and several π-conjugated polymers, only a few of these studies have focused on the diversity of the molecular structure and its relationship to the semiconductor performance [5,6], especially in the case wherein the molecules consist of only hydrocarbons, i.e. polycyclic aromatic hydrocarbons (PAHs). Since the selection of the starting PAH molecule is critical in the process of enhancing the performance and durability of the material, it is of basic importance to understand how the pentacene backbone shows such an impressive performance compared to other polyacene backbone structures. Recently, one of the PAHs, perylene was reexamined by several groups [7–9]. Carrier mobility of perylene TFT was reported several orders of magnitudes lower than that of single crystal on the basis of time-of-flight measurements. The mobility of OTFTs can generally be explained by the hopping transport model, wherein thermally activated mobility is dominant around room temperature [10,11], and charge transport is limited by grain boundaries in the polycrystalline thin films [12]. On the other hand, highly ordered molecular crystals were investigated mainly by using time-of-flight measurements of the mobility, where the mobility in highly pure defect-free crystals follows an inverse power-law

temperature dependence [13]. It appears to be generally recognized that the mobility of OTFTs could be placed in an intermediate region between the hopping model and a band-like transport model, such as the small polaron theory [14]. In order to interpret such a carrier transport mechanism and to design novel materials with high mobility, the theoretical calculations are powerful tool for organic semiconductive materials with the semi-empirical level to the first-principle level of theory and, indeed, such calculations have been carried out by many groups [15–19].

In this chapter, we focus on PAHs and clarify the underlying physics of the semiconductor performance from several microscopic viewpoints, i.e. the molecular electronic structure, the native packing mode of the molecules, and the resulting electronic band structure of two-dimensional molecular layer extracted from the bulk structure. To this end, we fabricated several OTFTs including pentacene (Pen), ovalene (Ov), dibenzocononene (DBC) and hexabenzocoronene (HBC), and characterized their field-effect mobilities. The fabricated PAH thin films were also analyzed by means of X-ray diffraction (XRD) for the molecular orientation of the ordered packing structure and atomic force microscopy (AFM) for the grain size.

2.2 Experimental procedure

2.2.1 Preparation of PAH films

All the PAHs except for pentacene were obtained from Dr. Ehrenstorfer GmbH (Augsburg, Germany), and pentacene was purchased from Aldrich. 50-nm-thick vacuum-deposited thin films were prepared on substrates with electrodes at a pressure of 10^{-6} Pa with deposition rates ranging from 0.2 to 0.4 Å/s. The temperature of the substrate was maintained at 40 °C throughout all the depositions. Heavily doped silicon with 200-nm-thick silicon dioxide at the surface was used as the substrate. Gold source and drain electrodes were prepared using photolithographic methods; electron beam deposition of 25/5-nm-thick Au/Ti, and cleaning by reactive-ion etching after the lift-off process. The bottom-contact configuration was adopted as the

geometry of the transistors with a channel width (W) of 500 μm and a channel length (L) of 50 μm.

2.2.2 Characterization of PAH films

The field effect mobility μ was calculated in the saturation region from the slope of the linear part of an $I_{d,sat}^{1/2}$ vs. V_g plot, using the following equation,

$$I_{d,sat} = \frac{WC_{ox}}{2L}\mu\left(V_g - V_{th}\right)^2, \tag{2-1}$$

where C_{ox}, V_g and V_{th} are capacitance of the insulator per unit area, gate voltage, and threshold voltage, respectively. V_{th} can be estimated from the intercept of a line drawn through the linear region of the $I_{d,sat}^{1/2}$ vs. V_g plot. The electrical properties were measured with a semiconductor parameter analyzer, the Keithley 4200SC, and the TFTs were placed under reduced pressure of 10^{-4} Pa for the electrical properties measurements. The TFT characteristics in ambient were not evaluated, since we want to eliminate extrinsic effects upon the electrical performances, such as oxygen and moisture, and so on.

XRD patterns with the conventional Bragg–Brentano set up were taken with the Rint-2500 (Rigaku Co.) instrument using a Cu target (λ = 1.54 Å). AFM measurements for the morphological characterization of the thin films were carried out with the Nanoscope IIIa (Digital Instruments), and all observations were performed using tapping mode of AFM with an NCH-10T probe.

2.3 Computational method

The electronic structures of the PAHs were calculated using the first-principles simulation software DMol^3 [20,21]. All-electron calculations were carried out within the density functional theory (DFT) level, where the exchange-correlation functional was parameterized according to the Perdew–Burke–Ernzerhof gradient corrected

exchange functional [22] within the generalized gradient approximation [23].

In the calculations, the localized numerical linear combination of atomic orbital was adopted in all the band structure calculations with a double set of numerical valence functions including a polarization d-function on all non-hydrogen atoms and a p-function on hydrogen atoms with the local basis cutoff R_c of 7.0 atomic units. The **k**-points mesh was sampled according to the Monkhorst–Pack scheme [24] with a **k**-point separation of 0.04 $Å^{-1}$.

We adopted the initial structures of the PAHs from the entries in the Cambridge Crystal Structural Database. The atomic coordinates of each crystal structure were optimized by keeping the lattice parameters same as those of the original crystal structure data. In the case of DBC, since the crystal structure in the database dose not contain the coordinates of the hydrogen atoms, the hydrogen atoms were inserted to the carbon atoms at the edge of the skeleton, and the geometry was optimized.

Two-dimensional molecular layer structures, which include the vacuum layer of 50 Å along the direction perpendicular to the slab planes, were constructed from the above-mentioned crystal coordinates with reference to XRD analysis to select the appropriate layer. Finally the band structures of the PAHs corresponding to the conduction sheets within the channel area in the TFT devices were calculated for the two-dimensional sheet structure. Furthermore, the energy band dispersions obtained from the first-principles calculations were analyzed on the basis of tight-binding approximation, to estimate electronic interaction between the neighboring molecules.

2.4 Results and discussion

2.4.1 Crystalline structure of thin films

Figure 2.1 shows the chemical structure of PAHs that were used in this chapter, and the corresponding crystal structural data are listed in Table 2.1 [25–28]. These PAHs could be divided into two groups, i.e. herringbone for Pen and γ for Ov, DBC, and HBC.

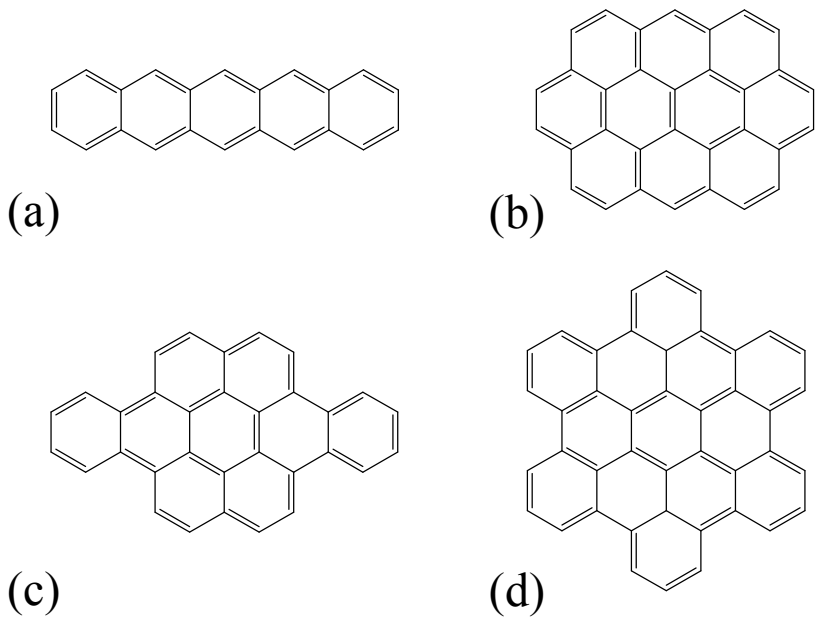

Figure 2.1: Structures of polycyclic aromatic hydrocarbons; (a) pentacene, (b) ovalene, (c) dibenzocoronene, and (d) hexabenzocoronene.

Table 2.1: Crystal structure of polycyclic aromatic hydrocarbons.

Compound	Formula	Space group	Z	*a*	b	c	*α*	*β*	*γ*
Pentacene	$C_{22}H_{14}$	P-1	2	6.27	7.78	14.53	76.48	87.68	84.68
Ovalene	$C_{32}H_{14}$	$P2_1/a$	2	19.47	4.7	10.12	90	105	90
Dibenzocoronene	$C_{32}H_{16}$	C2/c	4	22.83	5.22	15.77	90	103.9	90
Hexabenzocoronene	$C_{42}H_{18}$	$P2_1/a$	2	18.43	5.12	12.93	90	112.57	90

Figure 2.2 shows the XRD patterns of PAH films. The assignment of diffraction peaks and their interlayer spacing is based on XRD patterns of the original crystal data. The simulated *d* spacing values of the corresponding planes are *d*(0 0 1) = 14.1 Å for Pen, *d*(0 0 1) = 9.8 Å for Ov, *d*(2 0 0) = 11.1 Å for DBC and *d*(0 0 1) = 11.9 Å for HBC. All the estimated lattice planes indicate that the two-dimensional networks of π-orbital overlap between neighboring molecules are constructed parallel to substrate. The *d* spacing of HBC thin film is in good agreement with that of crystal structure, and two phases coexist in the film. In contrast, the inset values of the *d* spacing in Figure 2.2 for Pen, Ov and DBC have discrepancy of 1–2 Å. We consider that the difference in the *d* spacing should be derived from the structural difference between thin-film and bulk phases. It is well recognized that Pen films generally show two distinct crystalline phases, a thin-film phase with *d* = 15.4 Å, and a bulk phase with *d* = 14.4 Å [29]. Both phases are observed in the XRD pattern for the Pen film in this chapter. Moreover, the corresponding edge-to-edge lengths (including van der Waals radii) of Pen, Ov, and DBC molecules are 16.2, 12.7, and 11.6 Å, respectively. The inclination of PAH molecule on substrate in the thin-film phase is different from that in the bulk phase; the tilt angles of Pen and Ov decrease, while DBC is expected to be more inclined in the thin films.

For the first-principles calculations, we selected the assigned lattice plane as the intrinsic layer for the compound and constructed a monolayer slab model for each PAH. Since the crystal structure of thin-film phase is slightly different from those of bulk phase as is shown above, it is desirable to determine the crystal structure of thin-film phase and apply the structure for the first-principles calculations. However, it is difficult to determine the in-plane lattice parameters of thin film with the conventional XRD analysis. Thus, the bulk phase structures based on the crystal structure were taken into consideration in the calculation. In addition, in the case of the ideal OTFT model, since most of the accumulated carriers at the interface between insulator and semiconductor are expected to distribute within one or two molecular layer(s) from the interface [6], transfer integrals between the neighboring molecules

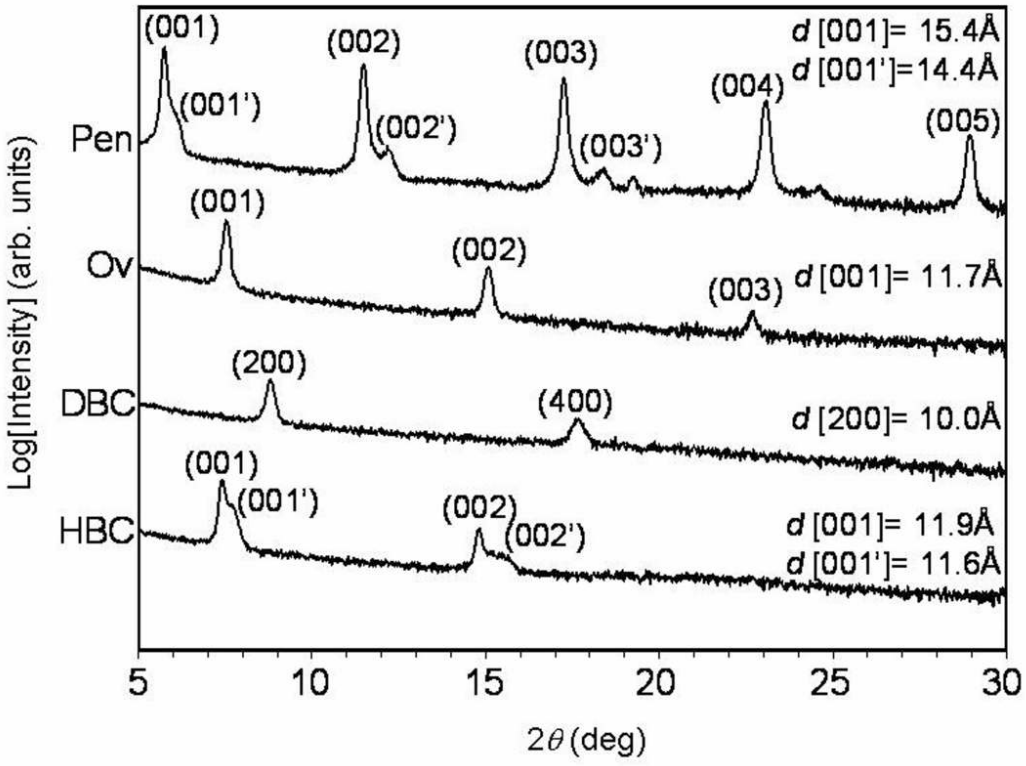

Figure 2.2: XRD patterns of Pen, Ov, DBC and HBC. The inset values indicate *d* spacings for the main peaks.

within the two-dimensional molecular layer is crucial for the mobility of OTFTs. Moreover, the typical transfer integral between molecules in the different molecular layers could be estimated to be on the order of 10^{-4}–10^{-3} eV. Therefore, we consider that one slab layer model should be enough to evaluate the transfer integrals between the adjacent molecules within the conduction sheet.

2.4.2 Electronic structure and field-effect mobility

Figure 2.3 shows the output characteristics of PAH-TFTs. The obtained field-effect mobilities of OTFTs are 0.17, 8.9×10^{-4}, 1.5×10^{-4} and 3.0×10^{-4} cm^2/Vs, and the threshold voltages are 24.9, 20.5, 12.4 and 18.4 V for Pen, Ov, DBC and HBC, respectively. Each PAH-TFT exhibited relatively low on/off ratios ranging from 10^2 to 10^3. The Pen-TFT exhibited outstandingly higher carrier mobility than the others. We examined the difference in the carrier mobilities obtained in this chapter, based on the first-principles calculation of band structure. For the first principles calculations, we considered monolayer slab models for each PAH, where the bulk phase structures based on the crystal structure were taken into consideration in the calculation.

Figure 2.4 shows the band energy dispersions of PAHs obtained from the calculations. The band gap values are 0.76, 1.74, 2.08, and 1.85 eV for Pen, Ov, DBC, and HBC, respectively. All values of the band gap were underestimated, as is commonly reported in the DFT calculations. UV–Visible spectra were measured for all PAH films, and the band gaps estimated from the absorption band edges are 2.07, 2.26, 2.84, and 2.82 eV for Pen, Ov, DBC, and HBC, respectively. We note that in the case of Pen film, the absorption band from 600 to 700 nm are assigned as Davidov splitting and are not taken into consideration for estimation of the band gap. We focused on the valence bands, since all PAH-TFTs showed *p*-type behavior. For simplicity, the bands derived from the highest occupied molecular orbital (HOMO) and the lowest unoccupied molecular orbital (LUMO) levels were extracted in Figure 2.4, because the molecular orbitals related to carrier conduction of holes and electrons are HOMO and LUMO, respectively. All PAHs have two nonequivalent molecules in the

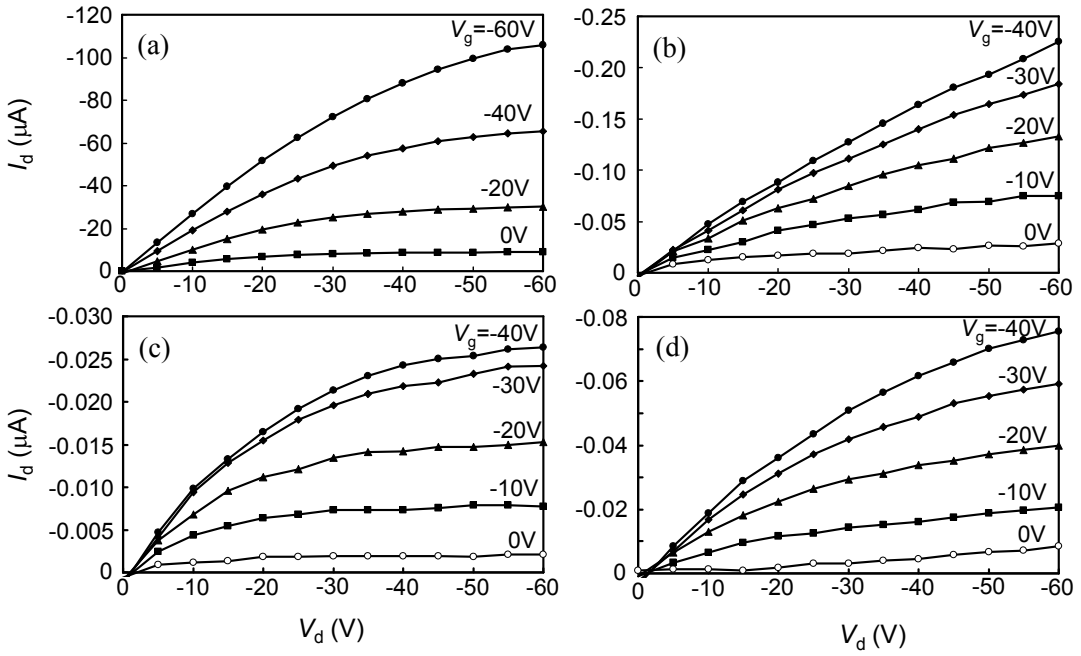

Figure 2.3: Output characteristics of PAH-TFTs, (a) Pen, (b) Ov, (c) DBC and (d) HBC. The transistor geometry is *W/L*= 500/50 μm.

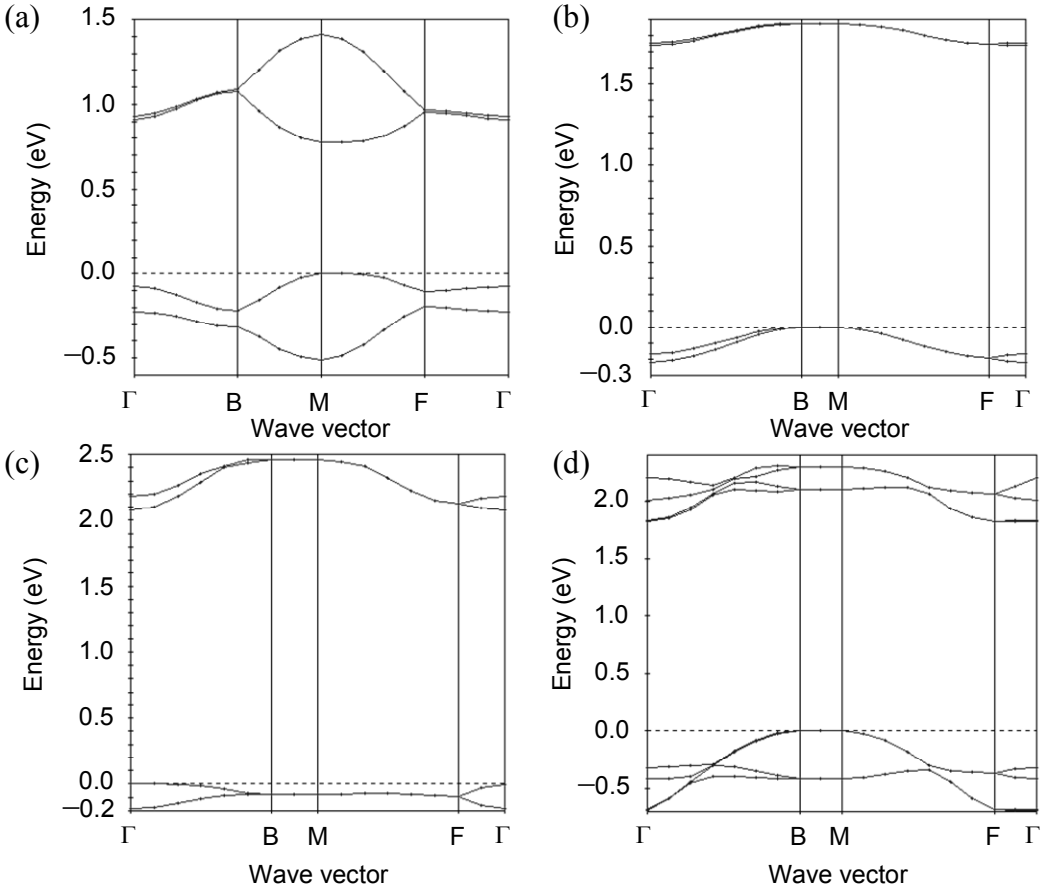

Figure 2.4: Energy band dispersion of PAHs for the bands derived from HOMO and LUMO levels for (a) Pen, (b) Ov, (c) DBC and (d) HBC, where **k**-point paths correspond to the conductive sheet in the TFT channel; Γ = (0, 0, 0), B = (a^*/2, 0, 0), M = (a^*/2, b^*/2, 0), F = (0, b^*/2, 0). In the 2D energy band calculation for Ov, DBC and HBC, *b*- and *c* axis of crystal structure was redefined as *a*- and *b* axis, respectively. Dashed lines represent the energy level at the valence band maximum.

unit cell of molecular layer, and therefore two bands are obtained respectively for HOMO and LUMO bands. In the case of HBC, HBC molecule itself has degenerate HOMO and LUMO and results in four bands in the HOMO and LUMO bands respectively. In the energy dispersion, the degeneracy is confirmed to split owing to transfer integrals between the two degenerate orbitals, HOMO1 and HOMO2 (LUMO1 and LUMO2) in the equivalent molecules [30]. Therefore, the upper two HOMO bands should be derived from the interaction between the same HOMOs for each nonequivalent molecule in the unit cell.

2.4.3 Background of tight-binding approximation

In the simple model, the energy band dispersion is expressed by

$$\varepsilon_k = -\alpha - 2\beta\cos(\mathbf{k}\cdot\mathbf{r}), \tag{2-2}$$

where **k** is the wave vector, α is the one-center Coulomb term, β is the transfer integral between the nearest neighbors, and **r** is the lattice vector of the two-dimensional square lattice [31]. The effective mass, m^*, is defined as

$$m^* = -\hbar^2\left(\frac{\partial^2\varepsilon}{\partial k^2}\right)^{-1}. \tag{2-3}$$

At the valence band maximum, equations (2-2) and (2-3) lead to

$$m^* = -\frac{\hbar^2}{2\beta a^2} = -\frac{4\hbar^2}{Ba^2}, \tag{2-4}$$

where the lattice constant is defined as a for both axes isotropically. In the case of the two-dimensional square lattice, the bandwidth (B) is 8β. When the Drude form of the mobility, $\mu = e\ \tau / m^*$, is taken into consideration, the mobility should be inversely proportional to the effective mass. Thus, the large bandwidth, attributed to the large transfer integral between neighboring molecules, should result in high carrier mobility. However, it is not straightforward to connect the HOMO bandwidth and FET mobility

directly, since thin films of organic semiconductors form granular structure and consist of many grain boundaries, which were proposed to reduce the carrier mobility [32]. On the other hand, a hopping-like electron transport mechanism based on the semi-classical Marcus–Hash theory has been considered at the microscopic level [33]. In the literature, the electron transfer rates for self-exchange reactions are determined by the transfer integral and the reorganization energy. The larger interactions of π-electrons between neighboring molecules and the smaller structural reorganization energy in the charge transitions could lead to faster charge transport. As a result, in both band and hopping transport, intermolecular electronic interactions are important for carrier transport.

We examined this point, looking into the difference among PAHs in terms of intermolecular interactions. To this end, tight-binding approximation approaches were adopted to describe the system as isolated molecules with a term for the overlap of molecular orbitals referred to in equation (2-2) [34,35]. We briefly introduce the background for this method below. Here, the tight-binding Bloch orbitals are presented as follows:

$$\psi_k(\mathbf{r}) = (1/N)^{1/2} \sum_n \left[\sum_j \phi_j(\mathbf{r} - \mathbf{R}_n) C_j(\mathbf{k}) \right] \exp(i\mathbf{k} \cdot \mathbf{R}_n), \tag{2-5}$$

where N is the number of molecules in the unit cell, $\mathbf{R}_n$ is the lattice vector, and $\phi_j(\mathbf{r}-\mathbf{R}_n)$ is the jth molecular orbital, which is the component of the valence band related to hole conduction, in the nth cell. $C_j(\mathbf{k})$ is the coefficient for linear combination of the molecular orbital at a certain $\mathbf{k}$-point. Based on a variational principle, $C_j(\mathbf{k})$ is determined to satisfy the equation:

$$\frac{\partial}{\partial C_j}\left[\langle \psi_k | H | \psi_k \rangle - \varepsilon(k) \langle \psi_k | \psi_k \rangle\right] = 0, \tag{2-6}$$

where H is a total Hamiltonian of the crystal. In the simplified form of the tight-binding scheme, the eigenvalue $\varepsilon(\mathbf{k})$ is determined by solving the secular equations,

whose order corresponds to the number of HOMOs in one unit cell with respect to the valence band. In the case of the PAHs examined in this chapter, we take into account that two nonequivalent molecules present in an unit cell. All these lead to the following eigenvalue problem,

$$\begin{vmatrix} E_1 - T_1 - \varepsilon(\mathbf{k}) & T_2 \\ T_2 & E_1' - T_1 - \varepsilon(\mathbf{k}) \end{vmatrix} = 0, \tag{2-7}$$

where $\varepsilon(\mathbf{k})$ is the eigenvalue at a certain **k**-point, E_1 is a molecular energy, T_1 represents the sum of the transfer integrals between the equivalent molecules, and T_2 is the sum of the transfer integrals between nonequivalent molecules. Each of these terms is denoted below,

$$E_1 = \langle \phi_a | H | \phi_a \rangle, \tag{2-8}$$

$$T_1 = \sum_n \exp(i\mathbf{k} \cdot \mathbf{R}_n) \langle \phi_a(\mathbf{r}) | H | \phi_a(\mathbf{r} - \mathbf{R}_n) \rangle, \tag{2-9}$$

$$T_2 = \sum_m \exp(i\mathbf{k} \cdot \mathbf{R}'_m) \langle \phi_a(\mathbf{r}) | H | \phi_b(\mathbf{r} - \mathbf{R}'_m) \rangle, \tag{2-10}$$

where, in equation (2-10), $\mathbf{R}'_m$ represents the vectors in real space to connect nonequivalent neighboring molecules to each other. The solutions of equation (2-7) are fitted to the eigenvalues previously obtained from first-principles calculations. These fitting calculations are performed at each **k**-point.

2.4.4 Transfer integrals between neighboring molecules

Table 2.2 shows that Ov and DBC, showing much lower mobilities than Pen, have narrow bandwidths of HOMO accompanied by small transfer integrals. Such low mobilities for Ov and DBC could be deduced from the transfer integrals in the molecular crystals where the carrier transport might be described simply by the hopping model. In other words, both Ov and DBC are predicted to exhibit intrinsically low carrier mobility not only in OTFTs but also in single crystals. One contradiction is that HBC showed low mobility of OTFT, in spite of the calculated widest HOMO band

energy dispersion. We compared the transfer integrals for Pen and HBC in detail with respect to the individual directions within the *a*-*b* plane. All *t*-values are absolute values, and the subscript denotes the direction of the neighboring molecule with electronic interaction in real space as shown in Figure 2.5. Comparing the respective transfer integrals, we note that Pen has relatively two-dimensional interaction between the neighboring molecules, while HBC has only one-dimensional interaction along the *a*-axis, which corresponds to the direction of π-π stacking.

In addition, according to semi-classical Marcus electron-transfer theory [33,36–38], the electron-transfer rate constant for self-exchange reaction is approximately described as

$$k_{\mathrm{et}} = \left(\frac{2\pi}{\hbar}\right) t^2 \left(4\pi\lambda k_{\mathrm{B}} T\right)^{-1/2} \exp\left(\frac{-\lambda}{4k_{\mathrm{B}} T}\right), \tag{2-11}$$

where t and λ are transfer integral and reorganization energy that consists of inner and outer parts. Here, the outer part of the reorganization energy is neglected, since there is no solvent around the charge-transfer site. The inner part of the reorganization energies for hole carrier transition between adjacent molecules were also calculated by using a first-principles simulation [39]. The reorganization energies for Pen, Ov, DBC, and HBC are 0.084, 0.142, 0.081, and 0.194 eV, respectively. k_{et} at temperature 300K are estimated from equation (2-11) by using the reorganization energies and the maximum transfer integrals for each PAHs in Table 2.2. As a result, k_{et} of Pen (10^{14} s^{-1}) is estimated to be one order of magnitude higher than those of Ov, DBC, and HBC (10^{13} s^{-1}). Therefore, Pen is expected to exhibit intrinsically higher carrier mobility than the other PAHs. Nevertheless, the difference of three orders of magnitude in the TFT mobility can not be explained only from the microscopic viewpoint.

2.4.5 Grain size of PAH thin films

We now briefly consider the morphological factors affecting carrier mobility. Figure 2.6 shows the surface morphologies of Pen, Ov, DBC and HBC observed by

Table 2.2: Transfer integrals between nearest neighboring molecules for respective direction and band width of HOMO and LUMO bands with respect to each PAH.

		Pen		Ov		DBC		HBC	
		HOMO	LUMO	HOMO	LUMO	HOMO	LUMO	HOMO	LUMO
t_a	(meV)	27.4	34.7	47.9	32.4	4.5	84.7	87.2	60.3
t_b	(meV)	2.9	5.3	0.07	0.10	0.10	0.05	0.3	1.1
$t_{(a+b)/2}$	(meV)	47.3	78.6	0.28	1.6	22	1.3	8.7	3.5
$t_{(a-b)/2}$	(meV)	77.2	78.2	0.27	1.7	22.8	1.4	10.1	3.6
Bandwidth	(eV)	0.51	0.64	0.22	0.14	0.18	0.38	0.69	0.49

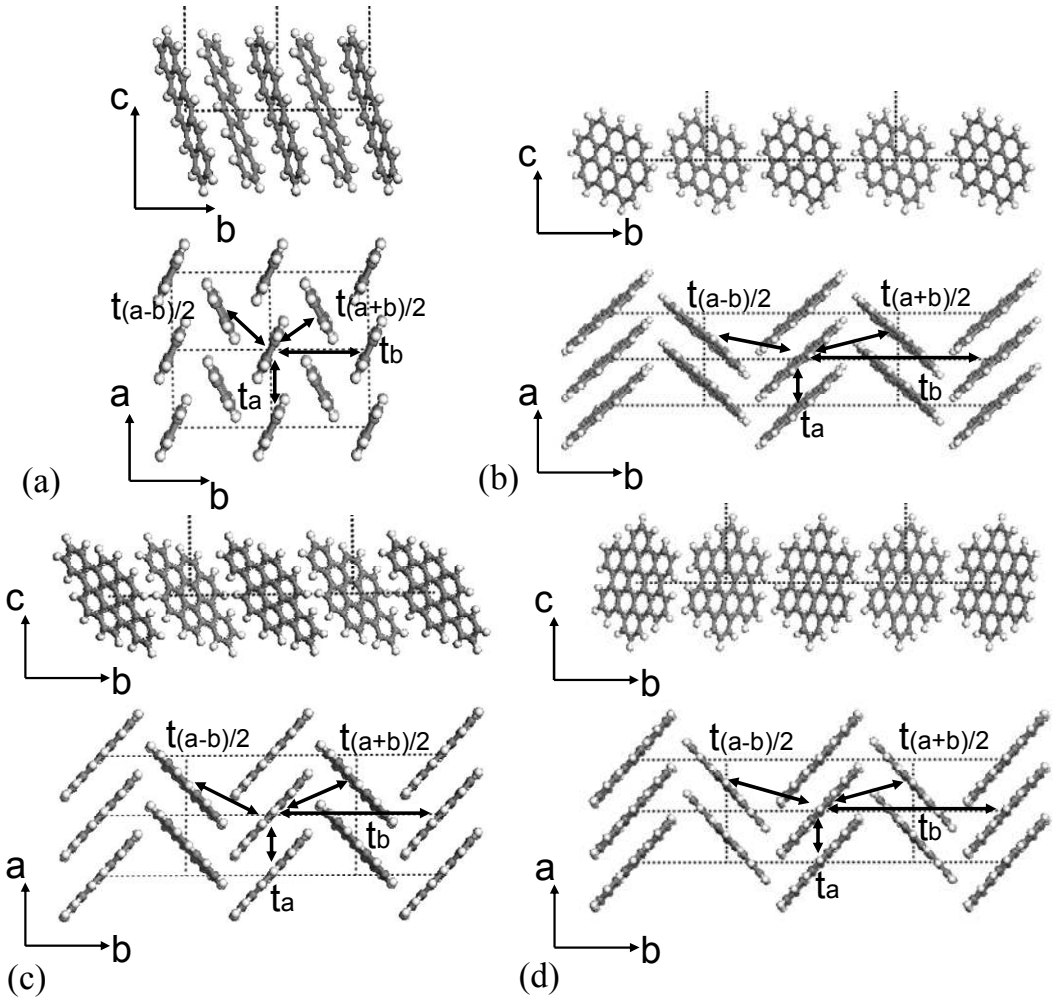

Figure 2.5: Structures of a molecular layer for each PAH viewed from the *c*- and *a* axis for (a) Pen, (b) Ov, (c) DBC and (d) HBC. The arrows represent the direction of different transfer integrals.

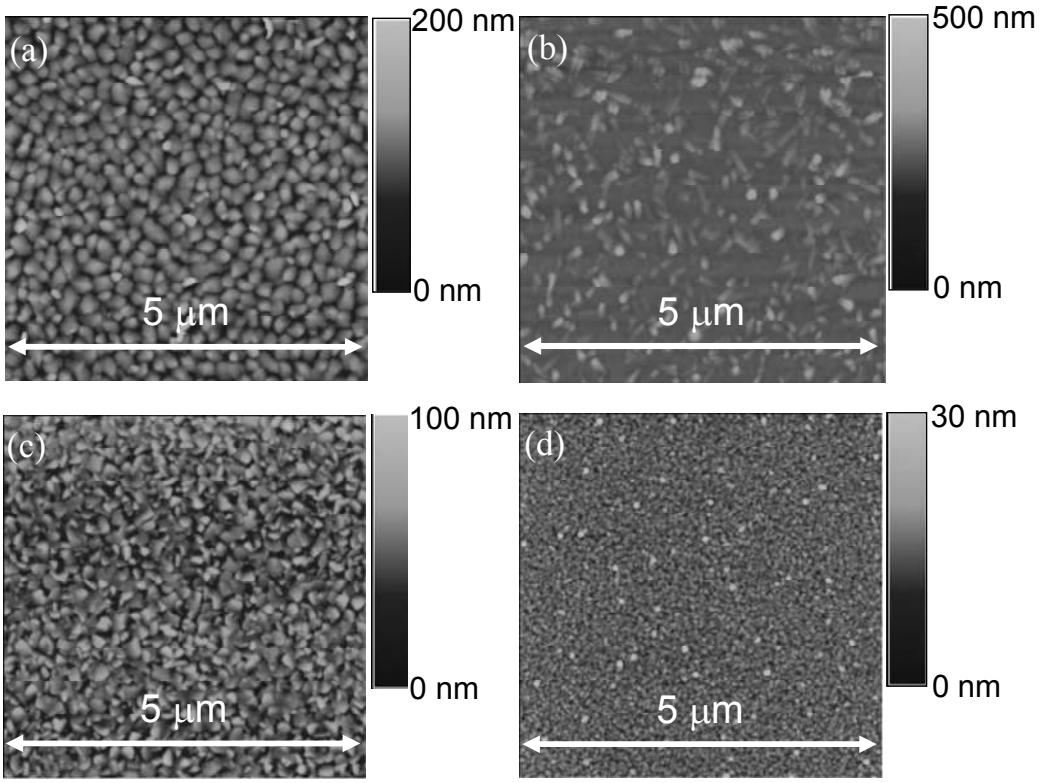

Figure 2.6: Surface morphologies of (a) Pen, (b) Ov, (c) DBC and (d) HBC. The scan area is $5 \times 5\ \mu m^2$ for all images.

AFM. All grains formed a columnar shape and we define the grain size parameter as an average valley-to-valley distance of the height data arbitrarily sampled from the cross sections of the AFM images. The grain size of Pen was approximately 200 nm, which is the largest among the samples examined, while Ov, DBC and HBC showed small grain size of 90, 80 and less than 50 nm, respectively. The Ov, DBC, and HBC thin films include more grain boundaries than Pen film, where the charge transport will be reduced by trap states. This must be an additional reason why Ov, DBC, and HBC TFTs show lower TFT mobility than Pen-TFT. Furthermore, it is possible that other predominant factors, reducing TFT mobility, exist in the Ov, DBC, and HBC TFTs, such as structural defects, impurities, trap states at the insulator/semiconductor interface, and so on.

2.5 Conclusion

We have investigated the structures of PAH thin films and the carrier mobility of OTFTs fabricated using these PAH thin films. The Pen-TFT showed the highest carrier mobility among the PAHs investigated in this chapter. According to the XRD analysis, it was found that all PAH molecules formed the π-interaction sheet parallel to substrates. The energy band structures of a molecular layer for PAHs were performed using first-principles calculations, where the plane of molecular layer was defined on the basis of the XRD analysis of the PAH thin films. The electronic interaction between neighboring molecules was also estimated in detail within the tight-binding approximation. It was revealed that Ov and DBC has small transfer integral resulting in the narrow bandwidth of HOMO, and that though HBC has a larger transfer integral than Pen, it only has a one-dimensional interaction with the neighboring molecules. In addition to that, further theoretical investigation based on Marcus electron-transfer theory was carried out and revealed that Pen was expected to exhibit intrinsically higher carrier mobility than the other PAHs by one order of magnitude or so, owing to both large overlap integral and small reorganization energy. Furthermore, AFM

observations of the PAH thin films showed that Pen film had fewer grain boundaries than the others. Since chemical or physical defects in the grain boundary should act as trapping states and scattering centers in the carrier transport, the mobility of Pen-TFT will be less affected by the extrinsic factors than the other PAHs.

References

1) B. Crone, A. Dodabalapur, Y. -Y. Lin, R. W. Filas, Z. Bao, A. LaDuca, R. Sarpeshkar, H. E. Katz, W. Lin, *Nature* **403**, 521 (2000).

2) P. F. Baude, D. A. Ender, M. A. Haase, T. W. Kelly, D. V. Muyres, S. D. Theiss, *Appl. Phys. Lett.* **82**, 3964 (2003).

3) B. Crone, A. Dodabalapur, A. Gelperin, L. Torsi, H. E. Katz, A. J. Lovinger, Z. Bao, *Appl. Phys. Lett.* **78**, 2229 (2001).

4) Y.-Y. Lin, D. J. Gundlach, S. F. Nelson, T. N. Jackson, *IEEE Electron Device Lett.* **18**, 606 (2002).

5) C. D. Dimitrakopoulos, P. R. L. Malenfant, *Adv. Mater.* **14**, 99 (2002).

6) G. Horowitz, *J. Mater. Res.* **19**, 1946 (2004).

7) N. Karl, K.-H. Kraft, J. Marktanner, M. Münch, F. Schatz, R. Stehle, H.-H. Uhde, *J. Vac. Sci. Technol. A* **17**, 2318 (1999).

8) S.-H. Kim, Y.-S. Yang, J.-H Lee, J.-I. Lee, H.-Y. Chu, H. Lee, J. Oh, L.-M Do, *Opt. Mater.* **21**, 439 (2002).

9) M. Kotani, K. Kakunuma, M. Yoshimura, K. Ishii, S. Yamazaki, T. Kobori, H. Okuyama, H. Kobayashi, H. Tada, *Chem. Phys.* **325**, 160 (2006).

10) M. C. J. M. Vissenberg, M. Matters, *Phys. Rev. B* **57**, 12964 (1998).

11) L. Torsi, A. Dodabalapur, L. J. Rothberg, A. W. P. Fung, H. E. Katz, *Phys. Rev. B* **57**, 2271 (1998).

12) R. Bourguiga, G. H. Horowitz, F. Garnier, R. Hajlaoui, S. Jemai, H. Bouchriha, *Eur. Phys. J. Appl. Phys.* **19**, 117 (2002).

13) W. Warta, N. Karl, *Phys. Rev. B* **32**, 1172 (1985).

14) T. Holstein, *Ann. Phys.* **8**, 343 (1959).

15) R. C. Haddon, X. Chi, M. E. Itkis, J. E. Anthony, D. L. Eaton, T. Siegrist, C. C. Mattheus, T. T. M. Palstra, *J. Phys. Chem. B* **106**, 8288 (2002).

16) A. Troisi, G. Orlandi, *J. Phys. Chem. B* **109**, 1849 (2005).

17) J. Cornil, J. -P. Calbert, D. Beljonne, R. Silbey, J. -L. Brédas, *Adv. Mater.* **12**, 978 (2000).

18) J. Cornil, J. -P. Calbert, J. L. Brédas, *J. Am. Chem. Soc.* **123**, 1250 (2001).

19) Y. C. Cheng, R. J. Silbey, D. A. da Silva Filho, J. P. Calbert, J. Cornil, J. -L. Brédas, *J. Chem. Phys.* **118**, 3764 (2003).

20) B. Delley, *J. Chem. Phys.* **92**, 508 (1990).

21) B. Delley, *J. Chem. Phys.* **113**, 7756 (2000).

22) J. P. Perdew, K. Burke, M. Ernzerhof, *Phys. Rev. Lett.* **77**, 3865 (1996).

23) J. P. Perdew, J. A. Chevary, S. H. Vosko, K. A. Jackson, M. R. Pederson, D. J. Singh, C. Fiolhais, *Phys. Rev. B* **46**, 6671 (1992).

24) H. J. Monkhorst, J. D. Pack, *Phys. Rev. B* **13**, 5188 (1976).

25) C. C. Mattheus, A. B. Dros, J. Baas, A. Meetsna, J. L. de Boer, T. T. M. Palstra, *Acta Crystallogr. C* **57**, 939 (2001).

26) J. M. Robertson, J. Trotter, *J. Chem. Soc.* 1115 (1961).

27) R. G. Hazell, G. S. Pawley, Z. *Kristallogr., Kristallgeom., Kristallphys., Kristallchem.* **137**, 159 (1973).

28) R. Goddard, M. W. Haenel, W. C. Herndon, C. Kruger, M. Zander, *J. Am. Chem. Soc.* **117**, 30 (1995).

29) C. D. Dimitrakopoulos, A. R. Brown, A. Pomp, *J. Appl. Phys.* **80**, 2501 (1996).

30) J. Kirkpatrick, *Int. J. Quantum Chem.* **108**, 51 (2008).

31) R. C. Haddon, T. Siegrist, R. M. Fleming, P. M. Bridenbaugh, R. A. Laudise, *J. Mater. Chem.* **5**, 1719 (1995).

32) D. Knipp, R. A. Street, A. Völkel, J. Ho, *J. Appl. Rhys.* **93**, 347 (2003).

33) C. R. Newman, C. D. Frisbie, D. A. da Silva Filho, J. -L. Brédas, P. C. Ewbank, K. R. Mann, *Chem. Matter.* **16**, 4436 (2004).

34) G. A. de Wijs, C. C. Mattheus, R. A. de Groot, T. T.M. Palstra, *Synth. Met.* **139**, 109 (2003).

35) Troisi, G. Orlandi, *J. Phys. Chem. B* **109**, 1849 (2005).

36) R. A. Marcus, *Rev*. *Mod*. *Phys*. **65**, 599 (1993).

37) P. F. Barbara, T. J. Meyer, M. A. Ratner, *J*. *Phys*. *Chem*. **100**, 13148 (1996).

38) V. Balzani, A. Juris, M. Venturi, S. Campagna, S. Serroni, *Chem*. *Rev*. **96**, 759 (1996).

39) M. Malagoli, J. -L. Brédas, *Chem*. *Phys*. *Lett*. **327**, 13 (2000).

Chapter 3

Crystal structure and electronic properties of solution-processed pentacene thin film

3.1 Introduction

Organic semiconductors can be applied to solution process with the flexible substrates, such as plastic panels, at lower temperature than the conventional processes for inorganic semiconductors. Recently, novel soluble materials have been studied vigorously by several groups [1–5]. Although one of the most promising candidates, pentacene, shows high carrier mobility comparable to amorphous silicon, it has been used for the source of vacuum deposition because of its low solubility in solvents. To obtain higher solubility in the pentacene-related materials, it is generally considered to be necessary to modify molecular structure of pentacene by introducing some functional groups. Diels–Alder-adducted pentacene derivatives, for example, were investigated to form the solution-processed thin films [6,7]. In their process, pentacene precursors were spin-coated on the substrate in common solution such as chloroform or toluene, followed by annealing under nitrogen atmosphere at 130–180 °C to convert precursors into pentacene. These solution-processed organic thin film transistors (OTFTs) with bottom-contact configuration exhibited relatively high carrier mobility of 0.1–0.5 cm^2/Vs. Another approach is that bulky substituents such as triisopropylsilylethynyl (TIPS) group were introduced into pentacene to change molecular packing from herringbone structure to other two-dimensional π-stacked array. High solubility ranging from 0.2 to 3 wt% was reported as for so-called TIPS-pentacene [8]. In the case of TIPS-pentacene, these OTFTs showed carrier mobility ranging from 0.2 to 1.8 cm^2/Vs with an average mobility of 0.65 cm^2/Vs at a drain voltage of −40 V.

In this chapter, we present pentacene-based direct solution process of organic thin films, which did not require particular syntheses to obtain pentacene derivatives.

We will present detailed investigations into the structures of the solution-processed pentacene thin film using grazing incidence X-ray diffraction (GIXD) and atomic force microscopy (AFM). The lattice parameters of the solution-processed pentacene film are estimated from the two-dimensional (2D) mapping of the GIXD patterns. The electrical properties of solution-processed pentacene TFTs are also investigated with respect to the different surface morphologies.

3.2 Experimental procedure

Organic semiconductor pentacene was purchased from Tokyo Chemical Industry and was used without further purification. Commercially available 1,2,4-tricholorobenzene (TCB) was used as a solvent after distillation. Pentacene was added to TCB and heated at 200 °C to obtain 0.1 wt% solutions in a glove box under nitrogen atmosphere. The solution was dropped onto a substrate previously heated at 200 °C to form pentacene thin film by evaporating TCB.

Heavily doped silicon wafers with a 200-nm-thick silicon dioxide insulator were used as a substrate. The electrode geometry was same as described in section 2.2.1. The substrates were cleaned with oxygen plasma prior to preparation of the thin films. The specific surface treatment such as self-assembled monolayer was not utilized in this chapter.

The electrical properties of OTFTs were measured with a semiconductor parameter analyzer (Keithley 4200SC) under reduced pressure of 10^{-4} Pa. The field effect mobility μ was calculated in the saturation region from the slope of the linear part of an $I_{d,sat}^{1/2}$ vs. V_g plot, using equation (2-1).

The out-of-plane and in-plane structures of the solution-processed thin films were investigated by GIXD [9]. The GIXD measurement was performed using ATX-GSOR diffractometer with synchrotron radiation (λ = 0.99 Å) at the BL13XU in SPring-8. In addition, the 2D-mapping was also carried out to investigate the orientation of lattice plane within the thin film. The schematic image of GIXD

measurement is illustrated in Figure 3.1. In this method, the incident X-ray from grazing angle (typically < 0.5 degree) is radiated to the sample surface, and X-ray propagates in the surface to be diffracted with the lattice plane perpendicular to the substrate.

The surface morphology was observed by atomic force microscopy (AFM; Nano scope IIIa, Digital Instruments). All observations were performed using tapping mode of AFM with an NCH-10T probe.

3.3 Results and discussion

3.3.1 Solubilization of pentacene

UV-Visible absorption spectra of mixture of pentacene and TCB are shown in Figure 3.2, where all measurements were carried out under inert atmosphere. At room temperature, solid particles of pentacene remained in the solvent, and the color of dispersion was purple, which is original color of the solid-state pentacene. As the temperature of the solution was elevated from room temperature, the absorption between 600 to 700 nm disappeared, and the color of the solution changed into red-violet. The absorption band from 400 to 600 nm is attributed to π-π^* transition and relevant vibrational structure of pentacene molecule. This indicates that pentacene solution formed successfully by heating the dispersion under inert atmosphere.

3.3.2 Surface morphology

Figure 3.3 shows the surface morphology of solution-processed pentacene thin film observed by optical microscope. The surface morphology can be divided into two types of structure, i.e. rough domain and flat domain, and this figure exhibits the boundary between them. At the beginning of thin film growth, the rough domains, which include dendritic shape of crystal, tend to form from the edge of the substrate. In the course of thin film growth, the growth mechanism was assumed to change from dendritic growth to two-dimensional growth, and the stripe-patterned large domains of

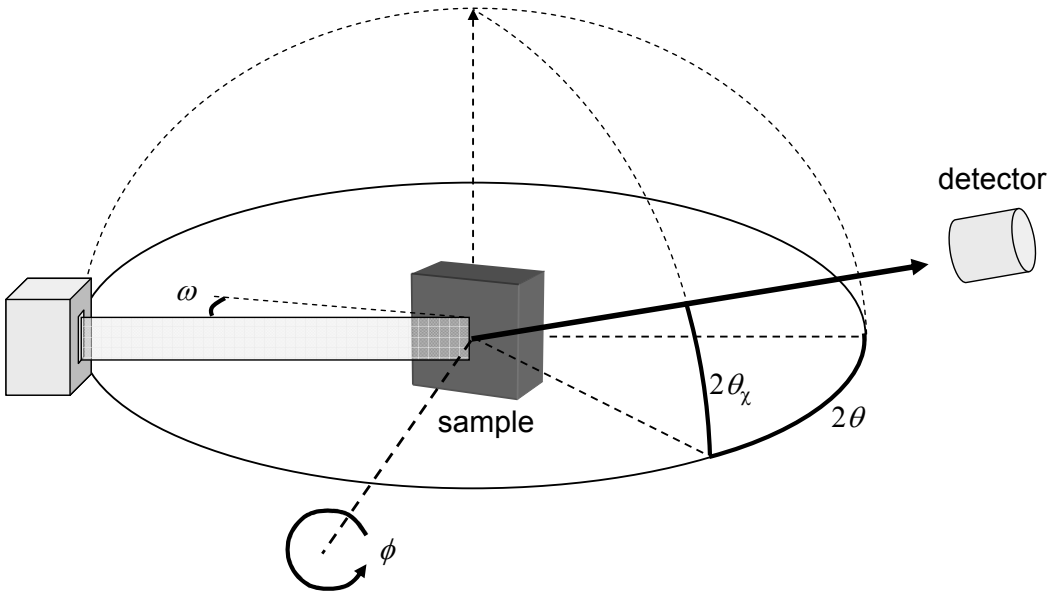

Figure 3.1: Schematic illustration of GIXD measurement. $2\theta_{\chi}$ is the diffraction attributed to in-plane structures, and ϕ is the rotation angle of sample for two-dimensional mapping.

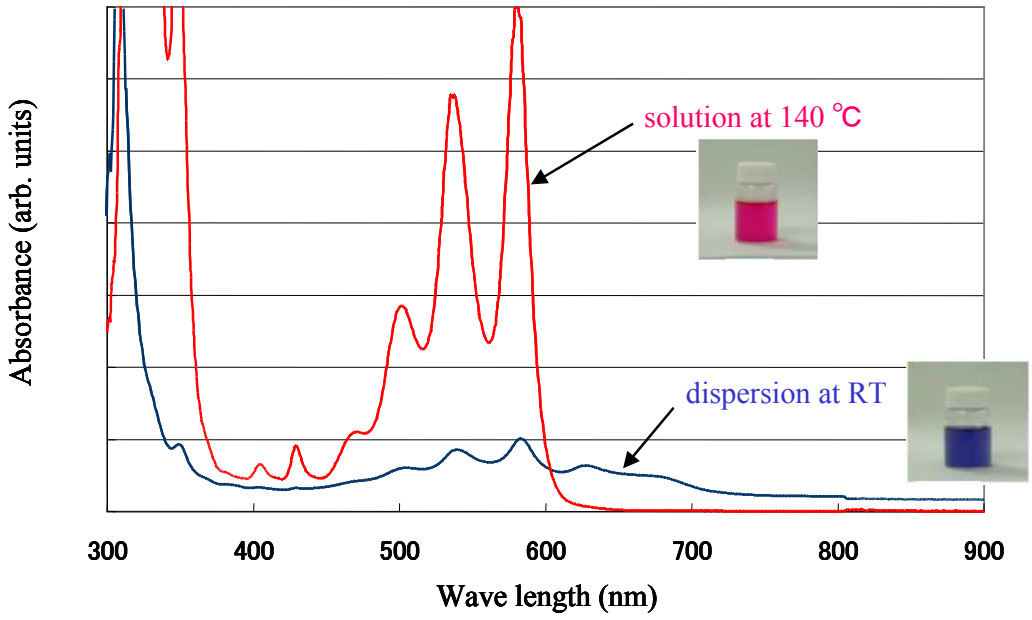

Figure 3.2: UV-Visible absorption spectrum of pentacene solution at room temperature and 140 °C.

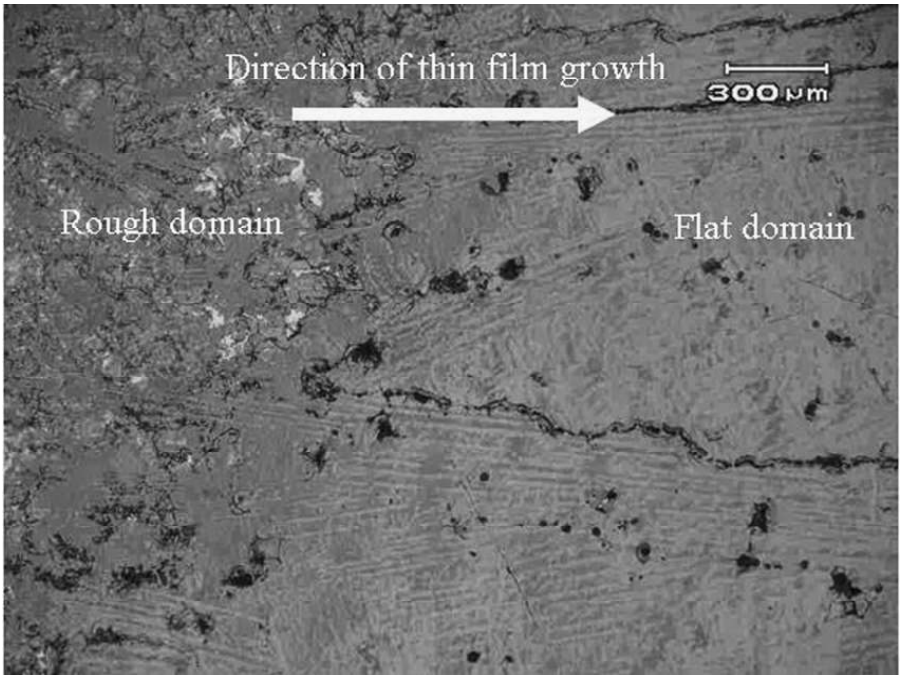

Figure 3.3: Optical microscope image of solution-processed pentacene thin film. Arrow represents the direction of thin film growth.

several hundred micrometers were formed in the flat domains.

The surface morphologies of the flat and rough domains observed by AFM are shown in Figure 3.4. The flat domain (Figure 3.4(a)) formed a continuous structure both on the channel area and the electrodes. This implies that the two-dimensional growth occurred at the surface of the solution and, afterwards, the film adhered to the substrate. The flat domain in Figure 3.4(a) contains grain boundary, in which approximately 5-μm particles exist. These particles should be generated mainly in the process of evaporating the residual solution between the thin film and the substrate after formation of the thin films. On the other hand, the rough domain (Figure 3.4(b)) showed the discontinuity in the films, where many grain boundaries were found in the channel region. In addition, the presence of small particles of a few micrometers is confirmed on the each grain in Figure 3.4(b). It is likely that frequent nucleation occurred simultaneously with domain growth in the solution because of enhanced supersaturation. Given the two different types of morphology, we focus on the flat domains in the following structural analysis. The average thickness of the flat domain was measured to be approximately 200 nm by cross-sectional profiling of the film.

3.3.3 Difference in transistor characteristics

The transfer characteristics of TFTs are shown in Figure 3.5. Both flat and rough domains exhibited steep subthreshold slope at similar turn-on voltage. The mobility and the threshold voltage are 0.21 cm^2/Vs and −2.3 V for the flat domain, and 0.07 cm^2/Vs and −10.3 V for the rough domain, respectively. With respect to the rough domain, the mobility showed lower than that of the flat domain because of the difference in the domain size and the crystallinity, and the threshold voltage shifted negatively compared with the flat domain. The method to estimate the trap density in the channel was reported in Ref. 10, where the difference between the threshold voltage and the turn-on voltage was used to calculate the trap density. The trap density at the interface between semiconductor and dielectric layer is expressed as follows,

$$N_{\text{trap}} = C_{\text{ox}} \left| V_{\text{th}} - V_{\text{on}} \right| / e , \tag{3-1}$$

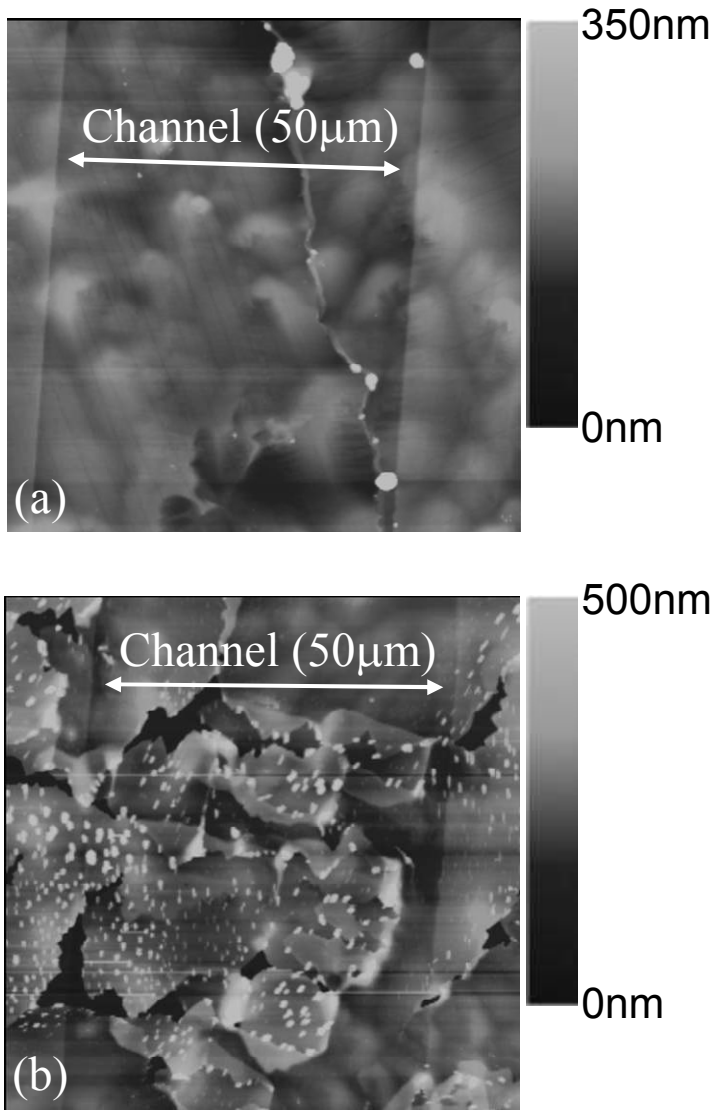

Figure 3.4: AFM height images of (a) flat domain and (b) rough domain. The channel area of transistors is displayed in both images.

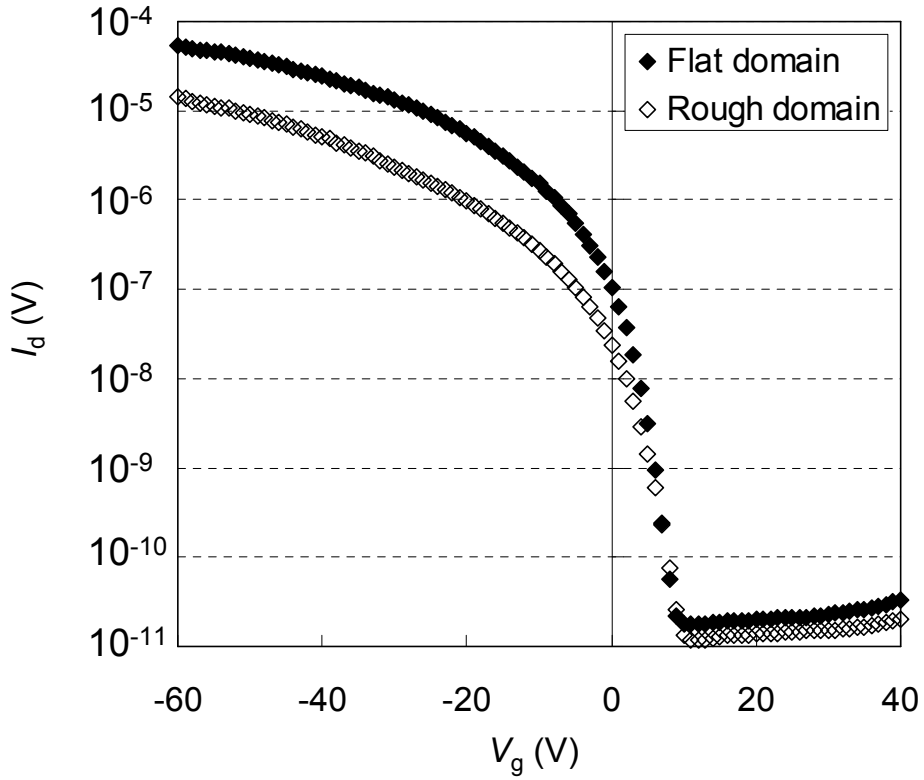

Figure 3.5: Transfer characteristics of solution-processed pentacene TFT with respect to the flat and rough domains. Applied voltage between source and drain is −60 V. The transistor geometry is W/L= 500/50 (μm).

where C_{ox} is the oxide capacitance per unit area and e is the elemental charge. The trap density per unit area was estimated to be 1.2×10^{12} cm^{-2} for the flat domain and 2.3×10^{12} cm^{-2} for the rough domain, respectively.

3.3.4 In-plane and out-of-plane XRD analysis

In Figure 3.6, the out-of-plane XRD measurement (ω–2θ scan) of the flat domain was performed to obtain d(0 0 1) value (2θ = 3.96°, d = 14.33 Å). The solution-processed pentacene thin films were found to include only bulk phase. In the case of vacuum-deposited pentacene thin films on SiO_2, at least two phases, bulk phase (d = 14.4 Å) and thin-film phase (d = 15.4 Å), have been reported commonly [11–13]. So far, at least five different polymorphs of pentacene single crystal were identified to the best of our knowledge [14–17]. Furthermore, Mattheus *et al*. has proposed that four different polymorphs of d(0 0 1) = 14.1, 14.4, 15.0 and 15.4 Å exist in pentacene single crystal and thin film [17,18]. The bulk phase in the vacuum-deposited films is believed in general to form the crystal structure similar to that reported by Campbell *et al*. [14]. Polymorphism and growth mechanism in vacuum-deposited pentacene thin films have also been studied by other groups [19–23].

In the preliminary measurement for out-of plane using a Cu-target (λ = 1.54 Å), the full width at half maximum (FWHM) of XRD patterns for the solution-processed thin films showed 0.08° for (0 0 1) plane, which was smaller values than that of the vacuum-deposited films (0.20°); however, these measured structures were related with the out-of-plane structure to the substrate. With respect to the carrier mobility, in-plane crystallinity is critically important for TFTs. Thus, we investigated in-plane crystallinity of thin films by GIXD measurement using synchrotron radiation in SPring-8. In this section, since the control of the π-π stacking structure at the substrate surface is critical issue, we focus on analyzing the GIXD results to determine the two-dimensional molecular assembling at the substrate.

The in-plane XRD patterns (ϕ–$2\theta_\chi$ scan) for the flat and rough domains of solution-processed thin film are shown in Figure 3.7. A remarkably strong peak at

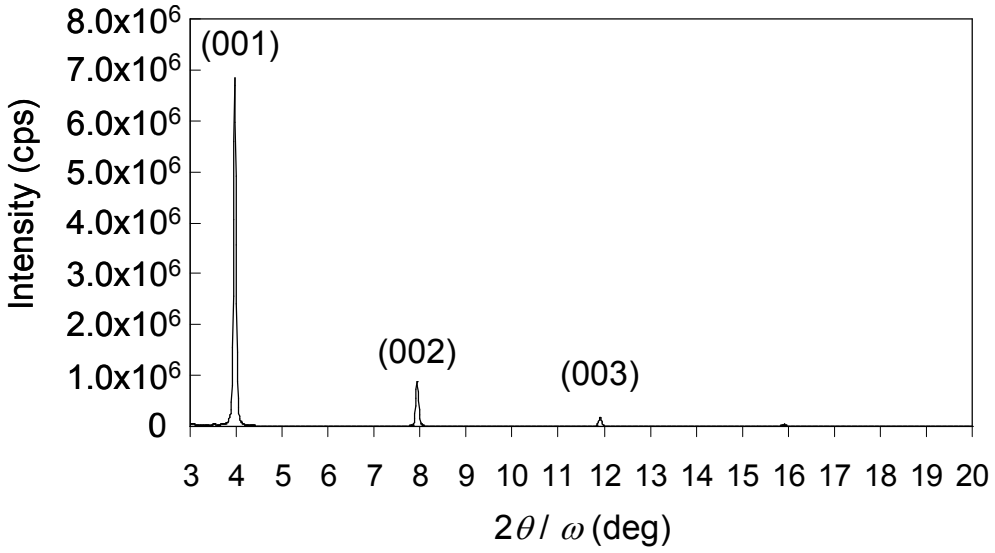

Figure 3.6: Out-of-plane diffraction pattern of solution-processed pentacene film. The 2θ angle is that of $\lambda = 0.99$Å.

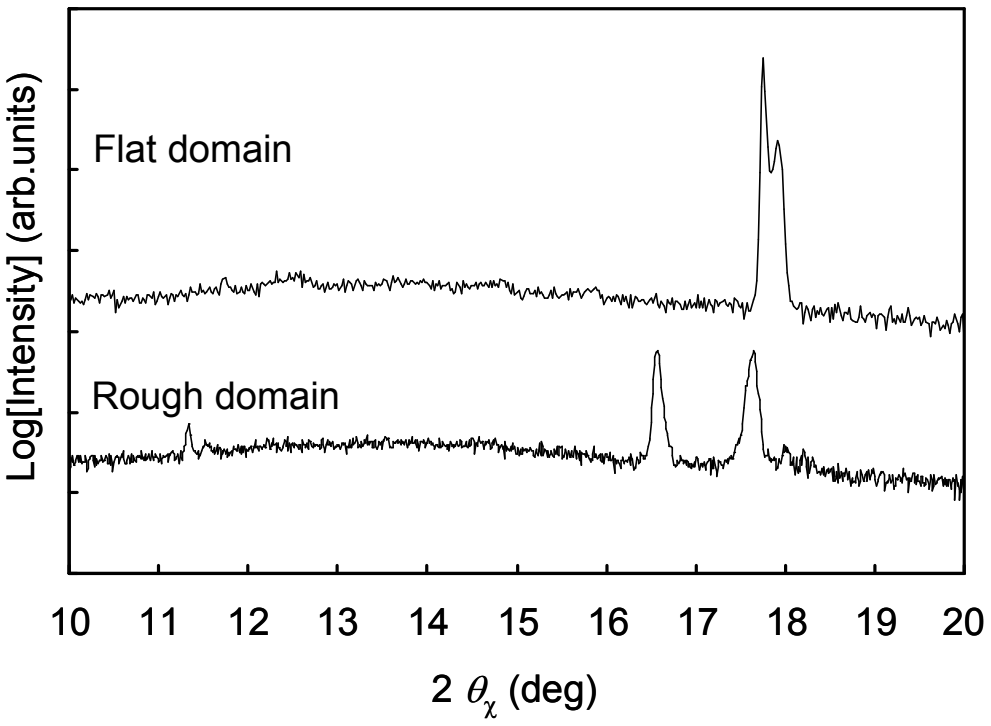

Figure 3.7: In-plane diffraction patterns of flat and rough domains. Note that the scale of intensity for flat domain is 20 times larger than rough domain. $2\theta_\chi$ angle is that of λ = 0.99Å.

17.76° was observed for the flat domain, with intensity almost 20 times higher than that of the peak at 17.65° for the rough domain. Since the rough domain in the thin films has a dendritic crystal shape, the observed peaks resemble those of a polycrystalline bulk structure, which has $2\theta_\chi$ values are 11.34°, 16.57°, and 17.65°. The crystallite size, *D*, of thin films was estimated using Scherrer's equation:

$$D = \frac{K\lambda}{\beta \cos\theta}, \tag{3-2}$$

where λ, β and θ are the wavelength of X-ray, FWHM and Bragg angle for sampled peak, respectively. A Scherrer constant, *K*, of 0.9 was employed, and the Bragg angles, $2\theta_\chi$, of sampled peak were 17.76° for the flat domain and 17.65° for the rough domain, respectively. In addition, the resolution of this measurement of $2\theta_\chi$ was 0.016°. With equation (3-2), the crystallite sizes were estimated at 150 nm for the flat domain and 50 nm for the rough domain from each FWHM (0.034° for the flat domain and 0.10° for the rough domain). As a result, the solution-processed pentacene TFTs with the flat domain exhibited the high carrier mobility, owing to the two-dimensional high crystallinity.

3.3.5 Two dimensional mapping of GIXD pattern

The sample was also rotated (ϕ axis) for every in-plane scanning to obtain the 2D-mapping of the GIXD patterns for the flat domains of solution-processed thin films. The mapping measurement is convenient to confirm preferred azimuthal crystal growth quickly. The 2D-mapping of the GIXD patterns for the flat domain was performed by rotating of sample stage with angle ϕ ranging from −45° to 45° as shown in Figure 3.8(a). For simplicity, the obtained peaks are truncated by the intensity of 10^3 cps. Several strong peaks of 10^4–10^5 cps at $2\theta_\chi$ = 17.7–18.1°, the middle peaks of ca. 10^4 cps at 16.4–16.6° and week peaks of less than 10^4 cps at 14.6°, 12.4° and 11.3° were obtained within this 90° range of sample rotation.

Figure 3.8(b) represents the GIXD patterns obtained from the summation of

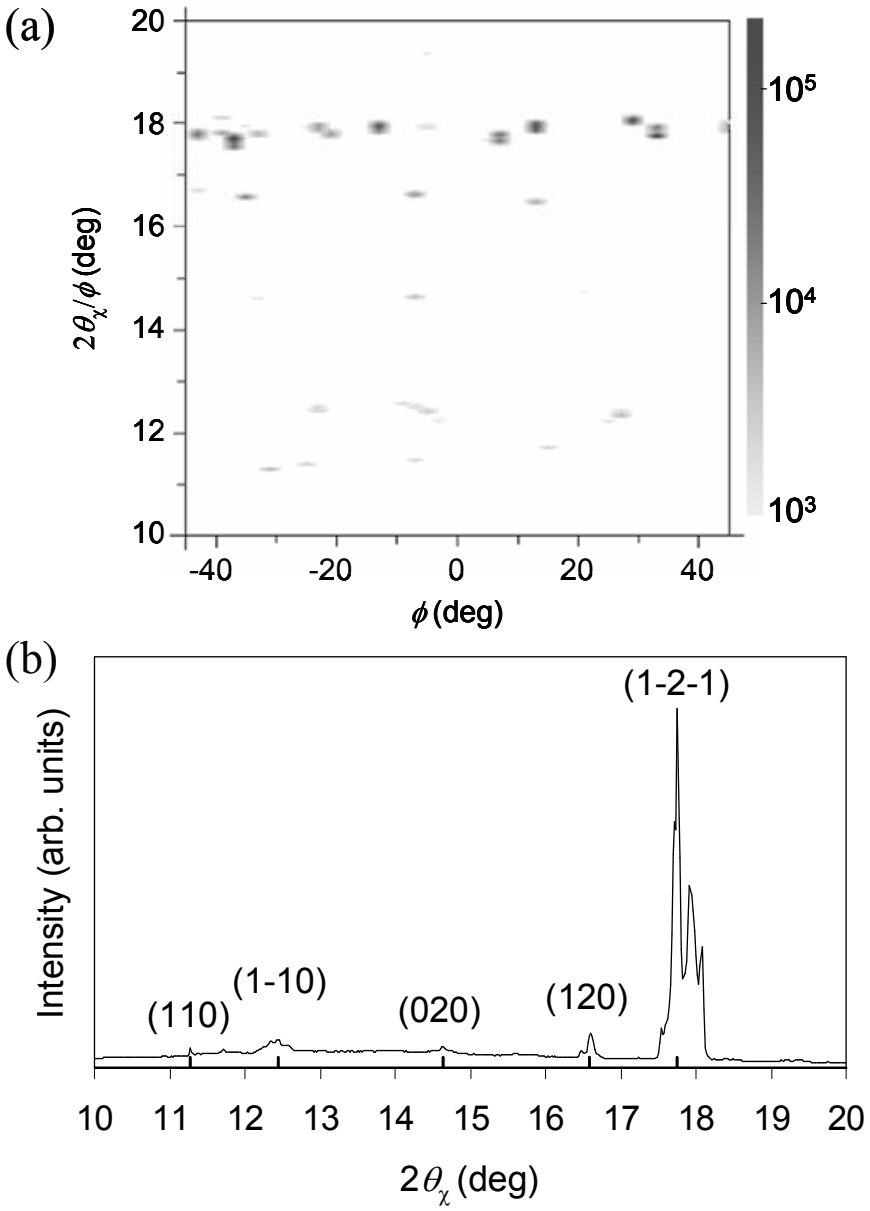

Figure 3.8: (a) In-plane two-dimensional mapping of GIXD patterns of the flat domain. Peaks were truncated by the intensity of 10^3 cps. (b) GIXD pattern obtained from summation of intensity over all ϕ scans. ϕ is the rotation angle of sample. $2\theta_\chi$ angle is that of $\lambda = 0.99$Å.

intensity over all the ϕ scans in the 2D-mapping. In principle, only the lattice planes perpendicular to the film surface should be detected; however, diffraction peaks assigned to lattice planes close to the exact diffraction condition were observed as well. These diffractions were assigned by employing the structure reported by Campbell *et al*. [14]. Campbell's structure was redefined as a = 6.06, b = 7.90, c = 14.88 Å, α = 83.26°, β = 100.54°, and γ = 85.80°, since the original structure was not reduced cell. By comparison with a simulated XRD pattern, based on the reduced Campbell's structure, the characteristic peaks at $2\theta_\chi$ = 17.76°, 16.58°, 14.64°, 12.44°, and 11.28° in Figure 3.8(b) were assigned to (1 −2 −1), (1 2 0), (0 2 0), (1 −1 0) and (1 1 0), respectively. However, there is the deviation within 0.5°–1.0° in $2\theta_\chi$ values for the respective diffraction peaks, especially in the peaks around $2\theta_\chi$ = 17.7–18.1°. We have not yet conclusively elucidated the source of this deviation.

Focusing on the strongest peaks around $2\theta_\chi$ = 17.7–17.8°, only four peaks with intensity above 10^4 cps are confirmed at ϕ = 33°, 7°, −37° and −43°. These preliminary results imply that the azimuthal development is considerably limited within the plane. A single flat domain of solution-processed pentacene film tends to have stripe patterns in a single direction. We consider that stripe direction is related to the growth direction of each flat domain and that the several diffractions around 17.7° for the rotated samples reflect the number of the flat domains included in the area irradiated by the X-ray beam. We will discuss the growth azimuth in Chapter 5.

3.3.6 Estimation of lattice parameters

The pentacene single crystal had a triclinic lattice ($P\bar{1}$), and the lattice spacing of the (h k l) plane, $d(h\ k\ l)$, for triclinic structure is represented as follows,

$$\begin{aligned}\frac{1}{d(h\ k\ l)^2} = \frac{1}{V^2}\Big[&(b^2c^2\sin^2\alpha)\ h^2 + (a^2c^2\sin^2\beta)\ k^2 + (a^2b^2\sin^2\gamma)\ l^2 \\ &+ 2abc^2(\cos\alpha\cos\beta - \cos\gamma)\ hk \\ &+ 2a^2bc(\cos\beta\cos\gamma - \cos\alpha)\ kl \\ &+ 2ab^2c(\cos\gamma\cos\alpha - \cos\beta)\ lh\Big]\end{aligned} \tag{3-3}$$

where V is the unit cell volume. Once several diffraction peaks are assigned to corresponding (h k l) indices, the lattice parameters can be determined by calculating d(h k l) values to satisfy equation (3-3). In the previous section, we determined (h k l) indices with respect to diffractions at $2\theta_\chi$ = 17.76°, 16.58°, 14.64°, 12.44°, and 11.28° on the basis of a refinement of the crystal structure reported by Campbell. To determine precise $2\theta_\chi$ values, we selected the respective diffractions from the GIXD pattern summed over the ϕ axis scan in the 2D-mapping. A d(0 0 1) value of the same film was obtained in section 3.3.4 (2θ = 3.96°, d = 14.33 Å). Fitting calculations were also carried out, using the reduced Campbell's structure as a structure starting point, to find d(h k l) values within 0.01 %. Estimated lattice parameters of solution-processed thin film are listed in Table 3.1, in comparison with the single crystal structures reported by Campbell and Mattheus. The lattice parameters obtained in this chapter seem to exhibit an intermediate structure between those of Campbell and Mattheus. Mattheus *et al*. discussed the detailed crystal structures for the vapor- and solution-grown single crystals as well as for the bulk phase in thin films grown by vacuum sublimation on SiO_2 [17,18]. They have reported that a crystal grown in a trichlorobenzene solvent had a similar structure to that of vapor-grown crystal with d(0 0 1) = 14.1 Å and that the bulk phase of vacuum-sublimed thin films obtained by powder X-ray diffraction (PXRD) was d(0 0 1) = 14.37 Å. Although d(0 0 1) value for the bulk phase in the sublimed thin film is close to the present result, the other values of d(h k l) differs considerably. In the case of Mattheus's single crystal, d(1 1 0) and d(1 −1 0) values are in accordance with those found in this chapter; however, the deviation in d-values becomes significant at wider angle of $2\theta_\chi$.

Comparing d(h k l) values, we notice that the lattice parameters α, β, and γ for Mattheus's single crystal are different from Campbell's. In Figure 3.9, the upper and lower molecular layers in the unit cell of pentacene are projected onto the b-c and a-b plane, with respect to Campbell's and Mattheus's structures. We note that the a-b projection, with the origin and b-axis of unit cell overlapping in the lower layer, differs considerably. The corresponding positions of pentacene molecules in the lower layer

Table 3.1: Lattice parameters of solution-processed pentacene thin film for comparison with the other crystal data.

Author	This work	Ref. 14 (single crystal)		Ref. 18	
	(thin film)	original	reduced	(single crystal)	(thin film)
Growth	Solution	Solution		Vapor	
Unit cell parameters (Å and degrees)					
A	6.21	7.90	6.06	6.266	6.485
B	7.87	6.06	7.90	7.775	7.407
C	14.72	16.01	14.88	14.53	14.745
α	83.06	101.9	83.26	76.475	77.25
β	100.70	112.6	100.54	87.682	85.72
γ	85.68	85.8	85.80	84.684	80.92
d-spacing of selected planes (Å)					
d(0 0 1)	14.33	–	14.50	14.12	14.37
d(1 1 0)	5.04	–	4.96	5.02	5.15
d(1 −1 0)	4.57	–	4.52	4.61	4.46
d(0 2 0)	3.89	–	3.90	3.77	3.57
d(1 2 0)	3.43	–	3.42	3.35	3.33
d(1 −2 −1)	3.21	–	3.19	3.16	2.97
Volume ($Å^3$)	698.78	–	692.38	685.16	681.56

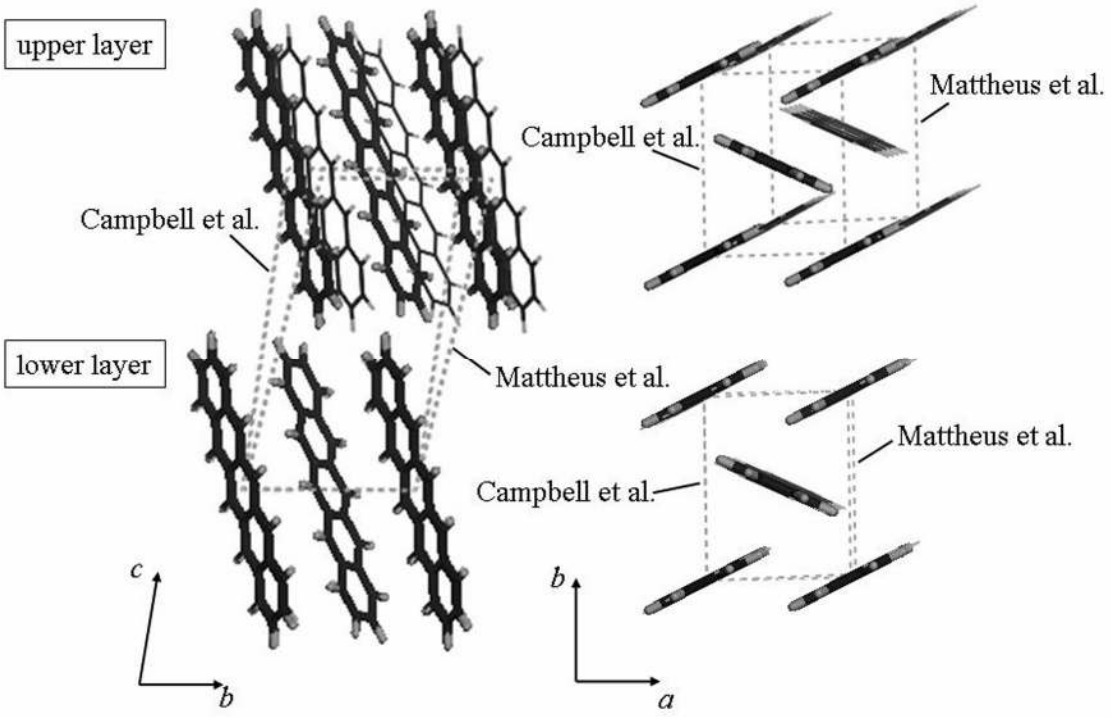

Figure 3.9: Comparison of pentacene molecular layers in the unit cell with respect to crystal structures reported by Mattheus and Campbell. Pentacene molecules drawn with thin line represent the Mattheus's structure and those drown with thick line correspond to the Campbell's.

are similar in both structures, while those in the upper layer are translated by about 3.2 Å within the *a*-*b* plane direction. The differences between these crystal structures arise from the different stacking of the molecular layers in the (0 0 1) direction. In addition, even in the bulk phase of vacuum-deposited pentacene thin films, lattice parameters similar to those of Campbell's structure were reported based on GIXD [21] and PXRD [22] measurements. These reports demonstrate that the crystal structures with identical *d*(0 0 1) do not necessarily have the same lattice parameters.

In contrast, the unit cell determined in this chapter is compared with the Campbell's structure in Figure 3.10. The molecular positions in the upper and lower layers can be regarded as similar despite a 0.4-Å translation of pentacene molecules in the upper layer. Hence, it can be concluded that our solution-processed pentacene thin films have a crystal structure close to the Campbell's structure, with *d*(0 0 1) = 14.33 Å. Moreover, we believe that this difference in crystal structure between Mattheus's and ours arises from the differences in condition of crystal formation. In the Mattheus's study [17], pentacene crystals were grown from trichlorobenzene by slowly evaporating the solvent over 4 weeks at 177 °C under a stream of ultra-pure N_2 gas. In this chapter, the pentacene thin film was prepared in a solution at 200 °C by rapid evaporation of solvent under N_2 atmosphere. Therefore, the relationship between the fabrication process and crystal structure in pentacene is so complicated that careful verification are required, in order to control the structure and electronic properties.

The field effect transistors of pentacene single crystal was reported to show the highest mobility of ~2.3 cm^2/Vs, though the crystal structure of the pentacene crystal has not presented in the literature [24]. Taking into consideration that both single crystal and vacuum-deposited thin film of pentacene can exhibit high carrier mobility comparably, we expect that our solution-processed pentacene TFTs also have an enough potential to show higher mobility than the present one, since our solution-processed pentacene thin films consist of the very large flat domains up to several hundred micrometers including large single-crystal-like crystallites therein. Moreover, it is not practical to fabricate transistors from single crystals since it is difficult to handle single

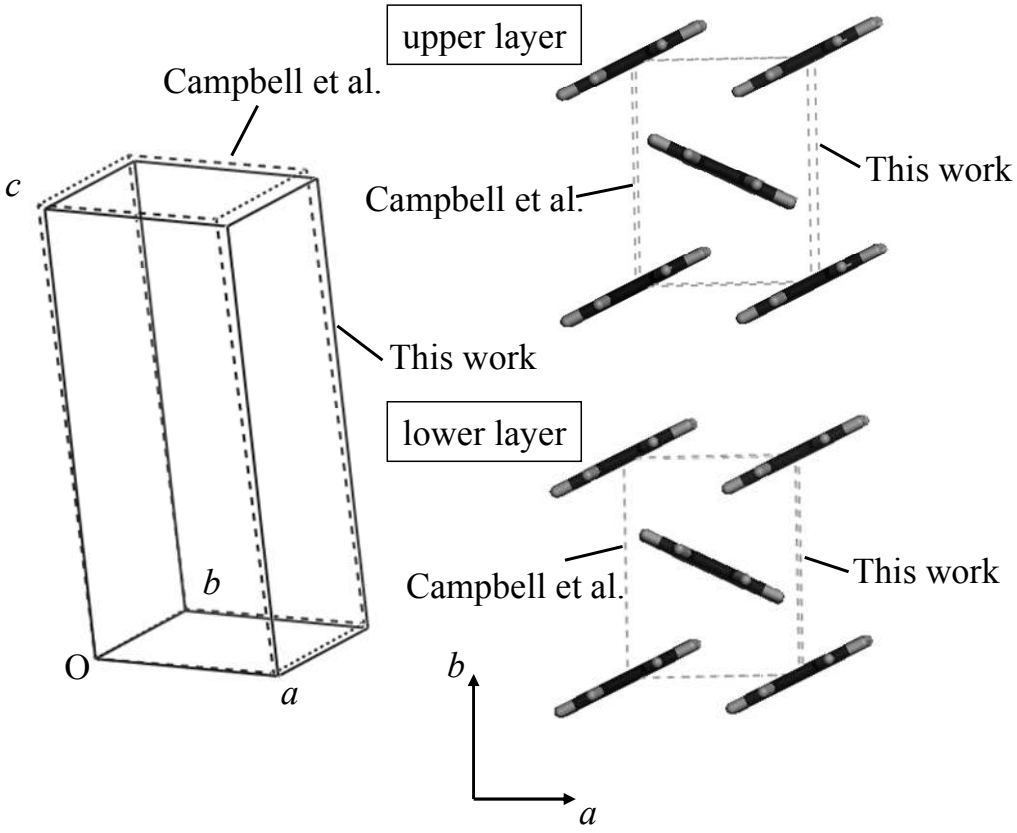

Figure 3.10: Comparison of unit cells for the reduced Campbell's and our crystal structures. The *a*-*b* projections of molecular arrangements are also displayed with respect to the lower and upper layers in the unit cell of pentacene crystal.

crystals due to their fragility and variation in size and shape. Solution-processed pentacene films are good candidates for high-performance transistors owing to their relatively simple processing.

3.4 Conclusion

Pentacene was found to be soluble in TCB under inert atmosphere, and we fabricated pentacene thin film transistors by a direct solution process. The surface morphology of the solution-processed pentacene thin film can be divided into two types: the flat and rough domains. The flat domain had a tendency to form a large plate up to several hundred micrometers. These different morphologies are presumed to arise from a transition in the growth mechanism over the course of film formation. In-plane XRD and AFM analysis revealed that the flat domain exhibited two-dimensional uniformity and included larger crystallites than the rough domain that contained small grains and particles with discontinuity. The characteristics of TFTs consisting of both flat and rough domains were measured. The flat domain was found to show higher carrier mobility and the narrower subthreshold region of transfer characteristic than the rough domain. We also investigated a two-dimensional mapping of GIXD patterns and estimated the lattice parameters of solution-processed pentacene thin film on the basis of a reduced Campbell's structure. This suggested that the solution-processed pentacene film had a crystal structure with $d(0\ 0\ 1) = 14.33$ Å, which is similar to Campbell's structure.

Finally, we emphasize that our solution-processed pentacene TFTs have the potential to show high mobility, since the solution-processed pentacene thin films consist of very large flat domains including large single-crystal-like crystallites.

References

1) M. M. Payne, S. A. Odom, S. R. Parkin, J. E. Anthony, *Org. Lett.* **6**, 3325 (2004).

2) H. Meng, J. Zheng, A. J. Lovinger, B.-C. Wang, P. Gregory, V. Patten, Z. Bao, *Chem. Mater.* **5**, 1778 (2003).

3) M. Mas-Torrent, P. Hadley, S. Bromley, X. Ribas, J. Tarres, M. Mas, E. Molins, J. Veciana, C. Rovira, *J. Am. Chem. Soc.* **126**, 8546 (2004).

4) K. Takimiya, H. Ebata, K. Sakamoto, T. Izawa, T. Otsubo, Y. Kunugi, *J. Am. Chem. Soc.* **128**, 12604 (2006).

5) F. Valiyev, W.-S. Hu, H.-Y. Chen, M.-Y. Kuo, I. Chao, Y.-T. Tao, *Chem. Mater.* **19**, 3018 (2007).

6) P. T. Herwig, K. Mullen, *Adv. Mater.* **11**, 480 (1999).

7) A. Afzali, C. D. Dimitrakopoulos, T. L. Breen, *J. Am. Chem. Soc.* **124**, 8812 (2002).

8) S. K. Park, T. N. Jackson, J. E. Anthony, D. A. Mourey, *Appl. Phys. Lett.* **91**, 063514 (2007).

9) S. Matsuno, M. Kuba, T. Nayuki, S. Soga, P. W. T. Yuen, *Rigaku J.* **17**, 36 (2000).

10) K. P. Pernstich, S. Haas, D. Oberhoff, C. Goldmann, D. J. Gundlach, B. Batlogg, A. N. Rashid, G. Schitter, *J. Appl. Phys.* **96**, 6431 (2004).

11) C. D. Dimitrakopoulos, P. R. L. Malenfant, *Adv. Mater.* **14**, 99 (2002).

12) I. P. M. Bouchoms, W. A. Schoonveld, J. Vrijmoeth, T. M. Klapwijk, *Synth. Met.* **104**, 175 (1999).

13) C. D. Dimitrakopoulos, A. R. Brown, A. Pomp, *J. Appl. Phys.* **80**, 2501 (1996).

14) R. B. Campbell, J. M. Robertson, J. Trotter, *Acta Crystallogr.* **15**, 289 (1962).

15) D. Holmes, S. Kumaraswamy, A. J. Matzger, K. P. C. Vollhardt, *Chem.-Eur. J.* **5**, 3399 (1999).

16) T. Siegrist, C. Kloc, J. H. Schön, B. Batlogg, R. C. Haddon, S. Berg, G.. A. Thomas, *Angew. Chem. Int. Ed.* **40**, 1732 (2001).

17) C. C. Mattheus, A. B. Dros, J. Baas, A. Meetsma, J. L. de Boer, T. T. M. Palstra, *Acta Crystallogr. C* **57**, 939 (2001).

18) C. C. Mattheus, A. B. Dros, J. Baas, G. T. Oostergentel, A. Meetsma, J. L. de Boer, T. T. M. Palstra, *Synth. Met.* **138**, 475 (2003).

19) S. E. Fritz, S. M. Martin, C. D. Frisbie, M. D. Ward, M. F. Toney, *J. Am. Chem. Soc.* **126**, 4084 (2004).

20) S. D. Wang, X. Dong, C. S. Lee, S. T. Lee, *J. Phys. Chem. B* **109**, 9892 (2005).

21) H. Yoshida, N. Sato, *Appl. Phys. Lett.* **89**, 101919 (2006).

22) L. Farina, A. Brillante, R. G. Della Valle, E. Venuti, M. Amboage, K. Syassen, *Chem. Phys. Lett.* **375**, 490 (2003).

23) T. Kakudate, N. Yoshimoto, *Appl. Phys. Lett.* **90**, 081903 (2007).

24) J. Y. Lee, S. Roth, Y. W. Park, *Appl. Phys. Lett.* **88**, 252106 (2006).

Chapter 4

Air stability of solution-processed pentacene thin film transistors

4.1 Introduction

Solution-processed organic thin film transistors (TFTs) have been made mainly from polymer semiconductors, for example, poly(3-hexyl-thiophene) [1] and polyfluorene [2]. In contrast to its high processibility, oxygen-induced unintentional carrier doping [3] and relatively high contact resistance [4–7] have been important issues in the polymer TFTs. In the previous chapter, we presented a novel solution process using pentacene without any precursors and derivatives ever reported [8–10]. The solution-processed pentacene thin film showed higher crystallinity than the vacuum-deposited one, and its TFT exhibited a high carrier mobility of more than 0.1 cm^2/Vs. The crystallinity and surface morphology of thin films are known to influence on the transistor performances directly. Therefore, a combination between organic semiconductors and related materials such as electrodes and gate insulators is important to control the TFT performances [11–13]. To interpret the electrical behavior, the transistor properties have been derived theoretically from the physical parameters of the films; carrier density, trap states, and impurities [14–16].

In this chapter, the trap states of the solution-processed pentacene TFTs are evaluated in comparison with the vacuum-deposited pentacene TFTs, using simple analytical models presented in Ref. 14. Then, we will show that solution-processed TFTs are accompanied by the advantage of stability of the TFT performances during the storage in air and dark conditions, compared with the vacuum-deposited TFTs.

4.2 Experimental procedure

The solution-processed pentacene films were prepared as described in section 3.2. Vacuum-deposited films were grown on the same substrate under pressure in the order of 10^{-6} Pa with the deposition rate of 0.6 Å/s. The temperature of substrate was kept at 25 °C throughout the deposition. Heavily doped silicon wafers with a 200-nm-thick silicon dioxide insulator were used as a substrate. Au source and drain electrodes of bottom-contact configuration were prepared as presented in section 2.2.1. The substrates were cleaned with oxygen plasma prior to all preparations of the thin films. The specific surface treatment such as a self-assembled monolayer was not utilized for TFT preparations.

The electrical properties of OTFTs were measured with a semiconductor parameter analyzer (Keithley 4200SC) under reduced pressure of 10^{-4} Pa. The field effect mobility μ was calculated from the slope of the linear part of an $I_{d,sat}^{1/2}$ vs. V_g plot in the saturation region, using equation (2-1). Threshold voltage V_{th} was estimated from the intercept of a line drawn through the linear part of the $I_{d,sat}^{1/2}$ vs. V_g plot.

The surface morphology was observed by atomic force microscopy (AFM; Nano scope IIIa, Digital Instruments). All observations were performed using tapping mode of AFM with NCH-10T probe.

Time-of-flight secondary ion mass spectroscopy (TOF-SIMS; TRIFT III, Physical Electric) was used to investigate the degradation of pentacene on the thin-film surface. In the TOF-SIMS analysis, Ga^+ ion beam was radiated to the sample surface as a primary ion to emit molecules (with some fragment ions) as a secondary ion. The mass of secondary ions can be determined by the difference in the flight time of the molecular ions. This method can characterize the outermost surface layers to several nanometers.

4.3 Analytical model

We present brief introduction of backgrounds in the analytical model presented by Horowitz and Delannoy [14]. This model is based on a single shallow trap level

near the conduction band minimum for *n*-type semiconductors as shown in Figure 4.1 (valence band maximum for *p*-type semiconductor). All the following equations were proposed for *n*-type semiconductors in the literature.

In the gradual channel approximation, the source–drain current, I_d is given by

$$I_d = \frac{W}{L}\int_0^{V_d} \left|Q_{s,f}\right| \mu_0 dV_y , \tag{4-1}$$

where $Q_{s,f}$ is the free surface charge and μ_0 is the intrinsic mobility that is independent from the gate voltage. The total surface charge per unit area, Q_{tot}, is induced by local gate voltage, $V_{g,y} = V_g - V_y$ at the position y of the interface, and is written as

$$Q_{tot} = -C_{ox}\left(V_{g,y} - V_{FB}\right) = Q_{s,f} + Q_{s,t} , \tag{4-2}$$

where C_{ox} is the capacitance of insulator per unit area and V_{FB} is the flat band potential. In this model, the flat band potential is considered to be much smaller than V_g, and is accordingly neglected. Q_{tot} can be divided into two terms, which are the free surface charge density $Q_{s,f}$, and the trapped surface density $Q_{s,t}$, respectively. The charge density can be replaced as follows,

$$Q_{tot} = \int_0^{V_S} \frac{\rho_f + \rho_t}{F_x(V)} dV = -C_{ox}\int_0^{V_g} \frac{\rho_f + \rho_t}{\rho_{tot}} dV_{g,x} , \tag{4-3}$$

where ρ is the volume charge density with subscription f and t representing free- and trapped charge, respectively. V_S denotes the potential at the semiconductor surface. $V_{g,x}$ value of the gate voltage can be defined from Gauss's law,

$$Q_{tot} = -\varepsilon_S F_x , \tag{4-4}$$

and equation (4-2) as

$$V_{g,x} = \frac{\varepsilon_S F_x}{C_{ox}} . \tag{4-2'}$$

At the semiconductor surface, $V_{g,x}$ is equal to V_g. $F_x(V)$, which denotes the electric field along the x direction in the channel ($F_x = -dV/dx$), is related to the total

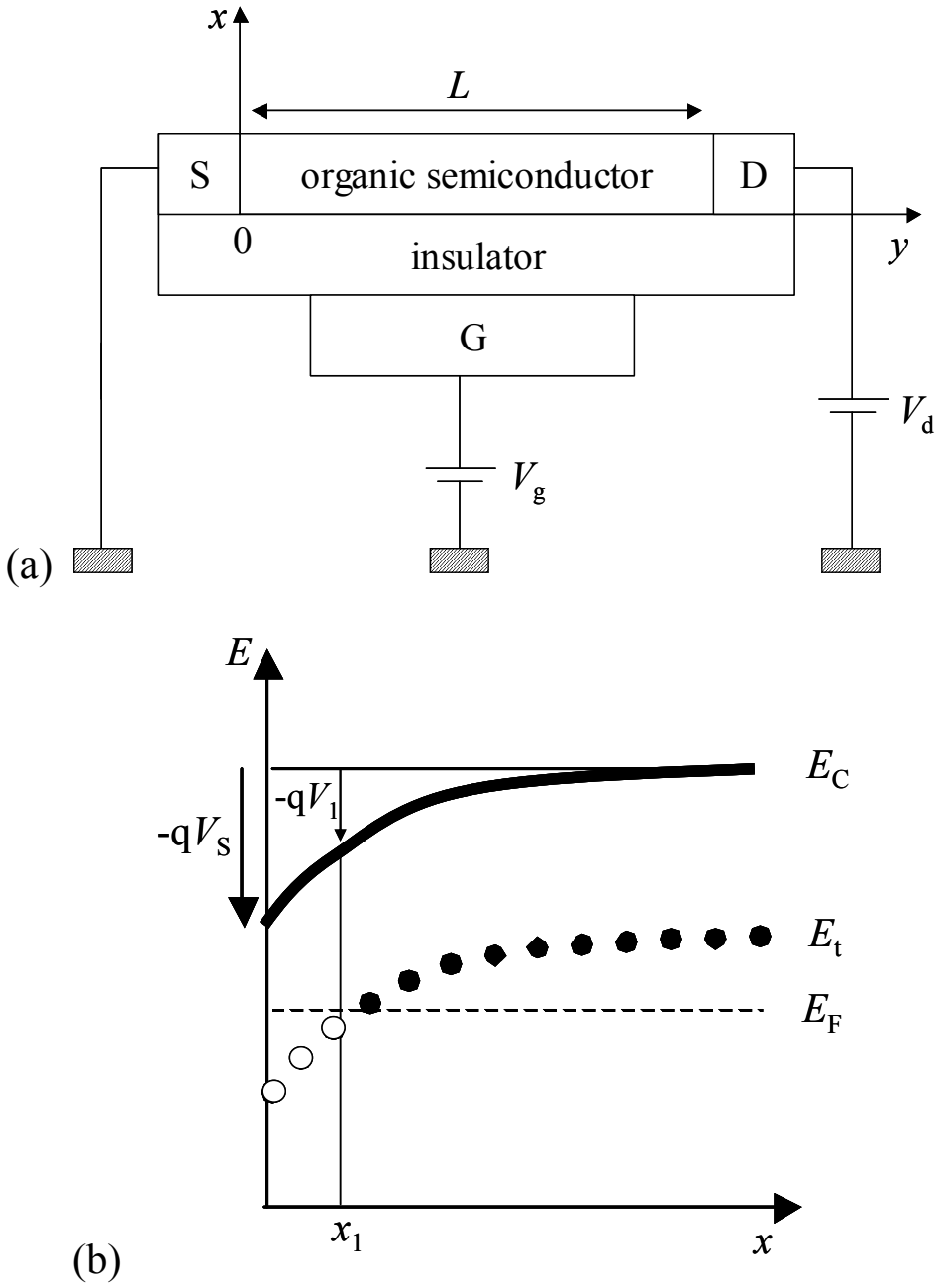

Figure 4.1: Schematic illustration of the organic thin-film transistors, (a) geometry of transistor and (b) energy diagram of an accumulation layer for *n*-type semiconductor with a single trap level of energy E_t. qV_S is the band bending at the surface.

space-charge density ρ_{tot} by Poisson's equation ($dF_x/dx = \rho_{tot}/\varepsilon_S$). Using these two relations, F_x can be integrated to give

$$F_x^{\,2} = -\frac{2}{\varepsilon_S}\int_0^V \rho_{tot}\, dV', \tag{4-5}$$

where ε_S is the dielectric constant of semiconductor.

Here it is assumed that the single trap state of density N_t at energy level E_t below the conduction band minimum E_C as shown in Figure 4.1(b). The volume density of free- and trapped charge carriers, n_f and n_t, are expressed as

$$n_f = \frac{N_C}{1+\exp\left[\left(E_C - E_F - qV\right)/kT\right]}, \tag{4-6}$$

$$n_t = \frac{N_t}{1+\exp\left[\left(E_t - E_F - qV\right)/kT\right]}. \tag{4-7}$$

In n-type semiconductors, $\rho = -qn$ with $V > 0$, while $\rho = qn$ with $V < 0$ in p-type semiconductors. In addition, the conduction band was also assumed to behave like a single state at the conduction band edge. On the basis of these assumptions, the following equation can be derived from equation (4-5) as

$$F_x^{\,2} = \frac{2kT}{\varepsilon_S}\left[N_C\left(\frac{qV}{kT} + \ln\frac{1+\exp\left[\left(E_C - E_F - qV\right)/kT\right]}{1+\exp\left[\left(E_C - E_F\right)/kT\right]}\right) + N_t\left(\frac{qV}{kT} + \ln\frac{1+\exp\left[\left(E_t - E_F - qV\right)/kT\right]}{1+\exp\left[\left(E_t - E_F\right)/kT\right]}\right)\right]. \tag{4-8}$$

The total charge Q_{tot} is obtained from equations (4-4) and (4-8), and the free- and trapped surface charge is derived from equation (4-3), into which equations (4-6), (4-7) and (4-8) are introduced, by means of a numerical integrating of the resulting equation. Furthermore, the gate voltage is deduced from Q_{tot} through equation (4-2). The important parameter should be defined as

$$\theta_s = Q_{s,f}/Q_{tot}\,, \tag{4-9}$$

where θ_s is the ratio of free to total induced carrier.

The drain current of TFTs was calculated using equations (4-1) and (4-3) within the gradual channel approximation.

$$I_d = \frac{W}{L}\mu_0 \int_{V_g - V_d}^{V_g} \left| Q_{s,f}\left(V_{g,y}\right) \right| dV_{g,y} \ , \quad V_d < V_g , \tag{4-10a}$$

$$I_{d,sat} = \frac{W}{L}\mu_0 \int_{0}^{V_g} \left| Q_{s,f}\left(V_{g,y}\right) \right| dV_{g,y} \ , \quad V_d \geq V_g . \tag{4-10b}$$

Free- and trapped carrier densities calculated based on equations (4-6) and (4-7) are exhibited in Figure 4.2. The physical parameters in the Figure are arbitrary chosen for the demonstration. In this model, the band bending range was divided into three regions. In the first region, to calculate drain current I_d, the free- and trapped carrier distributions of equations (4-6) and (4-7) are approximated by the Boltzmann distribution,

$$n_f = N_C \exp\left(-\frac{E_C - E_F - qV}{kT} \right) = n_{f0} \exp\frac{qV}{kT} , \tag{4-6'}$$

$$n_t = N_t \exp\left(-\frac{E_t - E_F - qV}{kT} \right) = n_{t0} \exp\frac{qV}{kT} . \tag{4-7'}$$

Here, n_{f0} and n_{t0} are the bulk free- and trapped carrier density, respectively. Using equations (4-6') and (4-7'), equation (4-9) can lead to

$$\theta_s = n_{f0} / \left(n_{f0} + n_{t0} \right) \equiv \theta_0 . \tag{4-11}$$

In the first region where the surface potential V varies from 0 to V_1, the drain current obtained from equation (4-10b) gives

$$I_{d,sat} = \frac{W}{2L} C_{ox} \theta_0 \mu_0 V_g^{\ 2} . \tag{4-12}$$

In this region, the free carrier density can be estimated to be much lower than the trapped carrier density. Hence, θ_0 is approximated to

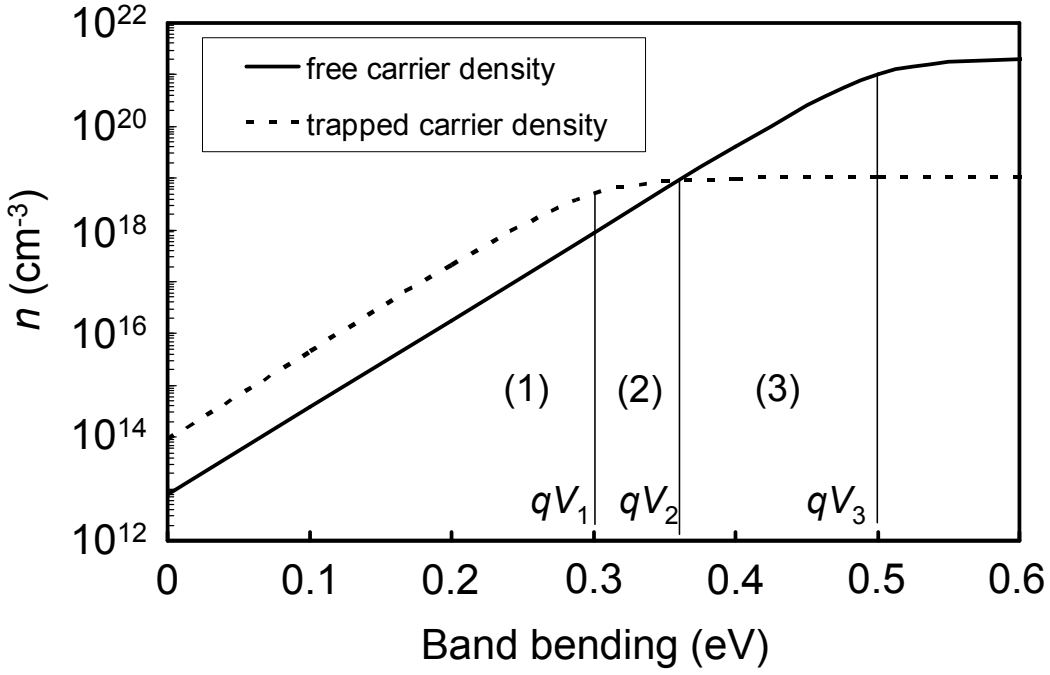

Figure 4.2: Simulation of trapped and free carrier density as a function of band bending energy. In this calculation, $E_C - E_F$ and $E_t - E_F$ were assumed to be 0.5 eV and 0.3 eV, respectively. N_C and N_t were 2×10^{21} cm^{-3} and 1×10^{19} cm^{-3}, respectively.

$$\theta_0 \approx \frac{n_{f0}}{n_{t0}} = \frac{N_C}{N_t}\exp\left(-\frac{E_C - E_t}{kT}\right). \tag{4-13}$$

In the second region, the surface potential takes a value from V_1 to V_2, at which n_f is equal to n_t. This region should correspond to the subthreshold regime in the conventional TFTs. In this region, the saturation current varies exponentially as a function of the gate voltage, and further details are given in Ref. 14.

In the third region, where the surface potential exceeds V_2, the free carrier density exceeds the trapped carrier density. The drain current is calculated using equation (4-10b), and is approximated by the following equation,

$$I_{d,sat} \approx \frac{W}{2L} C_{ox} \mu_0 \left(V_g - V_{g2}\right)^2, \tag{4-14}$$

where

$$V_{g2} = V_g\left(V_2\right) \approx \frac{\sqrt{2kT\varepsilon_S N_t\left(1 - \ln\theta_0\right)}}{C_{ox}}. \tag{4-15}$$

Equation (4-14) corresponds to the equation in the saturation regime of a conventional TFT, and the V_{g2} represents threshold voltage in the accumulation regime of a metal-oxide-semiconductor field-effect transistor. The surface potential of $V = 0$ was set to the position of an onset voltage V_{on}.

4.4 Results and discussion

4.4.1 Trap density in thin films

The trap-state parameters for α-sexithiophene were extracted from the $I_{d,sat}^{1/2}$ vs. V_g plot in Ref. 14. The procedures are applied to the pentacene TFTs in this section, and the method for the extraction of parameters is briefly summarized in the following. For reference, the straight lines are drawn on the transfer characteristics in Figure 4.3.

(i) V_{on} is determined from the I_d in log scale vs. V_g plot. The position of V_{on} is

defined as an origin of gate voltage.

(ii) The linear fit of the $I_{d,sat}^{1/2}$ vs. V_g plot in the initial regime, where the V_g is higher than V_{on} are taken, and the slope of this fitting line (fitting 1 in the figure) gives $\theta_0\mu_0$, based on equation (4-12).

(iii) The linear fit of the $I_{d,sat}^{1/2}$ vs. V_g plot in the saturation regime are drawn. The slope and the intercept of the fitting line (fitting 2 in the figure) correspond to μ_0 and V_{th} in equation (2-1), respectively.

(iv) The ratio of free-to-trapped carrier density, θ_0, is obtained from the ratio of two mobilities shown above. The values for θ_0 and V_{g2} (= $V_{on} - V_{th}$) are substituted into equation (4-15) to calculate the trap density N_t.

(v) The trap level, $E_C - E_t$, is determined from θ_0 and N_t by using equation (4-13).

The values corresponding to N_C (N_V for pentacene), ε_S, and T were presumed to be 2.9×10^{21} cm^{-3} from crystal data determined by Campbell *et al*. [17], $6.7\varepsilon_0$ where ε_0 is the permittivity of vacuum [18], and 300 K, respectively. The density of states in the conduction band N_C was regarded as equal to the density of molecules in the molecular crystal, as is generally assumed for materials with narrow transport band.

Estimated parameters of pentacene TFTs are listed in Table 4.1. Mobility in the saturation regime is almost the same both for the solution-processed (SP) and vacuum-deposited (VD) TFTs. However, the V_{g2} of the VD-TFT is larger than that of the SP-TFT by 20 V as is shown in Figure 4.3. This discrepancy should be attributed to the difference in the trap states, that is, the trap density of the VD-TFT is larger by one to two order(s) of magnitude and the trap level is shallower by 0.1 eV than those of the SP-TFT. These results imply that the trap states for the SP-TFT are filled with hole carriers rapidly with the applied gate bias, and that the hole carrier can be easily injected into the trap states near the Fermi level, in comparison with the VD-TFT. In addition, since the trap states that affect on the TFT characteristics is limited within the interfacial region between the dielectric and semiconductor layers, we also estimated a surface trap density, using equation (3-1) on the assumption that the trapped charge carriers distribute within the first molecular layer at the interface. The surface trap densities

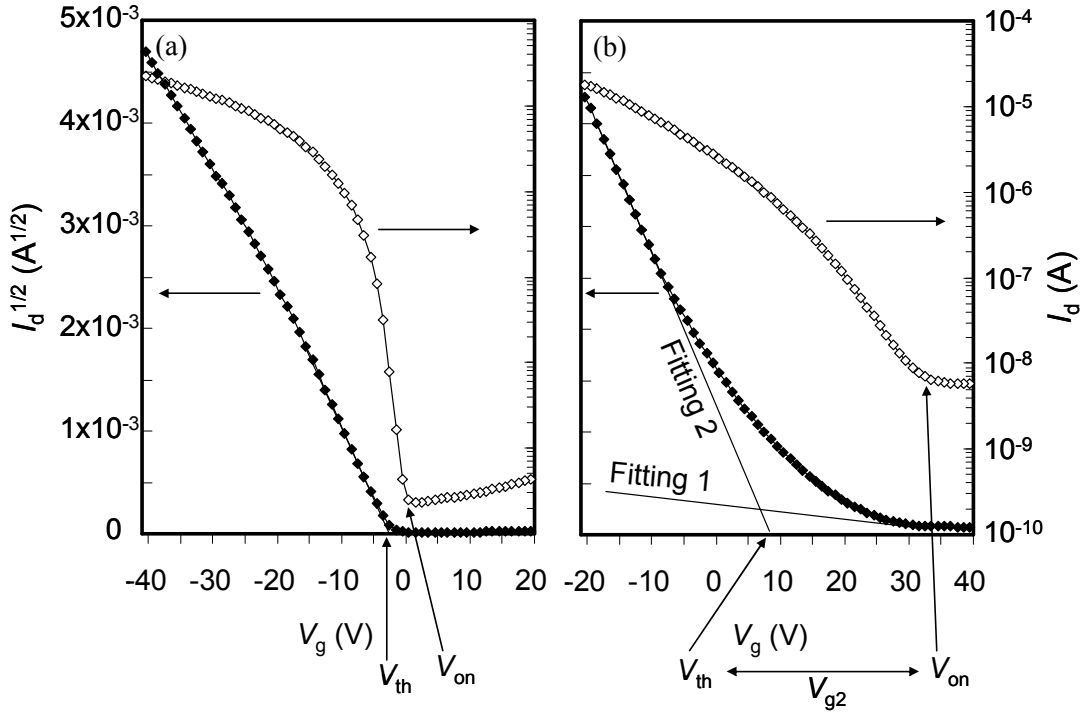

Figure 4.3: Transfer characteristic for (a) a solution-processed pentacene TFT and (b) a vacuum-deposited pentacene TFT. Note that the same V_g ranging from 40 to −60 V and $V_d = -60$V was applied in both measurements.

Table 4.1: Parameters of pentacene TFT fabricated with solution process and vacuum deposition.

Parameter	Unit	Solution process	Vacuum deposition
μ_0	cm^2/Vs	0.25	0.27
$\theta_0\mu_0$	cm^2/Vs	2.9×10^{-4}	7.3×10^{-4}
V_{g2}	V	3.3	25
θ_0	-	1.3×10^{-3}	2.6×10^{-3}
N_t	cm^{-3}	8.4×10^{16}	5.3×10^{18}
E_t-E_V	eV	0.44	0.32

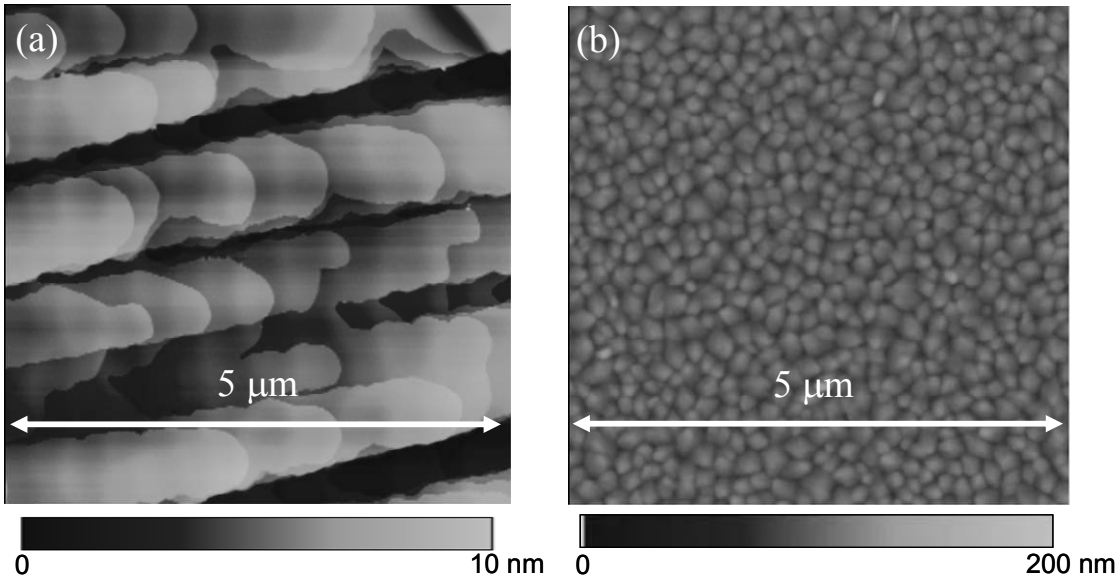

Figure 4.4: AFM height-images of (a) solution-processed and (b) vacuum-deposited films.

for the SP- and VD-TFTs are calculated to be 3.5×10^{11} cm^{-2} and 2.7×10^{12} cm^{-2}, respectively. The difference in the trap states would affect the subthreshold slope to be estimated at 1.6 V/decade for the SP-TFT and 13 V/decade for the VD-TFT.

Here the surface morphologies of both SP and VD films are shown in Figure 4.4. The SP film showed large plate-like domains with molecular steps up to several hundred micrometers in size, while the VD film consists of small grains of less than 200 nm. Therefore, the VD film obviously contains much grain boundaries, where a large amount of trap states should exist owing to the structural defects in the film.

As a result, the SP-TFT exhibited a higher subthreshold characteristic than the VD-TFT. The analytical model reveals that the SP film has lower trap density than the VD film, as is attributed to the morphological difference of the films.

4.4.2 Electrical stability of TFTs

The electrical stability of the SP and VD films was investigated by evaluating the change of the TFT characteristics during storage in air. Typical TFTs that exhibited the mean value of carrier mobility were investigated. Both of the films were stored in a dark environment in air. The transfer characteristics of the SP- and VD-TFTs were pursued for 77 days and 44 days, respectively. The transitions of TFT characteristics are listed in Table 4.2, and the change of the square root of drain current as a function of gate voltage are shown in Figure 4.5 for both TFTs. The carrier mobility of both TFTs has dropped slightly throughout the storage; however, the threshold voltage V_{th} showed large shift of more than 40 V for the VD-TFT, while V_{th} of the SP-TFT shifted in only several volts even for 77 days. The variations in trap state for both TFTs were estimated using the analytical model mentioned in the previous section. The total trap density, N_t of the SP- and VD-TFTs is confirmed to increase by 1.2×10^{17} and 2.7×10^{18} cm^{-3}, respectively, throughout the storage.

Since the structural defects such as grain boundary cannot change during the storage, these increases in the total trap density should be attributed to the change in the amount of chemical impurities. On the other hand, it is known that the V_{th} is related to

Table 4.2: Summarized properties of the solution-processed and vacuum-deposited pentacene TFTs resulting from storage in air and dark condition.

Duration	Solution process		Duration	Vacuum deposition	
[day]	μ [cm^2/Vs]	V_{th} [V]	[day]	μ [cm^2/Vs]	V_{th} [V]
1	0.15	10.9	1	0.21	28.5
14	0.13	9	10	0.2	1.8
77	0.13	7.6	44	0.13	-13.7

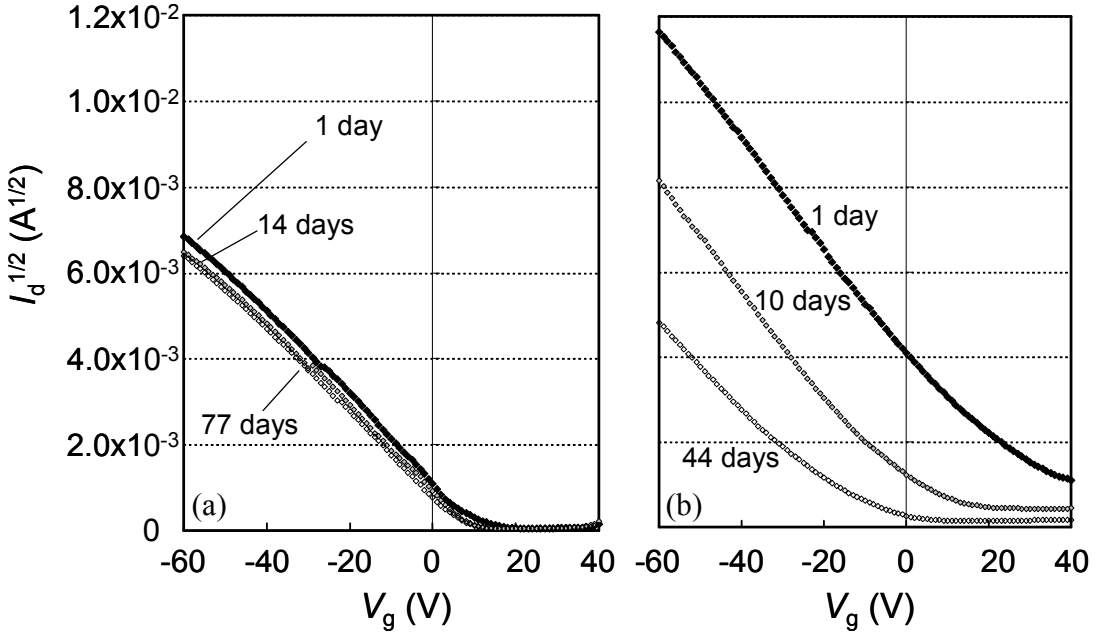

Figure 4.5: Plot of the square root of the drain current as a function of the gate voltage with elapse for (a) solution-processed and (b) vacuum-deposited pentacene TFTs. Applied voltage between source and drain is −60 V. The transistor geometry is *W/L*= 500/50 (μm).

the bulk carrier density and the interfacial dipole [15,19]. Thus, in this case, it can be assumed that this threshold shift is caused by the decrease in the bulk carrier density, ΔN_A rather than the shift of flat band potential. From that assumption, the threshold shift is defined as follow [15],

$$\Delta V_{th} = \frac{q\Delta N_A d_S^{\,2}}{2\varepsilon_S}\left(1+\frac{2\varepsilon_S}{C_{ox}d_S}\right), \tag{4-16}$$

where d_S is the thickness of semiconductor. The thickness of SP thin film was determined to be approximately 200 nm from the cross section of AFM profile, while the 200-nm-thick VD thin film was prepared. Here, taking into consideration that total ΔV_{th} is equal to the sum of shifts in V_{on} and V_{g2}, the net threshold shift should correspond to the shift of V_{on}. The estimated amounts of decrease in the bulk carrier density N_A for the SP- and VD-TFTs were 8.3×10^{15} cm^{-3} and 1.0×10^{17} cm^{-3}, respectively.

To verify the origin of this reduction in the bulk carrier, the same VD-TFT was stored under an inert environment (nitrogen glove box) for 66 days. The TFT characteristics, μ and V_{th}, were changed from 0.15 cm^2/Vs to 0.14 cm^2/Vs and from 29.5 V to 5.7 V, respectively. The threshold shift of the VD-TFT stored under nitrogen was 10 volts smaller than that of the VD-TFT under an air atmosphere, despite the longer storage term. The corresponding changes in N_t and N_A are 1.1×10^{18} cm^{-3} and 7.4×10^{16} cm^{-3}, respectively. Exposure to the atmosphere was inevitable after preparation of thin films and in the TFT characteristic measurements. Hence, this medium value of threshold shift for the VD-TFT stored in nitrogen globe box has arisen from the adsorption of oxygen and moisture in the initial and additional exposure to the atmosphere during several operations. Consequently, the VD-TFT is much more sensitive to the atmosphere than the SP-TFT.

It has been reported that the performances of pentacene TFTs could be affected by atmospheric oxygen and/or moisture [20–24]. The oxygen incorporated in the pentacene film induces the acceptor-like states to shift the onset voltage positively [20].

On the other hand, a first-principles calculation of defect formation energy in the bulk pentacene was carried out, and it was proposed that the electrically active gap states were caused by formation of $C_{22}H_{15}$ (hydropentacene), $C_{22}H_{13}O$ (oxypentacene), and $C_{22}H_{15}O$ (6,13-dihydro-6-hydroxy-pentacene) defects that are likely to become the carrier trapping states [25]. Those impurities were predicted to form the charged defects to give rise to the bias-stress effect, by which the threshold shift will occur. Moreover, it was reported that purification of pentacene by removing $C_{22}H_{12}O_2$ (6,13-pentacenequinone) contributed to reduce the trap density in the pentacene single crystal on the basis of space-charge-limited current measurement [26]. Therefore, pentacene molecules in the film react with oxygen or water in the air to generate oxides mainly at the grain boundary, where a part of the generated pentacenequinone reduces the hole carriers irreversibly to make them electrically inert.

On the contrary, the carrier mobilities of all TFTs have not shown significant drop during the storage. From these results, it seems to be proven that the carrier transport occurs within the first or second molecular layer from the interface between semiconductor and dielectric layer [27]. That is, the oxidation of pentacene is expected to proceed gradually from the thin-film surface into the bulk, and the inmost layer of pentacene thin films have not fully oxidized within a given period of storage. Needless to say, the carrier mobility is expected to decrease by the storage for much longer term even in the case of SP-TFT, and thus some encapsulations over pentacene films will be necessary in practical applications to the devices.

4.4.3 Surface constituents of degraded pentacene thin films

To investigate the impurities of the pentacene thin films, TOF-SIMS analysis was used. The surface mass spectrum of cations for both SP- and VD thin films after three months from fabrication is shown in Figure 4.6. The specific peaks, m/z = 278.054, 294.063, and 309.078, were detected, and those can be assigned to $C_{22}H_{14}^{+}$ (pentacene), $C_{22}H_{14}O^{+}$, $C_{22}H_{13}O_2^{+}$, respectively. The latter two, *mono*- and *di*-oxidized pentacene molecules are supposed to originate from $C_{22}H_{13}O$ and $C_{22}H_{12}O_2$ impurities

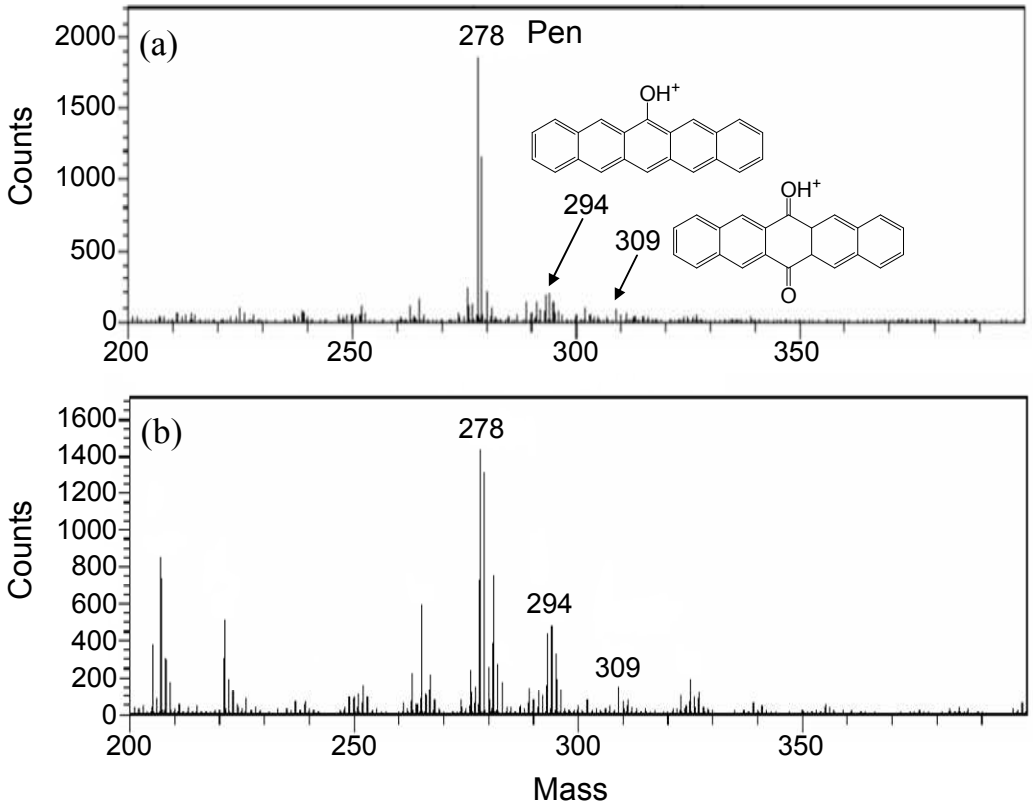

Figure 4.6: Surface mass spectrum of cations (a) for solution-processed (SP) film after three months, and (b) for vacuum-deposited (VD) film after three months. The inset molecules in (a) show the presumed pentacene-oxide cations, which are the most stable structures for $C_{22}H_{14}O^{+}$ and $C_{22}H_{13}O_2^{+}$.

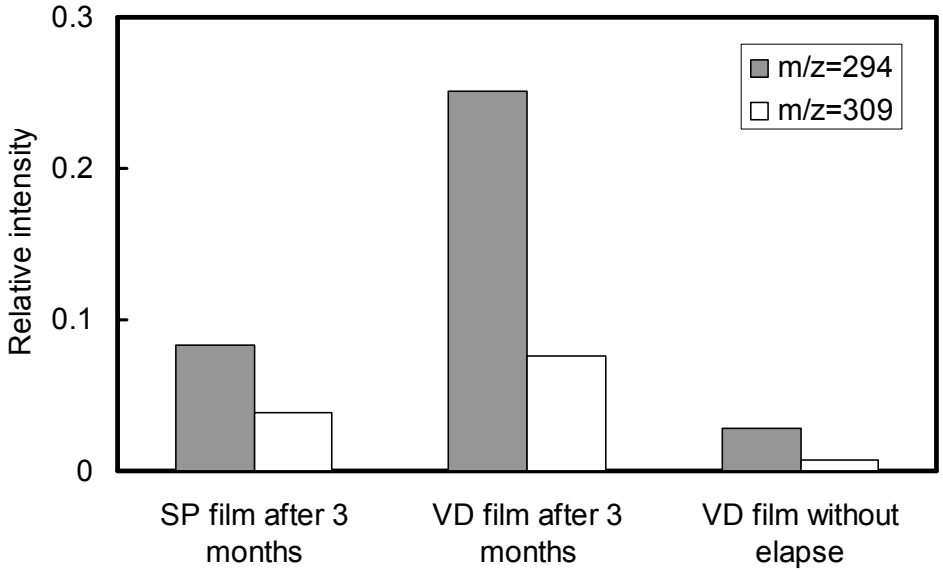

Figure 4.7: Relative intensities of oxidized pentacene determined from TOF-SIMS analysis. Relative intensities were normalized with the intensity of pentacene (*m*/*z* = 278) for each sample.

investigated in Refs. 25 and 26, respectively. Since the sensitivity of each fragment was not the same among the samples, the peak intensities of oxidized pentacene were normalized with that of pentacene for each sample. In this measurement, we focus on the determination of the oxidized pentacene impurities in the films and on the qualitative shift in the intensity of mass spectrum, since it is impossible to discuss the absolute amount of chemical impurities. The relative intensities of oxidized pentacene are shown in Figure 4.7. The intensity of oxidized pentacene has increased for three months considerably in the VD film. This result means that pentacene in the film is oxidized in the air to degrade into pentacenequinone. There is no doubt the VD film had a cleaner surface than the SP film at the initial stage; however, the SP film after three months showed lower relative intensity than the VD film in spite of similar storage term. This chemical stability of SP film was achieved due to significantly large domains with high crystallinity, that is, the large and rigid domains should prevent the atmospheric oxygen from penetrating into the film. In order to confirm this point, we analyzed an SP-pentacenequinone film by TOF-SIMS, and the relative intensity of the peak at m/z = 309 was 30 times larger than that of the stored SP-pentacene film.
Therefore, we can exclude the possibility that the oxidized-pentacene layer intrinsically forms at the film surface and act as a passivation layer in the case of the SP film.

Taking into consideration that $C_{22}H_{13}O$ defect can be regarded as one of the electrically active hole-trapping states [25], the generation of $C_{22}H_{13}O$ in the pentacene films should bring the increase in the total trap density, which is estimated from the analytical model of transistor characteristics. In addition, it is suggested that $C_{22}H_{12}O_2$ is generated gradually followed by the formation of $C_{22}H_{13}O$ and accordingly reduces the mobile hole carriers irreversibly to cause the threshold shift. $C_{22}H_{12}O_2$ impurities will also induce a local deformation in the pentacene lattice to create scattering centers, since 6,13-pentacenequinone can no longer take a herringbone structure in the crystal like pentacene [28]. Actually, the slight decline in the carrier mobility was confirmed both in the SP- and VD-TFTs, and moreover the VD-TFT showed a larger drop in the carrier mobility than the SP-TFT with longer storage.

4.5 Conclusion

The difference in electrical properties was investigated with respect to the SP- and VD-pentacene TFTs. Although the SP- and VD-TFTs exhibited the comparable maximum carrier mobility of ~0.3 cm^2/Vs, the subthreshold characteristics of both TFTs differed from each other. According to the analytical model related to the trap states, the SP film was estimated to have lower trap density with deeper trap level than the VD film. This discrepancy is attributed to the morphological difference in the films, that is, the SP film includes much fewer grain boundaries, in which the structural defects increase the trap states, than the VD film.

The electrical stability of the TFT performances during the long-term storage in air was also investigated. The increase in the total trap density and the reduction in the bulk carrier density were confirmed in both SP- and VD-TFTs, on the basis of the analytical models for transistor characteristics. The variations both in the total trap density and the bulk carrier density for the SP-TFT are estimated to be one order of magnitude lower than those for the VD-TFT, respectively. This means that the SP film is less sensitive to the air than the VD film. Using surface mass spectroscopy, the oxidized pentacene, $C_{22}H_{13}O$ and $C_{22}H_{12}O_2$ molecules were found to increase with storage time, especially in the case of the VD film. The SP film was found to be more chemically stable than the VD film, as is attributed to the large crystalline domains in the SP film. The increase in the total trap density and the reduction in the bulk carriers can be explained on the assumption that $C_{22}H_{13}O$ impurities act as electrically active hole-trapping states in the carrier transport, and that $C_{22}H_{12}O_2$ impurities followed by the generation of $C_{22}H_{13}O$ reduce the bulk hole carriers irreversibly to cause the negative threshold shift.

Finally, the degradation process in the pentacene films is suggested in the following items:

(i) The initial trap states for the SP- and VD-TFTs predominantly arise from the structural defects in the grain boundary rather than the chemical impurities.

(ii) The increase in the total trap density during the storage in air is caused by the

generation of the $C_{22}H_{13}O$ molecules, which should act as electrically active hole-trapping states in the carrier transport.

(iii) $C_{22}H_{12}O_2$ molecules, which are formed from $C_{22}H_{13}O$, irreversibly capture the bulk hole carriers, giving rise to the negative threshold shift. Furthermore, they also distort the pentacene lattice, thereby reducing the carrier mobility.

As a result, the remarkable advantage of the SP-TFT is that the large and rigid crystalline domains in the film inhibit the formation of hole-trapping states derived from the structural defects and the oxidation-induced chemical impurities.

References

1) H. Sirringhaus, P. J. Brown, R. H. Friend, M. M. Nielsen, K. Bechgaard, B. M. W. Langeveldvoss, A. J. H. Spiering, R. A. J. Janssen, E. W. Meijer, P. Herwig, D. M. de Leeuw, *Nature* **401**, 685 (1999).

2) H. Shirringhaus, R. J. Wilson, R. H. Friend, M. Inbasekaran, W. Wu, E. P. Woo, M. Grell, D. D. C. Bradley, *Appl. Phys. Lett.* **77**, 406 (2000).

3) M. S. A. Abdou, F. P. Orfino, Y. Son, S. Holdcroft, *J. Am. Chem. Soc.* **119**, 4518 (1997).

4) R. A. Street, A. Salleo, *Appl. Phys. Lett.* **81**, 2887 (2002).

5) L. Bürgi, T. J. Richards, R. H. Friend, H. Sirringhaus, *J. Appl. Phys.* **94**, 6129 (2003).

6) E. J. Meijer, G. H. Gelinck, E. van Veenendaal, B.-H. Huisman, D. M. de Leeuw, T. M. Klapwijk, *Appl. Phys. Lett.* **82**, 4576 (2003).

7) B. H. Hamadani, D. Natelson, *Appl. Phys. Lett.* **84**, 443 (2004).

8) P. T. Herwig, K. Mullen, *Adv. Mater.* **11**, 480 (1999).

9) A. Afzali, C. D. Dimitrakopoulos, T. L. Breen, *J. Am. Chem. Soc.* **124**, 8812 (2002).

10) S. K. Park, T. N. Jackson, J. E. Anthony, D. A. Mourey, *Appl. Phys. Lett.* **91**, 063514 (2007).

11) D. Knipp, R. A. Street, A. Völkel, J. Ho, *J. Appl. Phys.* **93**, 347 (2003).

12) B. H. Hamadani, D. Natelson, *J. Appl. Phys.* **97**, 064508 (2005).

13) G. B. Blanchet, C. R. Fincher, M. Lefenfeld, J. A. Rogers, *Appl. Phys. Lett.* **84**, 296 (2004).

14) G. Horowitz, P. Delannoy, *J. Appl. Phys.* **70**, 469 (1991).

15) G. Horowitz, R. Hajlaoui, H. Bouchriha, R. Bourguiga, M. Hajlaoui, *Adv. Mater.* **10**, 923 (1998).

16) G. Horowitz, R. Hajlaoui, P. Delannoy, *J. Phys. III* **5**, 355 (1995).

17) R. B. Campbell J. M. Robertson, J. Trotter, *Acta Crystallogr.* **15**, 289 (1962).

18) Y.-S. Yang, S.-H. Kim, J.-I. Lee, H.-Y. Chu, L.-M. Do, H. Lee, J. Oh, T. Zyung, M.-K. Ryu, M.-S. Jang, *Appl. Phy. Lett.* **80**, 1595 (2002).

19) K. P. Pernstich, S. Haas, D. Oberhoff, C. Goldmann, D. J. Gundlach, B. Batlogg, A. N. Rashid, G. Schitter, *J. Appl. Phys.* **96**, 6431 (2004).

20) D. Knipp, T. Muck, A. Benor, V. Wagner, *J. Non-Cryst. Solids* **352**, 1774 (2006).

21) R. Ye, M. Baba, K. Suzuki, Y. Ohishi, K. Mori, *Thin Solid Films* **464-465**, 437 (2004).

22) Y.-W. Wang, H.-L. Cheng, Y.-K. Wang, T.-H. Hu, J.-C. Ho, C.-C. Lee, T.-F. Lei, C.-F. Yeh, *Thin Solid Films* **467**, 215 (2004).

23) D. Li, E.-J. Borkent, R. Nortrup, H. Moon, H. Katz, Z. Bao, *Appl. Phys. Lett.* **86**, 042105 (2005).

24) E. J. Meijer, C. Detcheverry, P. J. Baesjou, E. van Veenendaal, D. M. de Leeuw, T. M. Klapwijk, *J. Appl. Phys.* **93**, 4831 (2003).

25) J. E. Northrup, M. L. Chabinyc, *Phys. Rev. B* **68**, 041202 (2003).

26) O. D. Jurchescu, J. Baas, T. T. M. Palstra, *Appl. Phys. Lett.* **84**, 3061 (2004).

27) G. Horowitz, *J. Mater. Res.* **19**, 1946 (2004).

28) A. V. Dzyabchenko, V. E. Zavodnik, V. K. Bel'skii, *Acta Crystallogr. B* **35**, 2250 (1979).

Chapter 5

Pentacene thin film transistors fabricated by solution process with directional crystal growth

5.1 Introduction

A variety of applications for organic semiconductors have been reported in organic electronics, such as thin film transistors (TFTs) [1–3], light-emitting diodes [4,5], photovoltaic cells [6,7], sensors [8,9], and radio-frequency ID-tags [10–12]. Moreover, several printing technologies, such as spin coating [13,14], stamping [15], and ink jetting [16,17], have been adopted for the fabrication of organic thin films at the same time, since the applicableness of organic semiconductors to the solution process could be the dominant feature in comparison with the silicon-based electronics. There is much ongoing research on soluble materials of small molecules, for example, substituted-acenes [18–20], and oligothiophenes [21–24]. In contrast, we have focused on the parent pentacene, and described the direct solution process and the superiority of the solution-processed pentacene films to the conventional vacuum-deposited one in the previous sections.

In this chapter, we focus on the crystal growth of pentacene from a solution, and subsequently discuss the application of the growth azimuth in the pentacene films to the solution process. Furthermore, the conditions for this drop casting are optimized in order to realize the large-area fabrication of pentacene thin films on glass substrates. Actually, this solution process was applied to the preparation of the transistor array for 5-inch-diagonal-sized liquid crystal displays (LCDs), and the obtained TFT arrays exhibited the uniform and high carrier mobilities as high as 1.0 cm^2/Vs [25].

5.2 Experimental procedure

5.2.1 Preparation and evaluation of thin film transistors

Pentacene was purchased from Tokyo Chemical Industry Co. (refined product by sublimation) and was used without further purification. Commercially available 1,2,4-tricholorobenzene (TCB) was used as the solvent after distillation. Pentacene was added to the TCB and heated at 200 °C to obtain 0.01 to 0.07 wt% solutions in a glove box under a nitrogen atmosphere. The solution was coated onto a substrate previously heated to 200 °C to form a pentacene thin film by evaporating the TCB. To enhance wetting of the solution on the substrate surface, we added polydimethylsiloxane (PDMS), obtained from Aldrich, to the pentacene solution to a concentration less than 50 ppm.

We used glass substrates with a 280-nm-thick silicon dioxide film as an insulator, which was prepared from polysilazane spin-coated over the 100-nm-thick Cr gate electrode and heated to 300 °C [25]. The source and drain electrodes were prepared using photolithography methods, electron beam deposition of 22/3-nm-thick Au/Ti, and cleaning by reactive-ion etching after a lift-off process. The bottom-contact configuration was adopted as the geometry of the electrode with a channel width (W) of 500 μm for all devices, and the channel length (L) was varied from 5 to 50 μm. The substrates were cleaned with oxygen plasma prior to the preparation of the pentacene thin films. The electrical properties of OTFTs were measured in air with a semiconductor parameter analyzer (Keithley 4200SC). The field effect mobility μ was calculated in the saturation region using equation (2-1).

5.2.2 Analysis for crystal growth mechanism

In-situ observations of crystal growth were carried out using an optical microscope with a heating and cooling stage (1002LS, Japan High Tech Co. Ltd.). The dispersed pentacene in TCB was enclosed in a cell of the stage unit under a nitrogen atmosphere, and the cell was mounted on the microscope stage. The dispersion in the cell was heated initially to 200 °C to form a uniform ca. 0.07-wt% solution of pentacene. Thereafter, the solution was cooled to yield crystal growth at a

cooling rate of 2 or 15 °C/min. The grown crystal domains were observed by polarized light.

Electron diffraction (ED) studies of the flat domain of the solution-processed pentacene thin films were carried out using a transmission electron microscope (TEM; HF-2000, Hitachi Ltd.). The pentacene films were covered with a water-soluble resin and were exfoliated together from the substrate. This was then floated on water to dissolve the resin, and the pentacene films left behind were picked up with a copper grid. The electron beam (λ = 0.0251 Å) was irradiated onto the sample in a perpendicular direction to the pentacene films on the copper grid. The stripe patterns on the pentacene film, corresponding to the growth direction, were checked prior to the ED analysis to confirm the direction of crystal growth.

The in-plane structure of the solution-processed thin films was investigated by grazing incidence X-ray diffraction (GIXD) [26], to confirm the relationship between the direction of the thin-film formation in the process and the crystallographic structure. The GIXD measurement was performed using an ATX-GSOR diffractometer with synchrotron radiation (λ = 1.00 Å) at the BL46XU in the SPring-8. The incident X-ray beam is radiated onto the sample surface at a grazing angle (typically < 0.5 degree). The X-ray detector is scanned in the in-plane direction to observe in-plane diffraction of the films. In this measurement, lattice planes perpendicular to the film surface can be detected. In addition, the in-plane two-dimensional azimuth of the pentacene crystalline film was subsequently analyzed by rotating the sample (ϕ axis) with a fixed angle of the detector at $2\theta_\chi$ = 18.0°, wherein the strongest diffraction was obtained in the previous measurements of the ϕ–$2\theta_\chi$ scan. Here, the origin of the sample rotation was set as the direction of the stripe patterns on the thin-film surface.

5.3 Results and discussion

5.3.1 Directional growth of solution-processed pentacene films

In-situ observations of pentacene crystal growth in the TCB solvent were carried out using the optical microscope with the thermally controllable stage unit. Figure 5.1 shows the crystal morphology for different cooling rates. The low cooling rate of 2 °C/min leads to plate-like crystal growth, while the high cooling rate of 15 °C/min results in dendritic pentacene crystals. The cooling rate is related to supersaturation of the solution, in other words, a fast cooling rate provides high supersaturation and vice versa. Furthermore, the plate-like crystal growth should evolve into flat domains of the solution-processed pentacene films, which always exhibit the stripe pattern. Here, we call these structures macro-stripe patterns. We have assumed that the macro-stripe patterns are related to the growth direction of the pentacene crystalline films.

The solution-processed films, in which the flat domains showed different directions of the macro-stripe patterns, were observed by a polarizing microscope, as shown in Figure 5.2. Some domains could be distinguished from the polarized image, with each domain having a different direction of the macro-stripe pattern. This implies that the macro-stripe patterns correspond to the crystal azimuth of the respective flat domains. We considered that the directionality of crystal growth is related to the evaporation direction. Drop casting was therefore carried out on a tilted substrate with a tilt angle of up to 0.5°. With a tilted substrate, the growth of the thin film proceeds approximately in one direction, since the thickness of the solution has a one-dimensional gradient. As shown in Figure 5.3, the obtained films showed a directionality of the macro-stripe patterns, with the direction of the macro-stripes mostly oriented towards the direction of the thin-film growth.

5.3.2 Growth azimuth of pentacene crystalline films

To investigate the relationship between the growth direction and crystal azimuth in the pentacene solution-processed films, we employed TEM measurements, and the TEM images obtained are shown in Figure 5.4. Another stripe pattern of ca. 0.2 μm width was observed in the TEM images; we named this the micro-stripe pattern.

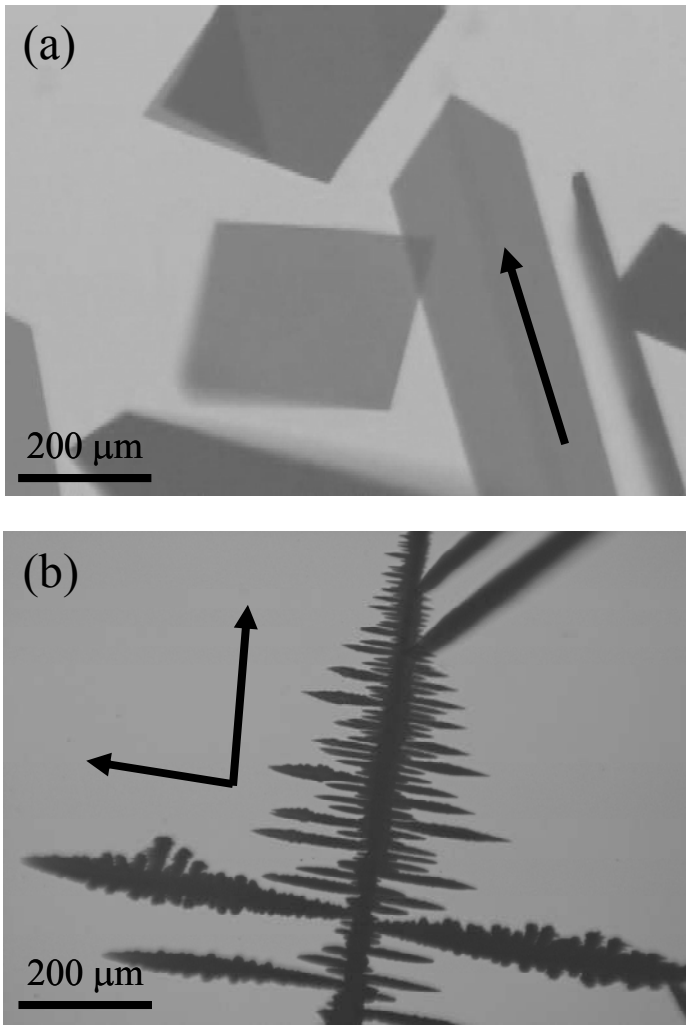

Figure 5.1: Crystal morphologies of pentacene from solution growth (a) at cooling rate of 2 °C/min and (b) 15 °C/min. The arrows in the images represent the growth directions with respect to each crystal.

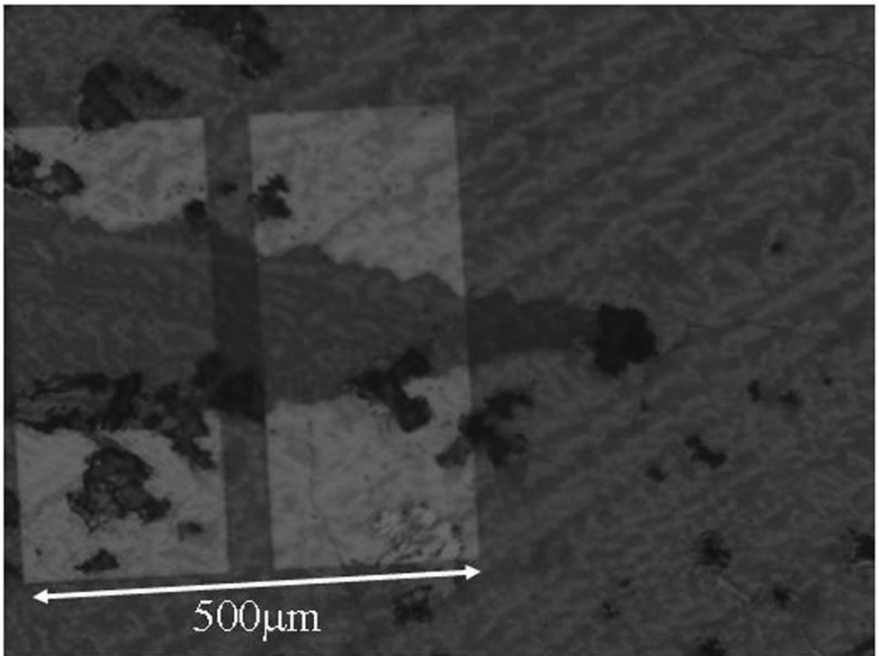

Figure 5.2: Polarized image of solution-processed pentacene thin film. The rectangles in the figure are source and drain electrodes.

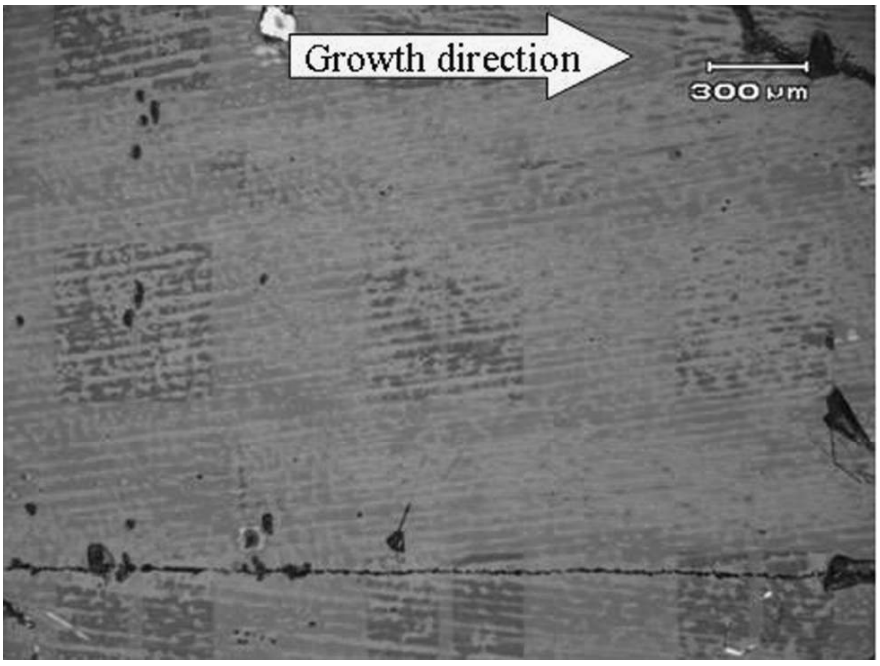

Figure 5.3: Optical microscope image for the solution-processed pentacene film with directional growth. Arrow represents the evaporation direction. The macro-stripe patterns were structured along the evaporation direction. The rectangles in the figure represent source and drain electrodes.

Although the direction of the micro-stripe patterns did not necessarily correspond to that of the macro-stripe patterns, we focused on the regions where the direction of both stripe patterns corresponded to each other in the azimuth. The inset image in Figure 5.4 represents the ED pattern observed simultaneously in the TEM measurement. In order to assign the respective diffractions, the obtained ED pattern was compared with ED simulation using the solution-grown crystal structure reported by Campbell *et al*. with the lattice parameters of a = 7.90 Å, b = 6.06 Å, c = 16.01 Å, α = 101.9°, β = 112.6°, and γ = 85.8° [27]. In the ED simulation, we used DIFFRACTION code implemented in Cerius^2 ver.3.8 (accelrys) for the simulation of electron diffraction pattern.

Recently, Siegrist *et al*. reported that the high-temperature pentacene polymorph is stable above 190 °C, and that the unit-cell parameters of this polymorph were similar to those reported by Campbell [28]. Furthermore, Della Valle *et al*. suggested that the structure reported by Campbell corresponds to the deepest minimum structure, using energy-minimization calculations with the quasi-Monte-Carlo sampling method [29]. These reports imply that pentacene crystal grown above 190 °C tends to have the structure reported by Campbell. In fact, the solution-processed pentacene thin film was found to have a structure close to that determined by Campbell in Chapter 3. Therefore, in the following, the crystal structure of pentacene will be discussed on the basis of the reduced Campbell's structure. In the ED simulation, Campbell's structure was redefined as a = 6.06 Å, b = 7.90 Å, c = 14.88 Å, α = 83.26°, β = 100.54°, and γ = 85.80°, since the original structure was not a reduced cell. The difference in the definition of a unit cell is displayed in Figure 5.5. The ED measurement in Figure 5.4 revealed that the direction of the stripe patterns on the film surface corresponded to (1 0 0) direction in the reduced Campbell's structure, that is, the (0 1 0) direction of the original one.

As further verification of the growth azimuth of the pentacene films, GIXD measurements were also carried out using synchrotron radiation at the SPring-8 (λ = 1.00 Å). The GIXD pattern of the ϕ–$2\theta_\chi$ scan for the solution-processed pentacene

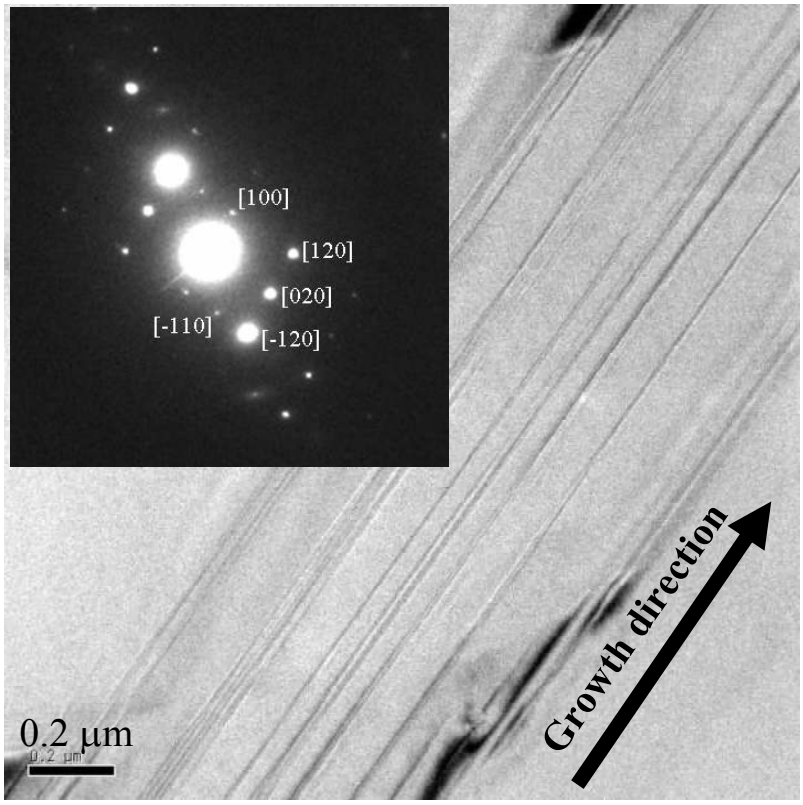

Figure 5.4: TEM image of the solution-processed pentacene film. The inset image is the electron diffraction pattern observed simultaneously with TEM. The direction of the micro-stripe pattern is in agreement with the growth direction of the solution-processed pentacene film in this case (the arrow in the figure).

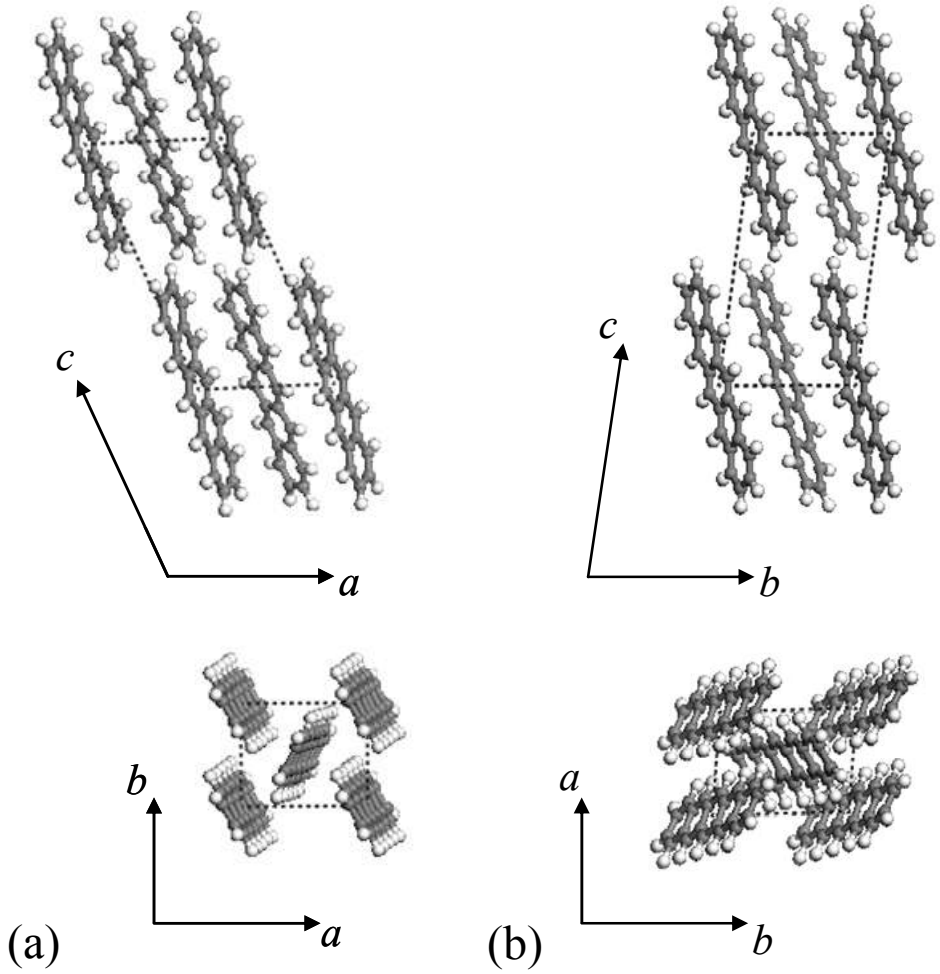

Figure 5.5: Crystal structure of pentacene (a) determined by Campbell *et al*., and (b) redefined structure.

film with directional growth is shown in Figure 5.6(a). A very strong peak is observed at $2\theta_\chi$ = 18.0°, which corresponds to the *d* spacing of 0.32 nm. This diffraction peak is assigned to the (1 −2 −1) lattice plane of the reduced Campbell's structure (calculated to be $2\theta_\chi$ = 18.0°). The (1 −2 −1) plane is confirmed to be almost perpendicular to the (0 0 1) plane, since the angle between these planes is calculated to be 90.4° from crystal structure data of the reduced Campbell's structure. In order to avoid confusion, the (1 2 0) and (1 −2 0) planes, which were also confirmed in the ED measurement, should be mentioned here. The calculated angle between (1 2 0) and (0 0 1) is 90.3°, almost perpendicular; however, the corresponding *d* spacing is 0.34 nm which should be observed at $2\theta_\chi$ = 16.8°. The (1 2 0) diffraction was actually confirmed at $2\theta_\chi$ = 16.82° with a low intensity of 10^3 cps in this measurement. On the other hand, simulations indicated that the (1 −2 0) plane was at $2\theta_\chi$ = 18.42° (*d* spacing = 0.31 nm) with low intensity, and the dihedral angle toward the (0 0 1) plane was estimated to be 78.0°. The (1 −2 0) plane cannot be detected in the GIXD measurement. Thus, it is reasonable to assign the peak at 18.0° to the (1 −2 −1) lattice plane. As shown in Figure 5.6(b), the in-plane distribution of the strong peak at $2\theta_\chi$ = 18.0° was subsequently investigated by rotating the sample (ϕ axis) with the fixed angle of detector at $2\theta_\chi$ =18.0°. In this measurement, we set the origin of the rotation angle approximately to the direction of the macro-stripe patterns, which was visible to the eye. It was revealed that the strongest peak was obtained in the narrow angle region from −56° to −52° with the peak top at −53.6°, while several peaks were detected in the other azimuth. In addition, the angle between (1 0 0) and (1 −2 −1) was calculated to be 54.9° from the crystal structure data. Since the difference in the azimuthal angle is only 1.3°, we conclude that the pentacene crystal growth from a solution proceeds along the minor axis (ca. 6 Å) in the *a*-*b* plane of the crystal structure of pentacene.

Using density functional calculations, Northrup *et al*. predicted an equilibrium crystal shape in terms of the surface energy of the crystal structure [30]. They employed the original Campbell's structure without any structural redefinition, and calculated the surface energies for the (0 0 1), (1 0 0), (0 1 0), (1 1 0), and (1 −1 0)

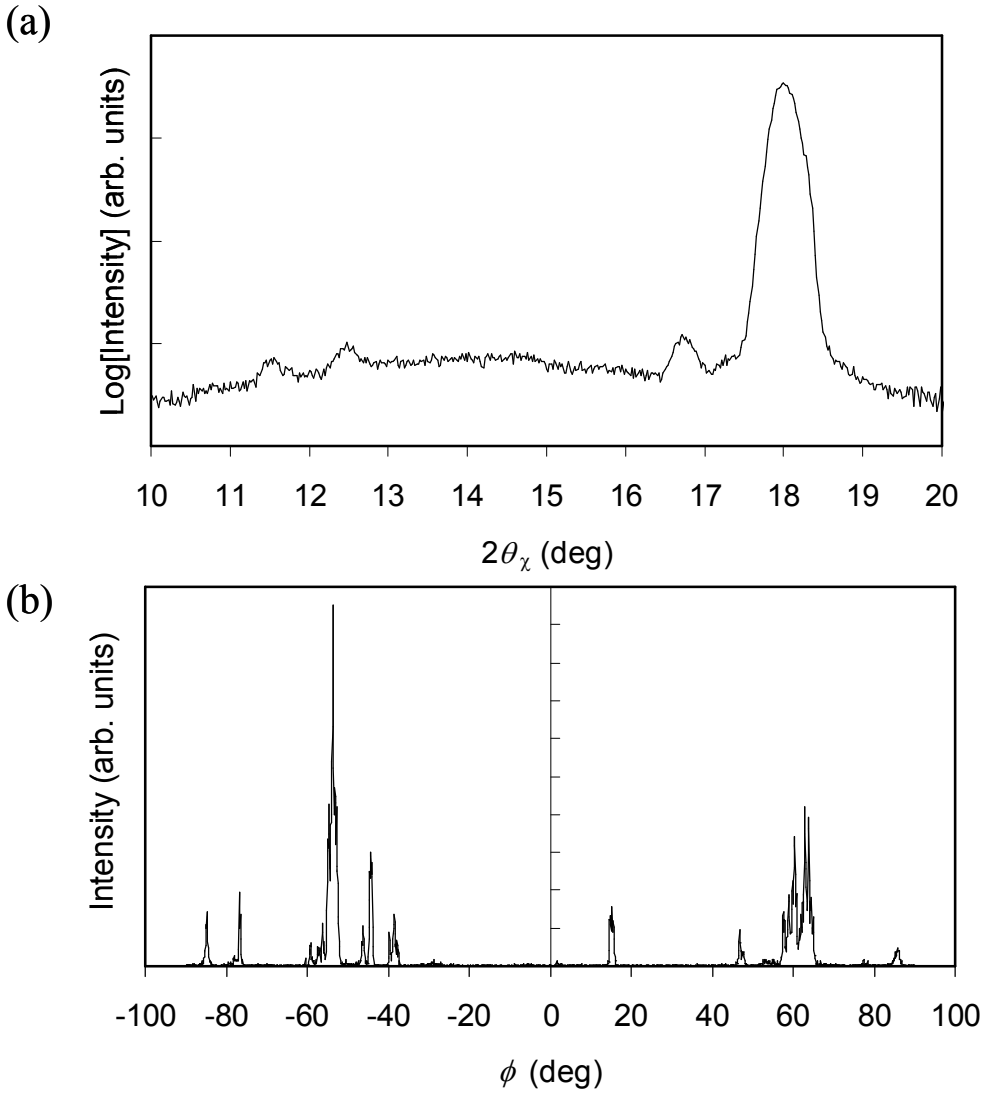

Figure 5.6: (a) GIXD pattern (λ = 1.00 Å) of the solution-processed pentacene thin film with directional growth. (b) In-plane distribution of diffraction at $2\theta_\chi$ = 18.0°, fixing the position of the detector during sample rotation of the ϕ axis.

surfaces. In addition, the theoretical form of the crystal can be derived from the relative growth rates of various low-index faces, since the growth rate of the crystal face is assumed to be proportional to its surface-formation energy [31,32]. The corresponding formation energies were also calculated to be 0.15, 0.45, 0.75, 0.71, and 0.72 eV/cell respectively in Ref. 30, that is, the (0 1 0) surface has the largest surface-formation energy. Therefore, pentacene molecules in a solution are likely to cohere to the (0 1 0) surface, and this facet will disappear from the equilibrium crystal shape [30]. It is worth noting again that the (0 1 0) surface mentioned here corresponds to the (1 0 0) surface of the reduced Campbell's structure in this chapter. Hence, the crystal growth was theoretically predicted to proceed preferably along the minor axis in the *a*-*b* plane of the pentacene crystal under equilibrium condition. This prediction implies that the flat-domain growth in this process takes place under nearly equilibrium condition.

5.3.3 Fabrication of transistor array

The solution process with directional growth was applied to a glass substrate with an area of 150×150 mm^2, wherein 10,000 transistors (W = 500 μm) were prepared in the center region of 100×100 mm^2 area (cf. Figure 5.9). The glass substrate was placed on a hot plate with a slight tilt and was sufficiently heated at 200 °C before drop casting of the pentacene solution. The direction of thin-film growth was parallel to that of the channel.

First, we emphasize that wetting of the solution on the substrate is important to stably provide two-dimensional growth of thin films. Since the drop casting itself is essentially a non-equilibrium process, it was difficult to control and restrain a phenomenon such as "*stick and slip movement*" at the edge of dropped solution without additives. It was found that the addition of PDMS of less than 50 ppm to the pentacene solution provides preferable wetting of the solution on the substrate, and that the solution on the tilted substrate can continuously evaporate from the upper side to the lower side of the dropped solution, even in the case of large-area substrates. Moreover,

the evaporation rate becomes moderate after starting the two-dimensional growth. The enhancement of wetting can be attributed to appropriate lowering of the surface tension of the solution and the interfacial tension between the solution and the substrate owing to the presence of an appropriate amount of PDMS. Although the exact mechanism for the enhancement in wetting has not been fully investigated at the present stage, this treatment was clearly found to make the drop casting controllable with simple experimental parameters as described below.

We focused on the surface-area-normalized amount of dropped solution and the concentration of the solution as process parameters to control the quality of the thin films. It is possible to apply the same condition to substrates with different sizes, by defining the surface-area-normalized amount of the dropped solution. These two parameters were optimized so that the best transistor characteristics were obtained. The optimum conditions for the amount and concentration of the dropped solution were found to be 0.058 ml/cm^2 and 0.05 wt%, respectively. In Figure 5.7(a), distributions of the transistor characteristics, mobility and threshold voltage in the TFT arrays fabricated using the best condition (condition 2) are displayed, and compared with conditions of 0.044 ml/cm^2 and 0.07 wt% (condition 1). The characteristics of transistors with L = 10 μm were evaluated at a drain voltage of −10 V, wherein 40 TFTs were randomly sampled from the TFT array of 100×100 mm^2 area. For condition 2, the characteristics converged well within a small distribution ranging from 0.2 to 1.1 cm^2/Vs for the carrier mobility (0.62 cm^2/Vs on average with standard deviation of 0.19 cm^2/Vs), and from −2.6 to −0.9 V for the threshold voltage (−1.8 V on average with standard deviation of 0.2 V), respectively. Moreover, the on/off ratio and the subthreshold slope showed good values of more than 10^4 and ranging from 0.5 to 1.1 V/decade, respectively. The transfer characteristics of OTFTs with the highest carrier mobility are shown in Figure 5.7(b). The maximum carrier mobility of 1.1 cm^2/Vs obtained may be one of the highest values ever reported measured at a low drain voltage in solution-processed OTFTs. In contrast, condition 1 resulted in low carrier mobility ranging from 0.01 to 0.52 cm^2/Vs with an average mobility of 0.13 cm^2/Vs.

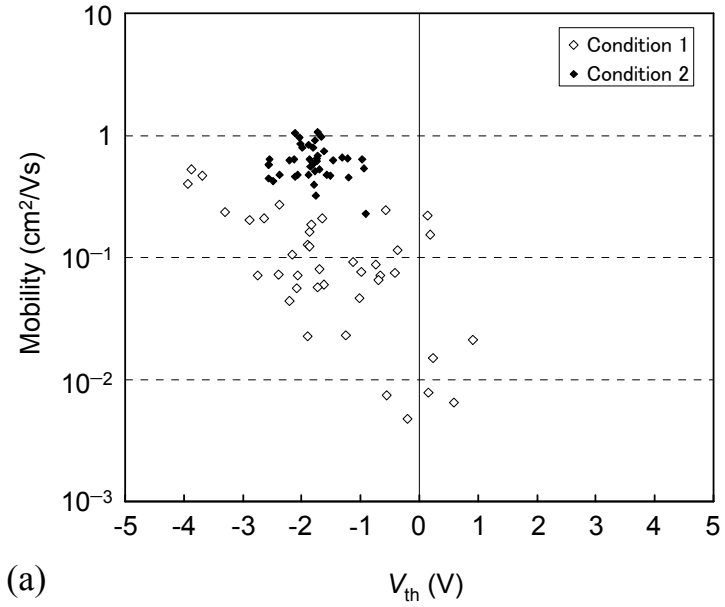

(a)

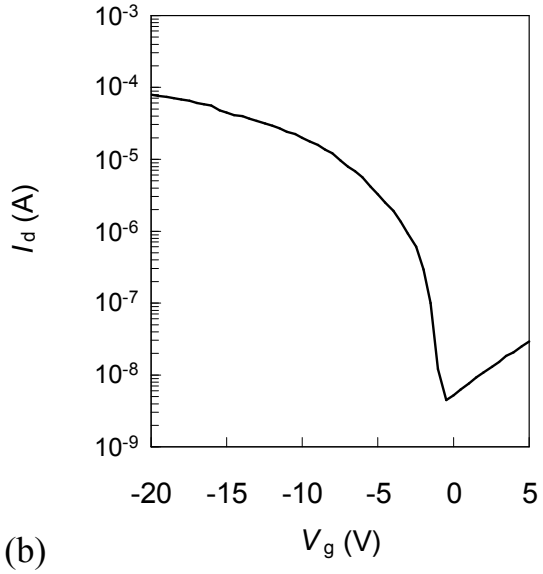

(b)

Figure 5.7: (a) Distributions of carrier mobility as a function of threshold voltage for conditions 1 and 2. In both cases, 40 TFTs were randomly sampled from each part of the TFT array. (b) Transfer characteristic of OTFT with the best carrier mobility from the TFT array fabricated using condition 2. The geometry of TFTs was W/L = 500/10 μm, and the applied drain voltage was −10 V for all measurements.

The area with lower carrier mobility in the array is comprised of dendritic domains as shown in Figure 5.8. The formation of dendritic domains occurs at the initial stage of film growth owing to high supersaturation accompanied by fast evaporation. In addition, the smaller amount of dropped solution results in widespread dendritic domains. Solution-processed films on 150×150 mm^2 glass substrates obtained using both conditions are shown in Figure 5.9. In the pictures, a part of the thin film is clouded due to the presence of dendritic domains or large roughness of the thick domains. In the case of condition 2, most of the area in the TFT arrays was covered with flat domains, and at the same time, the area of the dendritic domain was restricted to the edge of the glass substrate (Figure 5.9(b)), while the dendritic and thick domains covered a considerable area of the substrate when condition 1 was used as shown in Figure 5.9(a). In the course of the evaporation, the increasing vapor pressure should reduce the evaporation rate to change the growth mode from dendritic growth to two-dimensional growth, owing to lowering of the supersaturation. A similar phenomenon was confirmed in the in-situ observations of pentacene crystal growth.

The directionally grown films have color gradation from blue to violet, as seen in Figure 5.9. This color gradation is due to the gradient of the film thickness. The distribution of the film thickness obtained using condition 2 is displayed in Figure 5.10(b). The thickness was measured from cross-sectional profiling of the films, and 45 points (five points per division and nine divisions in an array) were evenly sampled from the respective area of the TFT array in the substrate. The TFT array was classified into nine divisions by separating three sections for each side, as *a–c* for the *x*-axis and *1–3* for the *y*-axis, respectively. The film growth proceeded in the direction from *a* to *c* along the *x*-axis. The thickness increased from 100 to 200 nm, accompanied by film growth, and the averaged thickness was approximately 150 nm. The distribution of the film thickness using condition 1 is also shown in Figure 5.10(a). The thickness gradually increased from 150 to 250 nm, accompanied by film formation, and the average thickness was ca. 200 nm. The concentration of the solution is roughly correlated with the thickness of the pentacene films. The dense solution

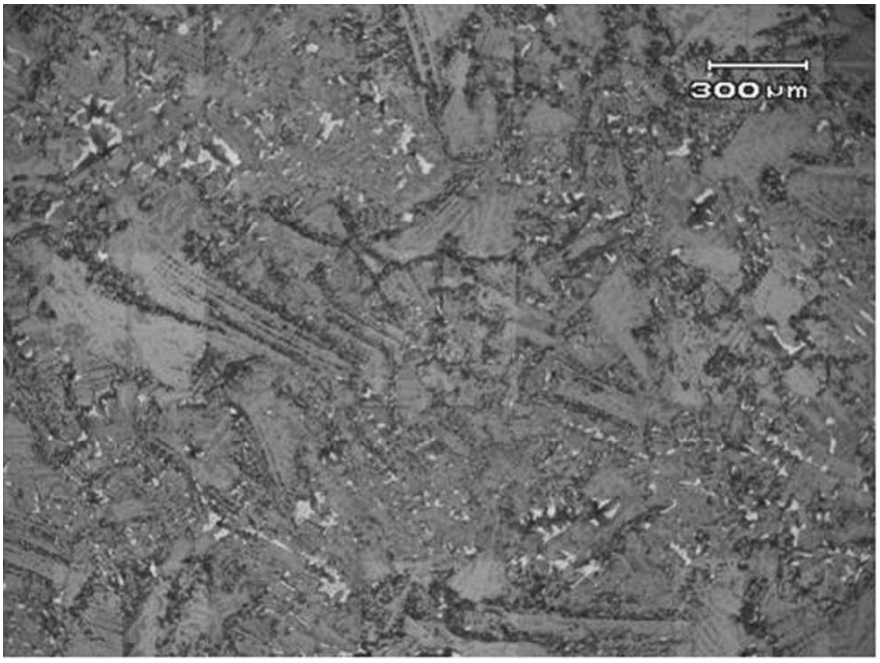

Figure 5.8: Optical microscope image of a typical dendritic domain.

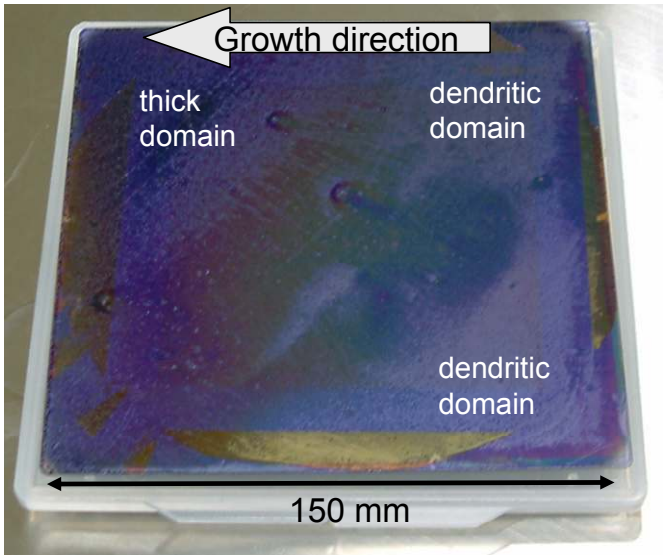

(a)

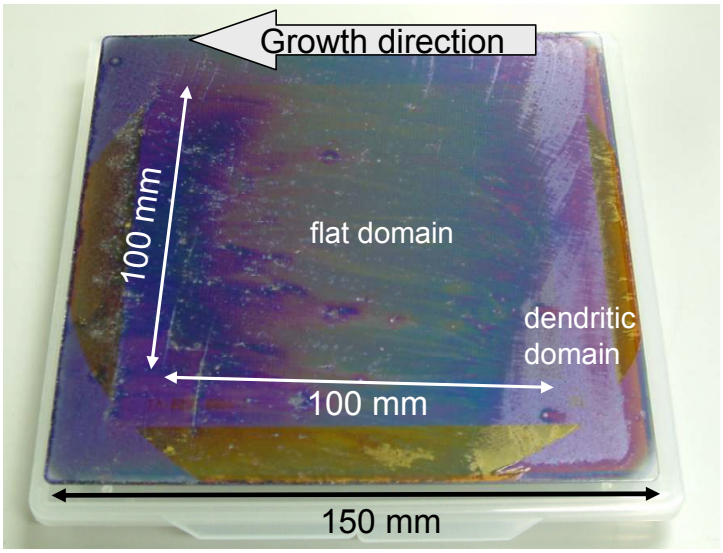

(b)

Figure 5.9: Solution-processed pentacene thin film on a glass substrate of area 150×150 mm^2, fabricated using (a) condition 1 and (b) condition 2. Both substrates were placed on a cover case for a 6-inch-square photomask. The outer area of the TFT array in the glass substrates was partially covered with gold in the electron beam deposition.

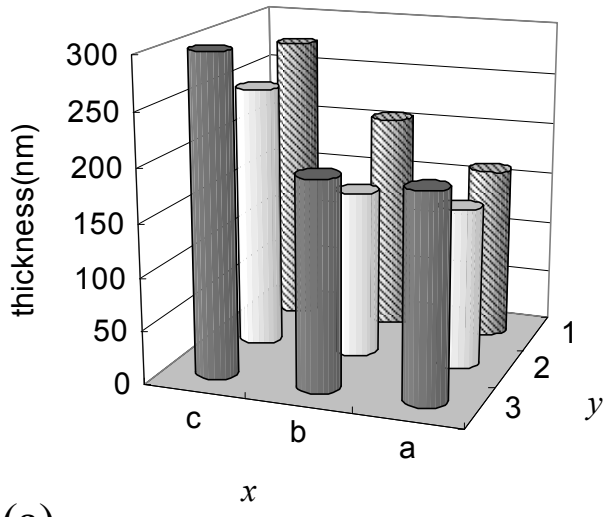

(a)

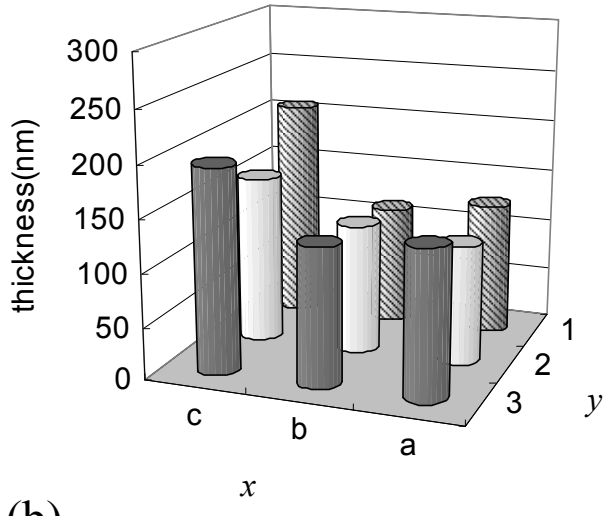

(b)

Figure 5.10: Distribution of thickness for the solution-processed pentacene film prepared using (a) condition 1 and (b) condition 2.

yielded thick films particularly at the end of evaporation, resulting in large roughness of the films. The rough surface could be an impediment in the post-processing of pentacene film formation, for example the sealing process for the liquid crystal layer. Thus, the intermediate concentration of 0.05 wt% was found to be desirable for application to TFT arrays [25].

The optimized process parameters thus successfully provided high quality solution-processed pentacene films, yielding high carrier mobilities. The directional growth also contributes to the high uniformity of TFT characteristics, even on large-area substrates, since the pentacene crystal has been reported to exhibit anisotropic carrier mobility both theoretically and experimentally [33,34]. This solution process was applied for the preparation of transistor arrays for 5-inch-diagonal-sized LCDs [25]. Figure 5.11 shows the fabricated twisted-nematic LCD with 240×320 pixels (QVGA) driven by the solution-processed OTFT array. Since the TFT performance is comparable with that of amorphous silicon, the TFT size can be reduced to the commercial size. The channel width and length of the TFTs are 50 and 8 μm, respectively. The aperture ratio of a dot with 318×106-μm size is designed to be 60 %.

5.4 Conclusion

We have successfully fabricated directional-solution-grown pentacene TFT arrays with high carrier mobilities, up to 1.1 cm^2/Vs, at a low drain voltage of −10 V. In addition, the distribution of TFT performance in an array showed high uniformity for both carrier mobility and threshold voltage, which were respectively 0.62 cm^2/Vs on average with standard deviation of 0.19 cm^2/Vs and −1.8 V on average with standard deviation of 0.2 V.

We found that the crystal growth direction in the pentacene film was accompanied by the thin-film growth direction, and that crystal growth proceeded preferably along the minor axis of the *a*-*b* plane in the crystal structure of pentacene. We applied this phenomenon to our solution process by dropping the solution onto tilted

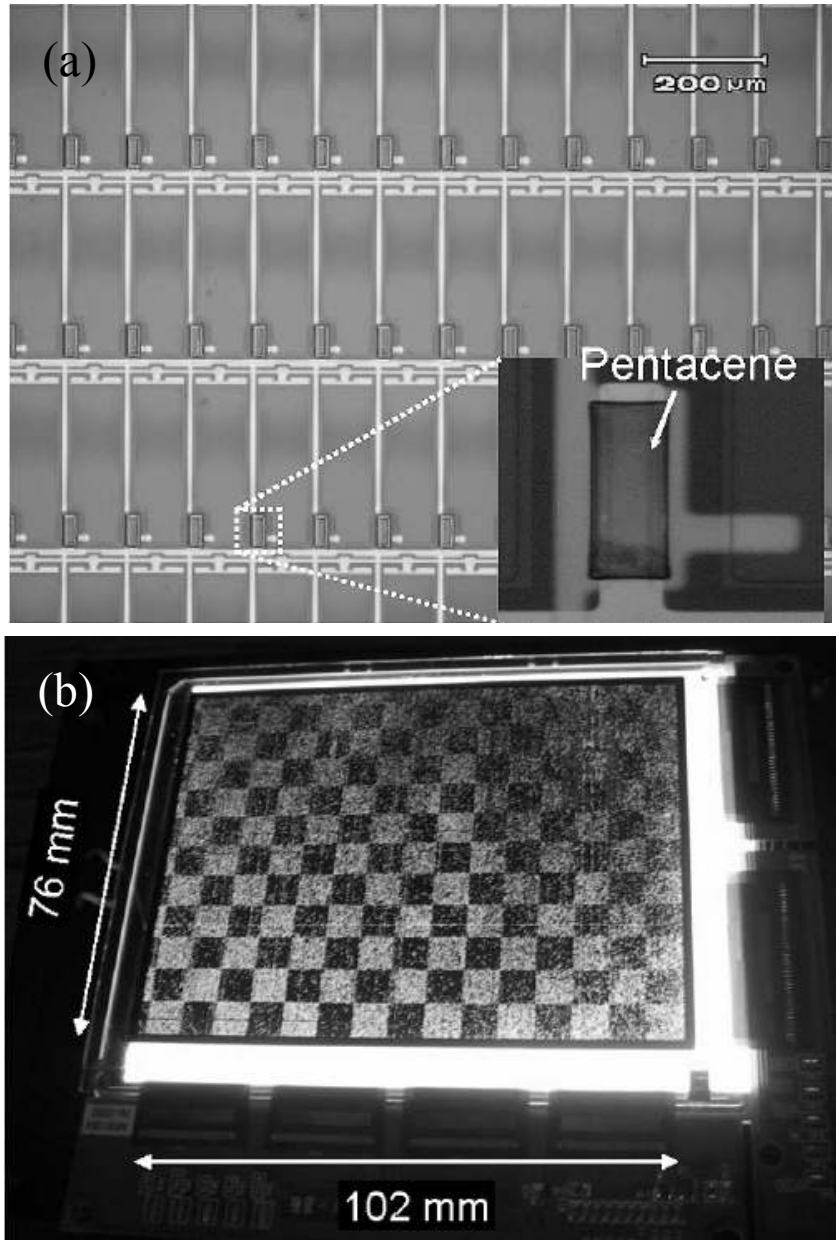

Figure 5.11: (a) Optical microscope image of the solution-processed OTFT array. The inset picture represents patterned and passivated pentacene films. (b) 5-inch-diagonal LCD driven by the solution-processed OTFTs. A black-and-white checkerboard pattern is displayed.

substrates, thereby obtaining high directionality of film growth.

This solution process with directional growth was applied to a large-area glass substrate with an area of 150×150 mm^2. To enhance the wetting of the pentacene solution on the substrate, we added a small amount of PDMS to the solution. With this treatment, good wetting on the substrate was realized, thereby making the drop-casting process controllable. We optimized the amount of the dropped solution and the concentration of the solution as prime parameters in the process to obtain the preferred films. This method was applicable to TFT arrays for LCDs, which were driven successfully.

References

1) G. Horowitz, *Adv. Mater.* **10**, 365 (1998).

2) Z. Bao, J. A. Rogers, H. E. Katz, *J. Mater. Chem.* **9**, 1895 (1999).

3) C. D. Simitrakopoulos, P. R. L. Malenfant, *Adv. Mater.* **14**, 99 (2002).

4) J. H. Burroughes, D. D. C. Bradley, A. R. Brown, R. N. Marks, K. Mackay, R. H. Friend, P. L. Burns, A. B. Holmes, *Nature* **347**, 539 (1990).

5) J. Kovac, L. Peternai, O. Lengyel, *Thin Solid Films*, **433**, 22 (2003).

6) C. J. Brabec, N. S. Sariciftci, J. C. Hummelen, *Adv. Funct. Mater.* **11**, 15 (2001).

7) K. M. Coakley, M. D. McGehee, *Chem. Mater.* **16**, 4533 (2004).

8) B. Crone, A. Dodabalapur, A. Gelperin, L. Torsi, H. E. Katz, A. J. Lovinger, Z. Bao, *Appl. Phys. Lett.* **78**, 2229 (2001).

9) T. Someya, H. E. Katz, A. Gelperin, A. J. Lovinger, A. Dodabalapur, *Appl. Phys. Lett.* **81**, 3079 (2002).

10) A. R. Brown, A. Pomp, C. M. Hart, D. M. Deleeuw, *Science*, **270**, 972 (1995).

11) B. Crone, A. Dodabalapur, Y.-Y. Lin, R. W. Filas, Z. Bao, A. LaDuca, R. Sarpeshkar, H. E. Katz, W. Li, *Nature*, **403**, 521 (2000).

12) C. J. Drury, C. M. J. Mutsaers, C. M. Hart, M. Matters, D. M. de Leeuw, *Appl. Phys. Lett.* **73**, 108 (1998).

13) F. Garnier, R. Hajlaoui, A. Yassar, P. Srivastava, *Science*, **265**, 1684 (1994).

14) H. Sirringhaus, N. Tessler, R. H. Friend, *Science*, **280**, 1741 (1998).

15) J. A. Rogers, Z. Bao, M. Meier, A. Dodabalapur, O. J. A. Schueller, G. M. Whitesides, *Synth. Met.* **115**, 5 (2000).

16) H. Sirringhaus, T. Kawase, R. H. Friend, T. Shimoda, M. Inbasekaran, W. Wu, E. P. Woo, *Science*, **290**, 2123 (2000).

17) S. P. Speakman, G. G. Rozenburg, K. J. Clay, W. I. Milne, A. Ille, I. A. Gardner, E. Bresler, J. H. Steinke, *Org. Electron.* **2**, 65 (2001).

18) P. T. Herwig, K. Mullen, *Adv. Mater.* **11**, 480 (1999).

19) A. Afzali, C. D. Dimitrakopoulos, T. L. Breen, *J. Am. Chem. Soc.* **124**, 8812 (2002).

20) S. K. Park, T. N. Jackson, J. E. Anthony, D. A. Mourey, *Appl. Phys. Lett.* **91**, 063514 (2007).

21) F. Garnier, R. Hajlaoui, A. El Kassmi, G. Horowitz, L. Laigre, W. Porzio, M. Armanini, F. Provasoli, *Chem. Mater.* **10**, 3334 (1998).

22) H. E. Katz, A. J. Lovinger, J. G. Laquindanum, *Chem. Mater.* **10**, 457 (1998).

23) H. E. Katz, W. Li, A. J. Lovinger, J. Laquindanum, *Synth. Met.* **102**, 897 (1999).

24) H. E. Katz, J. G. Laquindanum, A. J. Lovinger, *Chem. Mater.* **10**, 633 (1998).

25) M. Kawasaki, S. Imazeki, S. Hirota, T. Arai, T. Shiba, M. Ando, Y. Natsume, T. Minakata, S. Uemura, T. Kamata, *SID Inter. Symp. Digest Tech. Papers* **38**, 1761 (2007).

26) S. Matsuno, M. Kuba, T. Nayuki, S. Soga, P. W. T. Yuen, *Rigaku J.* **17**, 36 (2000).

27) R. B.Campbell, J. M. Robertson, J. Trotter, *Acta Crystallogr.* **15**, 289 (1962).

28) T. Siegrist, C. Besnard, S. Haas, M. Schiltz, P. Pattison, D. Chernyshov, B. Batlogg, C. Kloc, *Adv. Mater.* **19**, 2079 (2007).

29) R. G. Della Valle, E. Venuti, A. Brillante, A. Girlando, *J. Chem. Phys.* **118**, 807 (2003).

30) J. E. Northrup, M. L. Tiago, S. G. Louie, *Phys. Rev. B* **66**, 121404 (2002).

31) R. Docherty, G.. Clydesdale, K. J. Roberts, P. J. Bennema, *Phys. D: Appl. Phys.* **24**, 89 (1991).

32) Z. Berkovitch-Yellin, *J. Am. Chem. Soc.* **107**, 8239 (1985).

33) A. Troisi, G. Orlandi, *J. Phys. Chem. B* **109**, 1849 (2005).

34) J.Y. Lee, S. Roth, Y.W. Park, *Appl. Phys. Lett.* **88**, 252106 (2006).

Chapter 6

Thin films of pentacene formed by transferring crystals dispersed in liquid media

6.1 Introduction

Among the organic semiconductor transistors, pentacene is often studied because of its large carrier mobility and on/off ratio [1]. Due to the poor solubility of pentacene in common organic solvents, most of the studies are performed using vacuum deposited films [2,3]. The performance of the films strongly depends on the film structure, such as grain size [4,5] and texture [6,7]. Solution processing is a promising method for low-cost fabrication of thin films for large-area electronics. There have been several reports on solution processing by precursors [8,9] and substituted pentacene [10,11]. We have demonstrated a different approach to solution processing of thin films using the solutions of parent pentacene at elevated temperatures in the previous chapters. The solution-processed pentacene films show large platelet grain with well-defined crystal structure, and the thin-film transistors exhibit large carrier mobility. The films are assumed to be polycrystalline with single crystal domains, though the grain boundaries are not distinct from apparent film surface.

In this chapter, we demonstrate a new approach to forming thin films of pentacene by depositing pre-grown crystals using a liquid process. This method produces single or poly-crystalline thin films with distinct particulate grains. The films are fabricated by coating the dispersion of pentacene crystals in an organic solvent where the crystals are kept in solid state in the dispersion, and then the liquid media is vaporized to form the films. This fabrication process is unique since it is a “built-in system” in contrast to the “build-up system” of conventional thin films. In order to study the effect of grain boundary on the transport properties, several kinds of films are fabricated by changing the crystal size.

6.2 Experimental procedure

Crystalline particles of pentacene were grown in liquid phase from the solution. Crystals were prepared by cooling from a hot pentacene solution of 1,2,4-trichlorobenzene (0.07 we%) at 200 °C, and the crystal size can be varied by adjusting the cooling rate of the solution. Large rectangular or prismatic platelet crystals of up to millimeter in size were grown by slow cooling (1 °C/min), whereas small needle plate crystals with a width of a few micrometers were grown by rapid cooling (10 °C/min). These crystals are thin platelet and single domain crystals as observed by polarized microscopy. Small crystals of pentacene were prepared by dropping the hot solution into isopropanol, a poor solvent, which solidifies the solute. From these preparations, several kinds of crystals with sizes ranging from sub-micron to 50 μm were grown. After the growth of particulate crystals, pentacene crystals were concentrated by decantation of the mixture and were diluted with a dispersion media of isopropanol to form inks having a solid concentration of 1 wt%. The dispersion inks seemed to be relatively stable in air compared with a pentacene solution, since the blue color of the inks persisted during storage in air for several weeks. Thin films were prepared by the drop casting of the dispersion ink on the substrate and vaporizing the dispersion media at room temperature under a nitrogen atmosphere.

Thin-film transistors (TFTs) were fabricated by forming the films on SiO_2/Si substrates with patterned Ti (3 μm) under-layered with Au (22 μm) as source and drain electrodes. The same silicon wafers are used as presented in section 2.2.1. The SiO_2 surface was treated with hexamethylenedisilazane.

The electrical properties of OTFTs were measured with a semiconductor parameter analyzer (Keithley 4200SC). The field effect mobility μ was calculated in the saturation region from the slope of the linear part of an $I_{d,sat}^{1/2}$ vs. V_g plot, using equation (2-1). Temperature dependence of the carrier mobility of the transistors was also examined in the reduced pressure of 10^{-2} Pa from room temperature to 423 K.

6.3 Results and discussion

6.3.1 Thin film morphologies and transistor characteristics

Thin films were composed of assembled platelet-shaped crystals, and most of the crystal planes faced the substrate surface. This was confirmed by optical and scanning electron microscopy as shown in Figures 6.1(a)–(c). Molecular orientation of the films was confirmed by measuring the wide-angle X-ray diffraction, which reveals that the long molecular axes of pentacene are oriented in the films perpendicularly to the substrate plane. The *d*-spacing of 14.5 Å for (0 0 1) plane indicates that the crystal structure is mainly bulk phase.

The carrier mobility was plotted with the threshold voltage as shown in Figure 6.1(d), and typical transfer characteristics are shown in Figure 6.2. Single domain thin films, which consist of large crystal grains exceeding the channel length, exhibit an average carrier mobility of 1 cm^2/Vs. This value is comparable to single crystal transistors [12]. We believe that the wide distribution of the mobility and the threshold voltage is an effect of the inhomogeneous contact on the substrate, as observed from the surface view of the films.

Transistors of assembled small crystals with diameter less than the channel length performed well. The carrier mobility of the transistor deceases with the crystal size, thus a narrower distribution of the carrier mobility and threshold voltage was confirmed. It is assumed that the defects such as grain boundaries and vacancies in the films are uniformly distributed.

6.3.2 Influences of grain boundaries

The influence of grain boundaries can be identified from the relation between the channel length and carrier mobility presented in Figure 6.3. While the carrier mobility is independent of the channel length in case of the films assembled with large and medium crystals, those in the films with small crystals slightly increase with decreasing channel length. We believe that the effect of grain boundaries is negligible

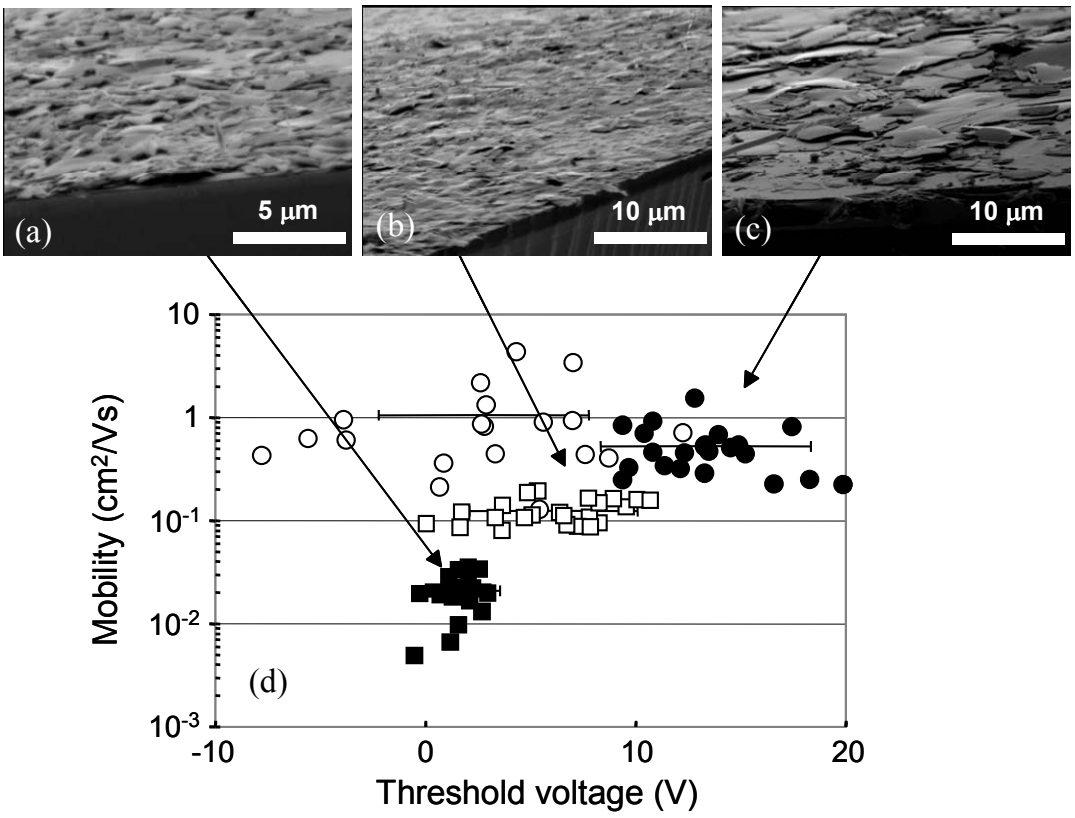

Figure 6.1: Surface views of crystalline assembled thin films obtained by scanning electron microscopy. The average crystal diameters in the films were approximately (a) 0.5, (b) 2, and (c) 10 μm, respectively. (d) Distribution of carrier mobility as a function of threshold voltage of the thin film transistors. The plots for open circle are the transistors assembled with large crystals of average diameter around 50 μm. The transistors were formed with a channel length of 20 μm.

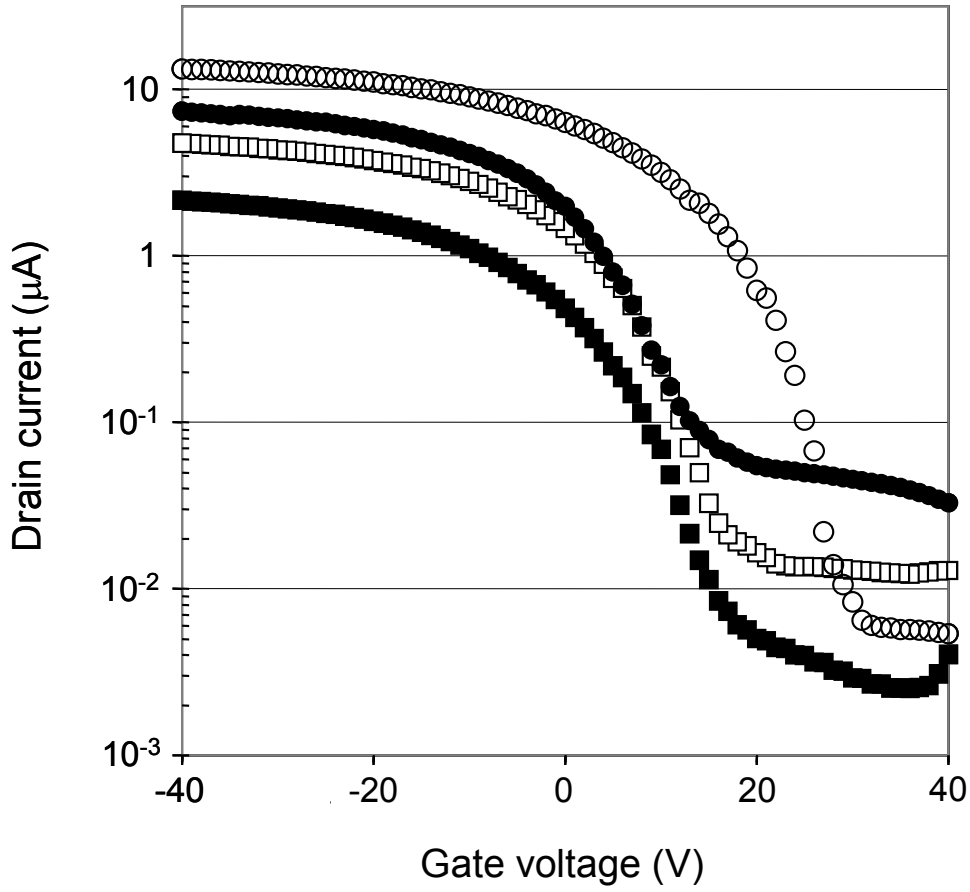

Figure 6.2: Typical transfer characteristics for the transistors (V_d = −20 V and W/L = 500/20 μm) with the respective average diameters of crystal; 50 (open circle), 10 (solid circle), 2 (open square), and 0.5 μm (solid square).

in short channel transistors and that the electrode contact resistance of the transistors is relatively small, since the ordinary organic transistors show higher carrier mobility with wider channel and have large electrode contact resistance [13]. The electrode contact resistance of the transistors was studied based on a transmission line model test structures [14–16]. Within this model, it is assumed that the ON resistance, R_{on}, which is extracted from the slope of linear region of TFT output characteristics, consists of the channel resistance, R_{ch} and the contact resistance, R_c, under the condition of low drain voltage and high gate voltage. The R_{ch} is a function of the channel length, L, and the gate voltage. Therefore, the R_c can be obtained from the intercept of the R_{on} (= R_{ch} + R_c) vs. L plot at $L = 0$. The resistance between the source and drain electrodes at low applied drain voltage in a linear regime is plotted with the channel length. The assumed R_c of 10 to 100 kΩ is very small compared to the R_{ch} of 1 to 10 MΩ at the gate voltage ranging from −60 to −10 V (W = 500 μm) with respect to all films with different crystal diameters.

The transport barrier between grain boundaries of the films was studied from the temperature dependence of the carrier mobility as shown in Figure 6.4. The barrier heights were determined from the slope to be 56, 11, and 0 meV for the small, medium and large crystal, respectively. They are considerably small compared to the conventional organic thin films of conducting polymers and are comparable to the sublimed thin films of pentacene [17,18]. A plausible explanation for the good contact is that the crystals form large contact planes with a smooth surface [19]. Since the film morphology of the crystal-assembled films is different from that of the conventional sublimed films, further studies are needed to explain the transport path and the barrier heights extracted from the temperature dependence, which would be correlated with the inter-grain structure.

6.4 Conclusion

In conclusion, thin films of pentacene have been fabricated by transferring a

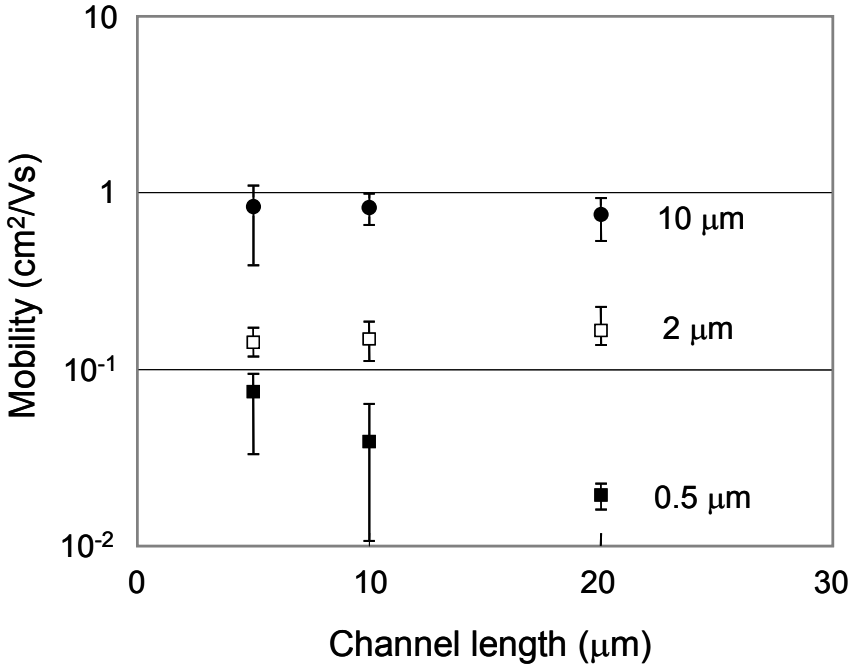

Figure 6.3: Channel length dependence on the carrier mobility of the film transistors. The average crystal diameters in the films were ca. 10 (solid circle), 2 (open square), and 0.5 μm (solid square), respectively.

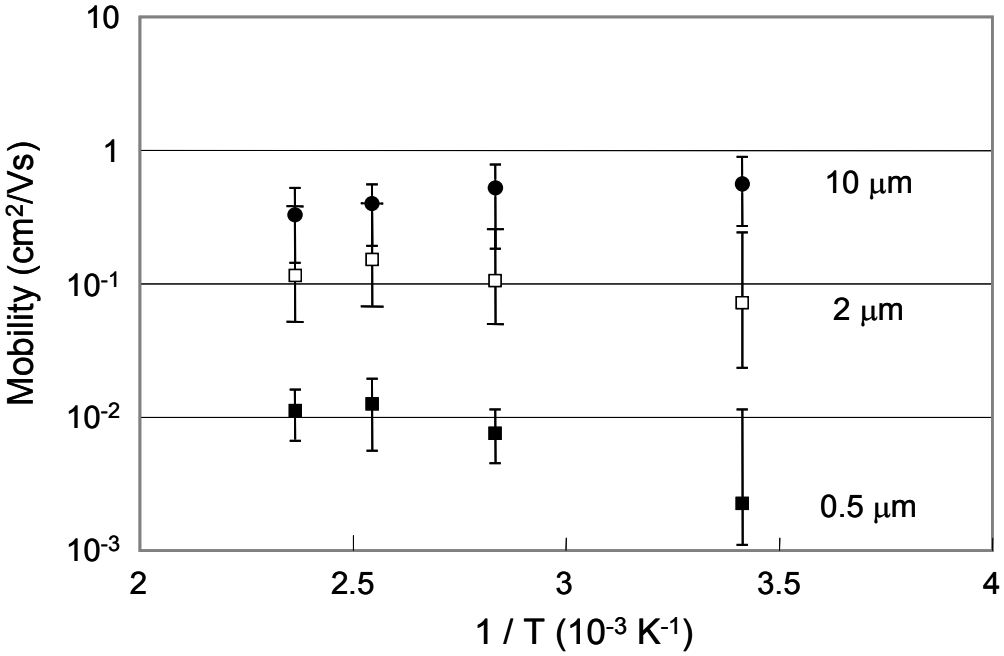

Figure 6.4: Temperature dependence of the carrier mobility of the film transistors. The average crystal diameters in the films are ca. 10 (solid circle), 2 (open square), and 0.5 μm (solid square), respectively.

dispersion of pre-grown crystals in liquid media. Single domain and multi-domain transistors were formed by changing the crystal size and showed a good performance. Single domain thin films assembled with large crystal grain sizes exceeding the channel length exhibited an average carrier mobility of 1 cm^2/Vs.

The interfacial properties including both the contact resistance at the semiconductors/electrodes interface and the transport barrier height in the films were found to be small. The electrode contact resistance of the transistors was studied by the transmission line model. The contact resistance was estimated to be 10 to 100 kΩ, which is considerably small compared to the channel resistance of 1 to 10 MΩ. Temperature dependence of the carrier mobility of the transistors was also examined, in order to extract the transport barrier between grain boundaries of the films. The barrier heights were determined to be 56, 11, and 0 meV for the small, medium and large crystal, respectively. These results indicate that the films with assembled crystals had a unique texture and further applications are expected in the future.

References

1) D. J. Gundlach, Y. -Y. Lin, T. N. Jackson, S. F. Nelson, D. G. Schlom, *IEEE Electron Device Lett.* **18**, 87 (1997).

2) R. Ruiz, A. Papadimitratos, A. C. Mayer, G. G. Malliaras, *Adv. Mater.* **17**, 1795 (2005).

3) R. Schroeder, A. Majewski, M. Grell, *Appl. Phys. Lett.* **83**, 3201 (2003).

4) D. Knipp, R. A. Street, A. Völkel, J. Ho, *J. Appl. Phys.* **93**, 347 (2003).

5) J. G. Laquindanum, H. E. Katz, A. J. Lovinger, A. Dodabalapur, *Adv. Funct. Mater.* **8**, 2542 (1996).

6) W. Y. Chou, H. L. Chen, *Adv. Funct. Mater.* **14**, 811 (2004).

7) S. H. Jin, H. U. Seo, D. H. Nam, W. S. Shin, J. H. Choi, U. C. Yoon, J. W. Lee, J. G. Song, D. M. Shin, Y. S. Gai, *J. Mater. Chem.* **15**, 5029 (2005).

8) A. Afzali, C. D. Dimitrakopoulous, T. L. Breen, *J. Am. Chem. Soc.* **124**, 8812 (2002).

9) A. R. Brown, A. pomp, D. M. de Leeuw, D. B. M. Klassen, E. E. Havinga, P. T. Herwig, K. Mullen, *J. Appl. Phys.* **79**, 2136 (1996).

10) M. M. Payne, S. R. Parkin, J. E. Anthony, C. -C. Kuo, T. N. Jackson, *J. Am. Chem. Soc.* **127**, 4986 (2005).

11) V. C. Sundar, J. Zaumseil, V. Podzorov, E. Menard, R. L. Willett, T. Someya, M. E. Gershenson, J. A. Rogers, *Science* **303**, 1644 (2004).

12) J. Y. Lee, S. Roth, Y. W. Park, *J. Appl. Phys.* **88**, 252106 (2006).

13) H. Klauk, G. Schmid, W. Radlik, W. Weber, L. Zhou, C. D. Sheraw, J. A. Nichols, T. N. Jackson, *Solid-State Electron.* **47**, 297 (2003).

14) S. Luan, G. W. Neudeck, *J. Appl. Phys.* **72**, 766 (1992).

15) P. V. Necliudov, M. S. Shur, D. J. Gundlach, T. N. Jackson, *Solid-State Electron.* **47**, 259 (2003).

16) H. Klauk, G. Schmid, W. Radlik, W. Weber, L. Zhou, C. D. Sheraw, J. A. Nichols, T. N. Jackson, *Solid-State Electron.* **47**, 297 (2003).

17) C. Goh, N. Kline, M. D. McGehee, E. N. Kadonikova, J. M. Frecht, *Appl. Phys. Lett.* **86**, 122110 (2005).

18) S. F. Nelson, Y. Y. Lin, J. D. Gundlach, T. N. Jackson, *Appl. Phys. Lett.* **72**, 1854 (1998).

19) K. Sato, T. Sawaguchi, M. Sakata, K. Itaya, *Langmuir* **23**, 12788 (2007).

Chapter 7

General conclusion

In the present thesis, the electronic properties and thin-film structures of the organic semiconductors were investigated. We confirmed that pentacene is most preferable for the active layer of thin-film transistors (TFTs) among several polycyclic aromatic hydrocarbons (PAHs). Moreover, we first proposed a novel solution processing approach using pentacene and successfully extended it to the fabrication of large-area TFT arrays. The surface morphology and crystalline structure of the solution-processed pentacene films were also studied to clarify their advantage to the conventional vacuum-deposited one.

In Chapter 2, we have investigated the carrier mobility of vacuum-deposited PAH-TFTs and the crystalline structure of PAH thin films, where pentacene, ovalene, dibenzocoronene, and hexabenzocoronene were used as organic semiconductors. Using a first-principles calculation, the electronic structures of 2D molecular layer of PAHs were also investigated on the basis of the XRD analysis and crystal structural data. Pentacene exhibits the highest carrier mobility among these PAH-TFTs, as is attributed both to the two-dimensionally large π-electron interactions between neighboring molecules and the preferable lateral networks in the grain boundary due to the large grain size.

In Chapter 3, we have investigated the solubilization of pentacene in trichlorobenzene (TCB) under inert atmosphere and presented the direct solution process. Two types of surface morphologies, flat and rough domains, were confirmed according to the preparation condition, i.e. the supersaturation derived from the evaporation rate. The flat domain of TFT exhibited higher carrier mobility than the rough domain, since the flat domain was found to consist of continuously spreading domains including large single-crystal-like crystallites. In this chapter, the unit cell of

the solution-processed pentacene film was estimated by grazing-incidence X-ray diffraction (GIXD) method, and was found to take a crystal structure similar to that reported by Campbell *et al*.

In Chapter 4, the air stability of solution-processed pentacene TFTs was investigated in comparison with the vacuum-deposited one. The significant difference of transistor characteristics especially in the subthreshold region was revealed, and it implies that the solution-processed films contain lower trap density than the vacuum-deposited one, on the basis of the simple analytical model related to the trap states, which was proposed by Horowitz and Delannoy. In addition, the shift of the threshold voltage was confirmed for both TFTs during long-term storage in air and dark condition. According to the analytical models, these threshold shifts can be attributed to the increase of trap density and the decrease of bulk carrier density in the films, and the variations in both densities for the solution-processed film were one order of magnitude lower than those of the vacuum-deposited one. Using the surface mass spectroscopy, the oxidation-induced chemical impurities, e.g. $C_{22}H_{13}O$ (oxypentacene) and $C_{22}H_{12}O_2$ (pentacenequinone) molecules were identified on the film surfaces, and their amounts increased with the aging time in particular in the case of the vacuum-deposited films. We proposed the hypothesis of the degradation mechanism as follow: (i) The initial trap states for both TFTs arise from the structural defects in the grain boundary more dominantly rather than the chemical impurities. (ii) The increase in the total trap density during the storage in the air is caused by the generation of the oxypentacene, which should act as electrically active hole-trapping states in the carrier transport. (iii) Pentacenequinone, which is formed resultantly from oxypentacene, captures the bulk hole carriers irreversibly to give rise to the negative threshold shift. The large and rigid crystalline domains in the solution-processed film inhibit the formation of hole-trapping states derived from the structural defects and the oxidation-induced chemical impurities.

In Chapter 5, we have successfully fabricated a solution-processed pentacene TFT array with uniform and high carrier mobility up to 1.1 cm^2/Vs. It was achieved

by controlling growth direction of pentacene films from solution, and by optimizing conditions for drop-casting. We discovered the directional growth of pentacene crystal in solution and applied it to our solution process. Crystal growth azimuth was also investigated using electron diffraction and GIXD analysis, and the crystal growth of pentacene is revealed to proceed preferably along to the minor axis in the *a*-*b* plane of the unit cell. The enhancement in wetting of pentacene solution enable us to handle the conditions for the drop-casting even on the large-area substrates of 150×150 mm^2, and consequently the large continuous pentacene films can be obtained steadily. As a result, our solution process was utilized for preparation of the transistor array for 5-inch-diagonal-sized liquid crystal displays, and it was also driven satisfactorily.

In Chapter 6, thin films of pentacene have been fabricated by transferring a dispersion of pre-grown crystals in liquid media. Single domain and multi-domain transistors were formed by changing the crystal size. Single-domain thin films assembled with large crystal exhibited an average carrier mobility of 1 cm^2/Vs. The electrode contact resistance of the transistors was estimated to be 10 to 100 kΩ, which is considerably small compared to the channel resistance. Temperature dependence of the carrier mobility of the transistors was also examined, in order to extract the transport barrier in the films. The barrier heights were determined to be 56, 11, and 0 meV for the small, medium and large crystal, respectively.

In summary, we have shown the possibility of the application of organic semiconductors to the electronic devises. We believe that the OTFT using small molecules is the most promising candidate for the flexible display manufactured by printing technologies.

List of publications

Chapter 2

1) Y. Natsume, T. Minakata, and T. Aoyagi, "Structures and electronic properties of thin films of polycyclic aromatic hydrocarbons" *Thin Solid Films*, **517**, 3005–3010 (2009).

Chapter 3

2) T. Minakata and Y. Natsume, "Direct formation of pentacene thin films by solution process" *Synth*. *Met*. **153**, 1–4 (2005).

3) Y. Natsume, T. Minakata, and T. Aoyagi, "Crystalline structure of solution-processed pentacene thin film" *Synth*. *Met*., **159**, 338–342 (2009).

Chapter 4

4) Y. Natsume and T. Minakata, "Pentacene thin-film transistors fabricated with a simple solution process" *Mater*. *Res*. *Soc*. *Symp*. *Proc*. **937**, M-10-32 120–125 (2006). (published online)

5) Y. Natsume "Characterization of solution-processed pentacene thin film transistors" *Phys. Stat. Sol. (a)* **205**, 2958–2965 (2008).

Chapter 5

6) Y. Natsume, T. Minakata, and T. Aoyagi, "Pentacene thin film transistors fabricated by solution process with directional crystal growth" *Org*. *Electron*. **10**, 107–114 (2009).

Chapter 6

7) T. Minakata and Y. Natsume, "Thin films of pentacene formed by transferring crystals dispersed in liquid media" *Appl*. *Phys*. *Lett*. **93**, 153306 1–3 (2008).

The publications not included in this thesis

8) M. Kawasaki, S. Imazeki, S. Hirota, T. Arai, T. Shiba, M. Ando, Y. Natsume, T. Minakata, S. Uemura, and T. Kamata, "High mobility solution-processed organic thin-film transistor array for active-matrix color liquid crystal displays" *J. Soc. Inf. Display* **16**, 161–167 (2008).

9) Y. Misaki, Y. Natsume, K. Takahashi, H. Fueno, and K. Tanaka, "Synthesis and properties of new extended TTP analogs" *Synth. Met.* **135–136**, 671–672 (2003).

10) N. Ando, S. Tasaki, Y. Hato, C. Marumo, Y. Natsume, S. Ohmori, A. Ito, and K. Tanaka, "Effects of heat treatment on electrochemical behavior of polyacenic semiconductive electrode for lithium ion battery" *J. Therm. Anal. Calorim.* **70**, 301–308 (2002).

11) A. Ito, Y. Natsume, S. Ohmori, and K. Tanaka, "Electronic structures of very this carbon nanotubes: Are they still π-electronic materials?" *Nano Lett.* **2**, 629–633 (2002).

12) N. Ando, Y. Hato, T. Yoshii, Y. Natsume, A. Ito, and K. Tanaka, "Correlation of Li ion and the environmental elements in the surface nano-reaction field of polyacenic semiconductive material as the battery electrode" *Thin Solid Films* **393**, 177–185 (2001).

Acknowledgments

The present thesis is based mainly on the study carried out under the national project, Advanced Organic Device Project, which was entrusted to the Optoelectronic Industry and Technology Development Association (OITDA) by the New Energy and Industrial Technology Development Organization (NEDO). The author joined the national project from 2004 to 2007.

The author would like to express his greatest gratitude to Professor Kazuyoshi Tanaka of Kyoto University for his supervision of this thesis with kind suggestions, discussions, and continuous encouragements.

He is deeply grateful to all the members of the national project, especially Dr. Toshihide Kamata and Dr. Yuji Yoshida of National Institute of Advanced Industrial Science and Technology; Mr. Masahiro Kawasaki, Dr. Shuji Imazeki, and Dr. Masahiko Ando of Hitachi, Ldt. for their collaboration in the development of the transistor arrays for liquid crystal display.

He also wishes to acknowledge his colleagues and managers at Asahi Kasei Corporation, in particular, Dr. Takashi Minakata, Mr. Eiichi Ohno, Dr. Takeshi Aoyagi, Dr. Shin-ya Matsuno, Dr. Makiko Hattori, Mr. Teiichiro Kohno, Mr. Tatsuya Nakao, Mr. Tomio Yamaguchi, Dr. Terumasa Yamasaki, Mr. Susumu Tanji, Dr. Masaru Ozaki, Dr. Haruyuki Yoneda, and Mr. Tokuzo Konishi, for their kind guidance, fruitful discussions, and continuous encouragements.

Finally, the author would like to thank his family, particularly his wife Miki for her sincere support and encouragement.